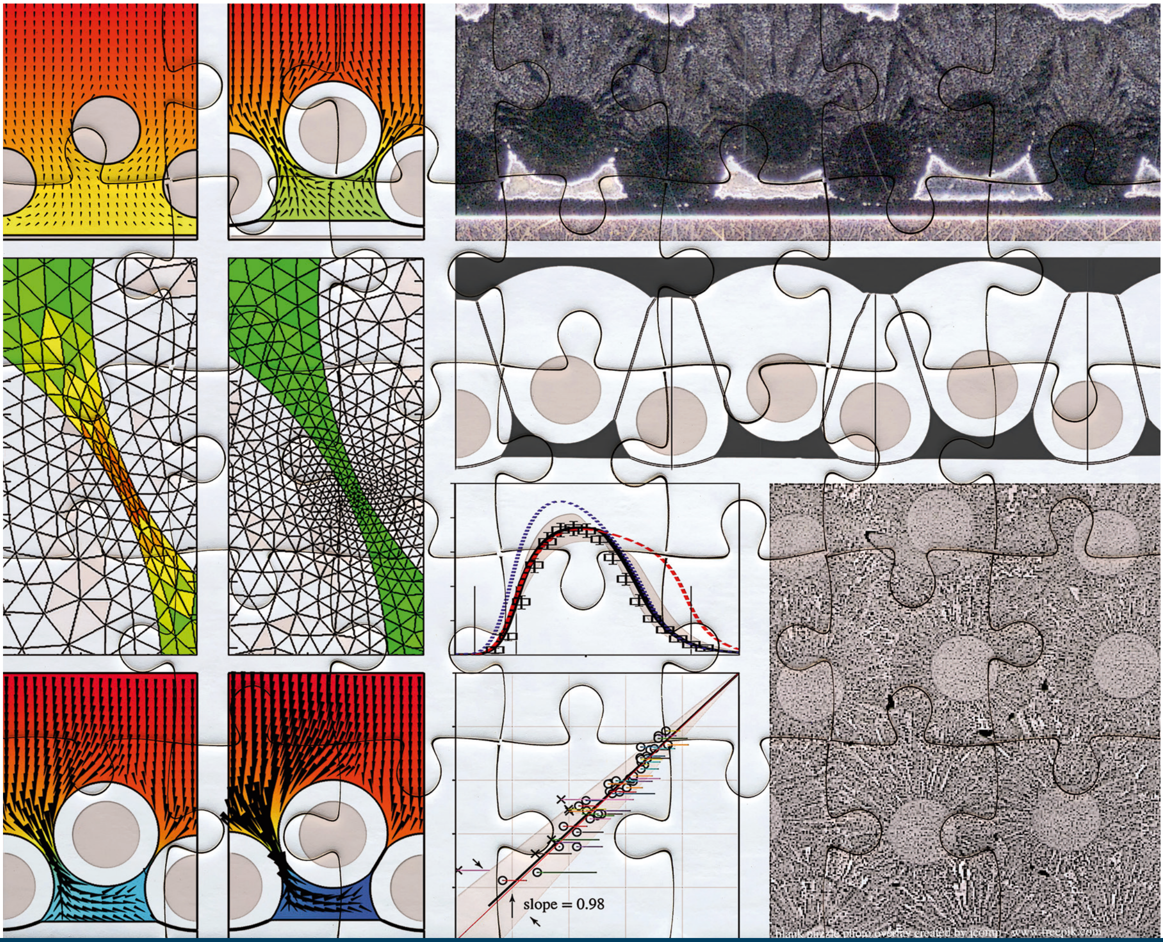

blank puzzle photo overlay created by jcomp - www.freepik.com

Modeling and validation of chemical vapor deposition for tungsten fiber reinforced tungsten

Leonard Raumann

Energie & Umwelt / Energy & Environment
Band / Volume 515
ISBN 978-3-95806-507-9

Mitglied der Helmholtz-Gemeinschaft

JÜLICH
Forschungszentrum

Schriften des Forschungszentrums Jülich
Reihe Energie & Umwelt / Energy & Environment Band / Volume 515

Forschungszentrum Jülich GmbH
Institut für Energie- und Klimaforschung
Plasmaphysik (IEK-4)

Modeling and validation of chemical vapor deposition for tungsten fiber reinforced tungsten

Leonard Raumann

Schriften des Forschungszentrums Jülich
Reihe Energie & Umwelt / Energy & Environment Band / Volume 515

ISSN 1866-1793 ISBN 978-3-95806-507-9

Bibliografische Information der Deutschen Nationalbibliothek.
Die Deutsche Nationalbibliothek verzeichnet diese Publikation in der Deutschen Nationalbibliografie; detaillierte Bibliografische Daten sind im Internet über http://dnb.d-nb.de abrufbar.

Herausgeber und Vertrieb: Forschungszentrum Jülich GmbH
Zentralbibliothek, Verlag
52425 Jülich
Tel.: +49 2461 61-5368
Fax: +49 2461 61-6103
zb-publikation@fz-juelich.de
www.fz-juelich.de/zb

Umschlaggestaltung: Grafische Medien, Forschungszentrum Jülich GmbH

Druck: Grafische Medien, Forschungszentrum Jülich GmbH

Schriften des Forschungszentrums Jülich
Reihe Energie & Umwelt / Energy & Environment, Band / Volume 515

D 82 (Diss. RWTH Aachen University, 2020)

ISSN 1866-1793
ISBN 978-3-95806-507-9

Kurzfassung

In Kernfusionsreaktoren herrschen extreme Bedingungen für plasmabelastete Wandkomponenten. Aktuell wird reines Wolfram (W) verwendet, um den enormen Hitze- und Teilchenflüssen, der Neutronenbestrahlung und der Plasmaerosion standzuhalten. Ein erheblicher Nachteil ist jedoch, dass W inhärent spröde ist und daher ohne Vorwarnung versagen kann. Als Gegenmaßnahme werden derzeit W-faserverstärkte Verbundwerkstoffe (W_f/W) entwickelt. Die Herstellung kann über die Beschichtung von W-Geweben mittels chemischer Gasphasenabscheidung (engl.: chemical vapor deposition (CVD)) erfolgen. Ziel dieser Arbeit ist es, ein tiefgreifendes und quantitatives Verständnis dieses Herstellungsprozesseses zu schaffen, sodass die Materialeigenschaften weiter verbessert werden können.

Unter Verwendung der kommerziellen Software COMSOL Multiphysics wurden Modelle für den W-CVD-Prozess entwickelt und anhand von experimentellen Parameterstudien validiert. Als Highlight wurde eine neue Beschreibung der Reaktionskinetik vorgeschlagen, die Kontroversen in der Literatur bezüglich der Reaktionsordnung des Präkursors WF_6 auflöst [1]. Eine höhere W_f/W-Festigkeit kann durch eine höhere relative Dichte und durch feinere W-Körner erzielt werden. Experimentelle CVD-Parameterstudien und Infiltrationssimulationen ergaben, dass beides durch einen Anlagenbetrieb bei niedrigen WF_6-Gasflussraten, hohen H_2-Gasflussraten, mittleren Gesamtdrücken und niedrigen Temperaturen erreicht werden kann. Da niedrigere Temperaturen die erforderliche Beschichtungsdauer exponentiell erhöhen, werden 723–773 K empfohlen. Zudem ist es wichtig, eine Verarmung von WF_6 innerhalb von zu infiltrierenden Faserzwischenräumen zu vermeiden, da diese zu schnell abnehmenden Abscheidungsraten, zurückbleibenden Poren, und daher zur Verringerung der relativen Dichte führt. Die hierzu minimal notwendige WF_6-Gasflussrate kann mit dem entwickelten Modell berechnet werden.

Die theoretisch optimierten CVD-Prozessparameter wurden experimentell angewendet, um neues massives 15-lagiges W_f/W herzustellen. Neben der Verbesserung der Kornfeinheit und der relativen Dichte, waren weitere Erfolge ein erhöhter Faservolumenanteil, ein reduzierter WF_6-Bedarf, sowie eine gleichmäßigere Schichtdicke im Makromaßstab. Im Mikromaßstab führten die neuen Parameter zu einer praktisch vollständig gleichmäßigen Abscheidung. Daher wurde eine Optimierung der W-Faserpositionen innerhalb des Gewebes (CVD-Substrat) auf Grundlage rein geometrischer Gleichungen vereinfacht.

An bestimmten Stellen können jedoch immer noch Poren aufgrund von Faserpositionsschwankungen auftreten. Konzepte zur Verringerung dieser Schwankungen und auch zur Verbesserung einer kontinuierlichen W_fW-Herstellung werden im Kapitel Outlook vorgestellt.

Abstract

In nuclear fusion reactors there are extreme conditions for plasma facing components. Currently, pure tungsten (W) is used to withstand the enormous heat and particle fluxes, neutron irradiation and plasma erosion. However, a significant drawback is that W is inherent brittle and thus can fail without warning. Therefore, W fiber-reinforced composites (W_f/W) are currently being developed. These can be produced by coating W fabrics via chemical vapor deposition (CVD). The aim of this work is to provide a profound and quantitative understanding of this process so that the material properties can be further improved.

Models for the W-CVD process have been developed utilizing the commercial software COMSOL Multiphysics, and validated against experimental results. As a highlight a new description of the reaction kinetics was proposed solving controversies in literature with respect to the reaction order of the precursor WF_6 [1]. An increased W_f/W strength can be reached by higher relative density and finer W grains. Experimental CVD parameter studies and infiltration simulations showed that both can be achieved by operating at low WF_6 gas flow rates, high H_2 gas flow rates, medium total pressures and low temperatures. As lower temperatures increase the needed deposition time exponentially, 723–773 K are recommended. In addition, it is important to avoid WF_6 depletion within fiber inter-spaces, as this will lead to rapidly decreasing deposition rates, remaining pores, and thus to a reduced relative density. The minimum necessary WF_6 gas flow rate can be calculated with the developed model.

The theoretically optimized CVD process parameters were applied experimentally to produce new bulk 15-layer W_f/W. In addition to finer grains and a higher relative density, further successes were a larger fiber volume fraction, a reduced WF_6 demand and a more uniform macro-scaled coating thickness. On the microscale, the new parameters resulted in such an uniform deposition that the optimization of the W fiber positions within the fabric (CVD substrate) was simplified based on geometric equations. However, in practice, pores can still remain at certain locations due to fiber positional deviations. Concepts for reducing these deviations and also for improving a continuous W_f/W production are presented in the Outlook chapter.

Nomenclature

i, j	Placeholders for species (here WF_6, H_2, HF or W)
A	Area [m^2]
D_{ij}	Binary diffusion coefficient [$m^2\ s^{-1}$]
$D_{eff,i}$	Effective diffusion coefficient [$m^2\ s^{-1}$]
$D_{T,i}$	Thermal diffusion coefficient [$kg\ m^{-1}\ s^{-1}$]
D_{warp}	Warp fiber diameter [(150) µm]
D_{weft}	Weft fiber diameter [(50) µm]
$d_{decel.start}$	Surface-to-surface distance below which the surfaces are decelerated [m]
d_{final}	Final surface-to-surface distance [m]
E_A	Activation energy [$\mathrm{J\,mol^{-1}}$]
k_0, k_1, k_2	Constants for deposition rate equations [$\mathrm{m\,s^{-1}\,Pa}^{-(n_{\mathrm{H_2}}+n_{\mathrm{WF_6}})}$]
k_B	Boltzmann constant [1.381×10^{-23} J K^{-1}]
L_{char}	characteristic length between nearest walls [m]
M_i	Molar mass [g mol^{-1}]
m_i	Mass [g]
Δm_{W}	Deposited mass of W [g]
N	Number of gas species [-]
n_i	Reaction order [-]
P_{tot}	Total pressure [Pa]
p_i	Partial pressure [Pa]
R	Gas constant [$8.314\ \mathrm{J\,mol^{-1}\,K^{-1}}$]
R_{W}	Deposition rate of W [$\mathrm{m\,s^{-1}}$]
R_{exp}	Experimental R_{W} [$\mathrm{m\,s^{-1}}$]
R_{sim}	Simulated R_{W} [$\mathrm{m\,s^{-1}}$]
$R_{\mathrm{WF_6}dep.}$	R_{W}, dependent on $p_{\mathrm{WF_6}}$ [$\mathrm{m\,s^{-1}}$]
$R_{\mathrm{WF_6}indep.}$	R_{W}, independent on $p_{\mathrm{WF_6}}$ [$\mathrm{m\,s^{-1}}$]

S	Reactive sticking coefficient [-]
T	Temperature [K]
T_H	Heater temperature [K]
T^*	Reduced temperature = $k_B T/\epsilon_{ij}$ [-]
Δt	Deposition duration [s]
U_{WF_6}	Consumption rate of WF_6 [-]
$\dot{V}_i$	Volume flow rate [sccm]
x_i	Mole fraction [-]
X_{ff}	Horizontal distance between fiber surfaces [m]
Y'_{ff}	Vertical fiber displacement [m]
Y_{fg}	Vertical distance between lower fiber and ground surface [m]
ϵ_{ij}	Lennard-Jones potential parameter [J]
ρ_i^0	Standard density [g/cm^3]
ρ_{rel}	Relative density = solid volume fraction [-]
σ_{ij}	Collision diameter [m]
Φ_{V_f}	Fiber volume fraction [-]
Ω	Collision integral [-]

Contents

1 Introduction

During the last decades, mankind's technology level and average life standard increased continuously [2]. However, this also led to a strong increase in energy consumption and greenhouse gas emission [2]. As a consequence, global warming is increasingly becoming a threat. Going back voluntarily to preindustrial life standards is not a satisfying option. Therefore, replacements for the finite fossil energy sources have to be found. Nuclear fission is a rather unfavorable solution due to its safety [3] and waste issues [4, 5]. More promising are current efforts in developing Virtual Power Plants, which are meant to connect and manage the different distributed energy resources from volatile renewable energy (wind, solar), non-volatile renewable energy (water, biomass) and energy storage systems (potential energy or heat storages, electric batteries, power-to-gas) [6]. However, to meet the rising base energy demand, a very high storage capacity will be needed for the months without much wind and sun. It is not yet known whether the required storage capacity can be achieved with acceptable cost and raw material amount [2]. Adding, on the other hand, nuclear fusion power plants to a renewable energy dominated electricity network would strongly reduce the needed energy storage capacity and thus could become in long-term a more cost- and resource-efficient solution for the base demand. Nuclear fusion power plants have the potential to provide stable energy with virtually inexhaustible fuel supply, minimal environmental impact, and inherent safety [7]. Additionally, the much higher energy output per required construction area (foot print) compared to renewable energy production would make nuclear fusion power plants ideal for future megacities or very energy intensive industry areas.

The reason why fusion energy is not yet being used is its extremely high complexity and the resulting open questions in research and development without a guarantee for success. This and the already very long development time are on the one hand leading to a rather hesitant governmental funding, but on the other hand to a peaceful cooperation between all nations on earth, on this topic at least. One of those cooperations has allowed to build the International Thermonuclear Experimental Reactor (ITER). ITER, which is on the same time the Latin word for "path", is built in southern France and planned to be ready for the first plasma in 2025. It has the goal to show for the first time a Q of 10, which means that the generated fusion power is 10 times larger than the needed power input to sustain the plasma.

On the way towards fusion power plants the development of high-performance materials with improved lifetimes is essential. In particular, dealing with the nuclear fusion power, resulting in enormous heat and particle fluxes, neutron irradiation, plasma erosion and thermal cycling, is one of the ultimate design challenges [8–11]. Pure tungsten (W) was chosen in ITER as a plasma facing component as it met the harsh requirements best [12, 13]. However, there is a major drawback of pure W. It is intrinsically brittle up to around 500–1200 K (depending on the fabrication process and treatment [14, 15]). This can lead to catastrophic cracks and failure [16]. As potential solution, a new W fiber-reinforced W composite (W_f/W) is currently being developed. A possible synthesis route is chemical vapor deposition (CVD) with W fibers or fabrics as CVD substrate. While starting the present dissertation, dense W_f/W with a sufficiently high fiber volume fraction (30–40%) could not be achieved. As shown in Figure 1.1, remaining large pores weaken the mechanical properties.

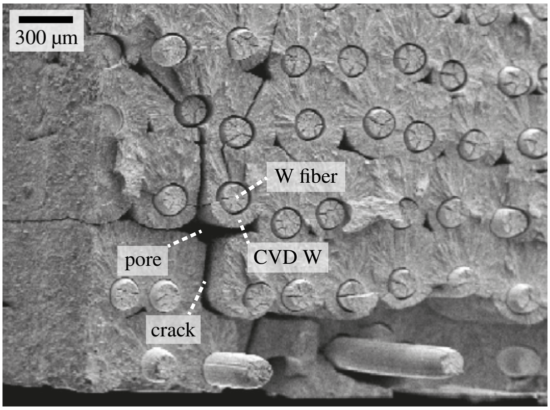

Figure 1.1: Fracture surface of a W_f/W sample after a charpy impact test at room temperature with a crack through a large pore [17].

Therefore, the goal of the present work is to provide a profound and quantitative process understanding to optimize the relative density and the fiber volume fraction of W_f/W via the CVD process parameters (temperature, gas flow rates, pressure) and the fabric geometry parameters (e.g. warp and weft fiber diameters and distances).

Regarding the structure of this dissertation, after the introduction there is a short theory chapter on nuclear fusion reactors and the material challenges, on W, W_fW, and CVD, as well as on the W-CVD reaction kinetics including open questions. The next chapter is about the simplified single fiber model validation to obtain the CVD-W rate equations. Here a newly developed W reaction kinetics description was implemented, which also solves controversies in the literature [1]. In the next chapter, the model parts about the chemistry, fluid dynamics and heat transfer were applied on new geometries being on the one hand the CVD reactor chamber, for a stationary simulation, and on the other hand multiple neighbored fibers, for a transient pore infiltration simulation. The macro-scaled reactor model output provides the species concentration input for the micro-scaled infiltration model, which was also validated experimentally. The next chapter describes how the CVD process parameters and fabric geometry parameters were varied to learn their influence on the relative W_f/W density and the fiber volume fraction. Another chapter is about the influence of the CVD process parameters on the CVD-W grain morphology, which has additionally an important influence on the material properties. The final chapter, before the conclusions and outlook, presents how the newly acquired knowledge was applied to select new parameters and to improve the synthesis of W_f/W.

2 Theory

2.1 Nuclear fusion reactors

Nuclear fusion is the most dominant reaction in our observable universe [18]. It powers stars such as our Sun and therefore is essential for nearly all known lifeforms.

For technical fusion on earth the hydrogen isotopes deuterium ($D = {}^{2}_{1}H$) and tritium ($T = {}^{3}_{1}H$) are most relevant as their repulsive nuclei forces are lower than those of normal hydrogen atoms. To compensate the much lower technically feasible pressure values than in stars, the hydrogen isotopes (DT) have to be heated to even higher temperature than in stars. Around 120-150 million degrees are necessary for ignition, which can be reached by sending high-frequency electromagnetic waves or high kinetic energy particles into the plasma. The plasma is confined via magnetic fields [19], which strongly reduces its interaction with the vessel walls. In this way, a large enough fraction of the energy from the external heating, or later from the fusion reaction, is kept inside of the plasma, which allows for starting and maintaining the fusion reaction (Equation 2.1). Here, α-particles (${}^{4}_{2}He$) and neutrons (${}^{1}n$) are formed with kinetic energies of 3.517 MeV and 14.069 MeV, respectively [19].

$$ {}^{2}_{1}\mathrm{H} + {}^{3}_{1}\mathrm{H} \qquad \longrightarrow \qquad {}^{4}_{2}\mathrm{He} + {}^{1}\mathrm{n} \tag{2.1} $$

The resulting very fast neutrons cannot be confined by magnetic or electric fields. Therefore, they impact on the vessel wall and heat it up, together with the thermal radiation of the plasma. The heat is transported out via coolant media to be used directly or to power conventional electricity generators.

With respect to the magnetic fields, various configurations are being tested. The leading magnetic confinement concepts are the tokamak and the stellarator. In both concepts, the plasma is enclosed by a strong toroidal magnetic field, which is produced by a current flowing through a set of external toroidal field coils. However, as a side effect of the torus shape, the magnetic field is stronger on the inside and weaker on the outside. Without countermeasures, this would lead to a separation of positive ions and electrons and thus to an electric field, which would carry the plasma to the chamber walls [20]. For compensation, an additional poloidal magnetic field is needed, which twists the magnetic field lines, so that the charges do not accumulate anymore in only one area. The poloidal magnetic field can be produced by a set of solely external coils (stellarator) or by inducing a toroidal current into the plasma (tokamak) [20]. As it is impossible to maintain an ever increasing inductor current, a tokamak cannot be operated continuously. Nevertheless, due to successes of the tokamak in the 1960s, the research and development was focused on it so that the attention was moved away from the stellarator for several decades. This is also the reason why the tokamak concept is used for ITER (Figure 2.1a). On the other hand, the more complex stellarator can be operated continuously. Wendelstein 7-X in Greifswald, Germany, showed very promising results recently [21]. Thus, the plasma confinement concept for the first demonstration fusion power plant (DEMO) planned for >2050 is not yet decided.

For both, tokamak and stellarator, the plasma has to be cleaned from fused α-particles, also called helium ash, and from impurities, which were plasma-eroded from the plasma-facing components (PFCs). This is achieved by directing the plasma at so-called divertor targets, which thus have to withstand very strong heat fluxes of up to 20 MW/m^2 [22–25] and even higher during short plasma instabilities [26]. In Figure 2.1b the divertor to be used in ITER is shown.

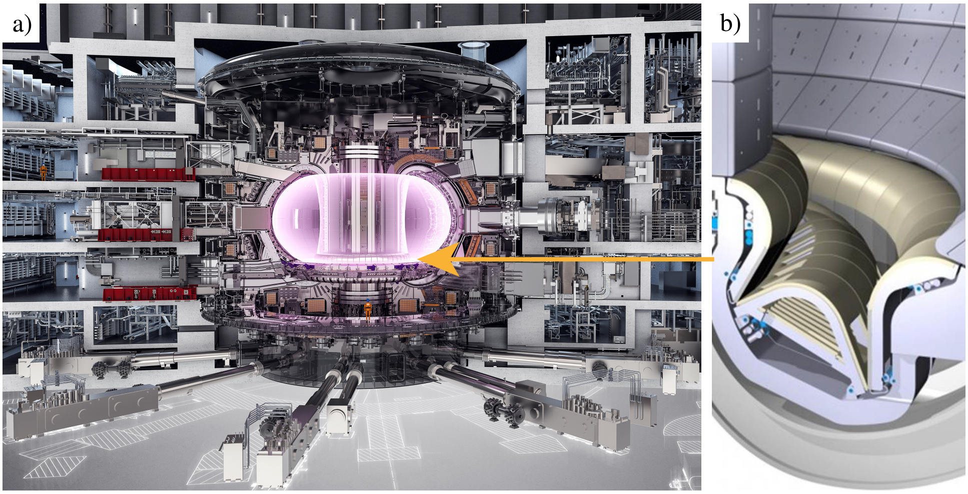

Figure 2.1: a) Technical illustration of ITER with a detailed view of the divertor in b) [27].

For a cost-efficient fusion power plant, the divertors must consist of materials that provide reasonable operational lifetimes despite of the enormous heat and particle fluxes, high-energy neutron bombardment, plasma erosion and thermal cycling [9, 13]. In addition, the material is required to have a high thermal conductivity, should not produce long-living radioisotopes due to transmutation, and should not trap much hydrogen (including radioactive tritium). Possible material solutions are presented in the following sections.

2.2 Tungsten for fusion reactors

Pure tungsten (W) was chosen as material for the PFCs in ITER, since it has the highest melting point of all metals (3422 °C), a high thermal conductivity (175 $\mathrm{W\,m^{-1}K^{-1}}$), low hydrogen retention, high mechanical strength even at high temperatures, a low plasma erosion rate, and a moderate neutron activation [14,22,23,28]. The PFCs design for ITER consists of a tungsten mono block with space for a cooling channel (Figure 2.2 a). In the component developed for ITER, the cooling pipe is made of copper-chromium-zirconium (CuCrZr) [29], which is brazed to W via a Cu interlayer.

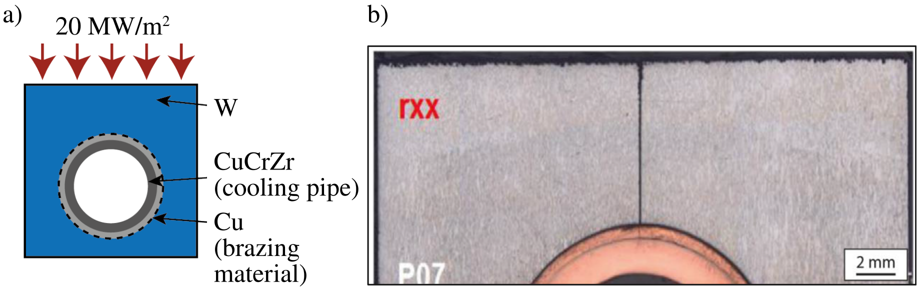

Figure 2.2: a) Schematic of a water-cooled mono block used as divertor. b) 1000 cycles 20 MW/m^2, actively cooled [30].

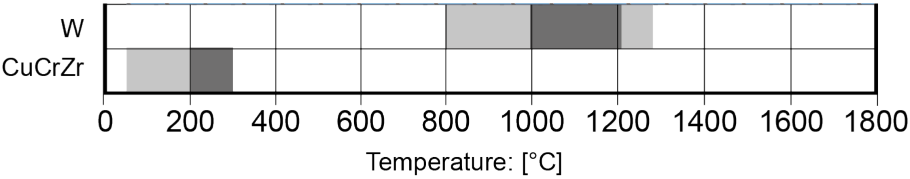

Figure 2.3: Possible operating temperature for W and CuCrZr used in PFCs [17]. The darker areas represent the optimum operating temperature, while the lighter areas represent the maximum possible temperature ranges. The data for W are based on [31] and the data for CuCrZr are taken from [32].

Below the ductile-to-brittle transition temperature (DBTT) a material changes from ductile to brittle. For W the DBTT has a large range of ~60 to ~1000 °C, depending on the production and pretreatment [15, 26, 33] and on the amount of impurities [34]. During operation in the fusion reactor, neutron irradiation causes transmutation and crystal lattice defects, increasing the DBTT of W [26, 35–37]. Even a very low starting DBTT of ~60,°C results in a quick raise to ~500 °C after half a year of operation, and to ~900 °C after one year of operation [26]. However, for CuCrZr the maximum operation temperature is ~300 °C above which the strength deteriorates [32]. Therefore, a problem with the selected materials is that the optimal application temperatures of W and CuCrZr do not overlap after neutron irradiation (Figure 2.3). Furthermore, during operation there are large thermal gradients in the component due to the high thermal loads and the necessary cooling. The different thermal expansion coefficients of W, Cu and CuCrZr lead to stresses. In addition, the neutron irradiation in a fusion reactor will not only increase the DBTT but also reduce the thermal conductivity [16, 38–40] leading to even higher thermal gradients and thus stresses. After many heating cycles at 20 MW/m^2, brittle W could fail catastrophically with cracks down to the cooling channel as shown in Figure 2.2b. Furthermore, in a fusion reactor plasma instabilities can lead to recrystallization and microcrack initiation into the PFC surface [41].

To prevent catastrophic PFC failure, a W composite with extrinsic toughening via fiber-reinforcement is currently being developed in cooperation between the Max Planck Institute for Plasma Physics (IPP) and Forschungszentrum Jülich GmbH.

2.3 Tungsten fiber-reinforced tungsten (W_f/W)

Potassium doped drawn W fibers are coated by an Y_2O_3 interface and then embedded into a W matrix as shown in Figure 2.4. Tungsten fiber-reinforced tungsten (W_f/W) composites are more damage tolerant than pure W. The reason is that the interface allows for several crack-energy dissipating mechanisms leading to a pseudo-ductile composite behavior, similar to fiber-reinforced ceramics (Figure 2.5).

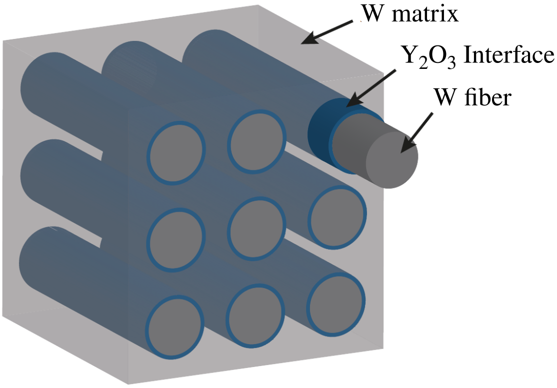

Figure 2.4: Schematic of W_f/W [42]

While the ductility of the fibers is advantageous, the other mechanisms even work with fibers being embrittled during neutron irradiation in the fusion reactor. Due to crack bridging and crack energy conversion into fiber pull-out friction or interface debonding,

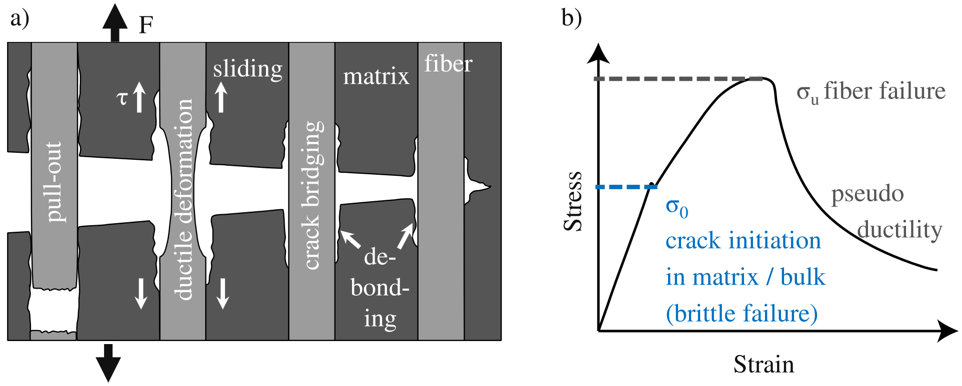

Figure 2.5: a) Crack energy dissipating mechanism of the fibers, b) stress vs. strain curve for a fiber-reinforced composite [43].

W_f/W has the potential to increase the temperature range in which it can be used as a PFC as shown in Figure 2.6.

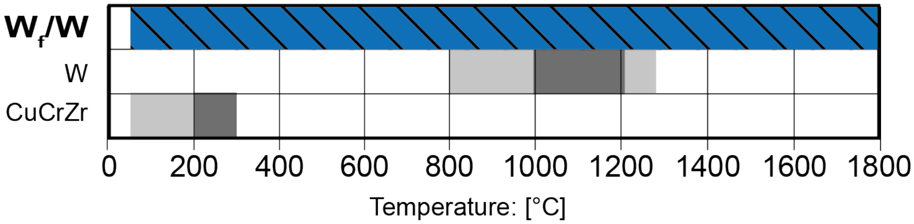

Figure 2.6: Theoretically possible operating temperature for W_f/W added to Figure 2.3.

As first step towards the development of W_f/W, a feasibility study was done and different interlayer materials were investigated by pushing W fibers out of the W matrix (push-out test) [44]. This was necessary as the behavior of the interface between fiber and matrix significantly influences the material behavior of composites with a brittle matrix [45–47]. Subsequently, samples were prepared by chemical vapor deposition (CVD) and the mechanical properties were tested on very small samples. Hereby it was shown via in situ synchrotron tomography that the extrinsic toughening of the material works in principle [48–50]. With the motivation to build an ITER-like mock-up, larger samples were produced via subsequently stacking and coating several fiber layers [17, 51–53]. During another PhD project on W_f/W, the experimental setup was improved, the W fibers replaced by W fabrics, and a prototype for a continuous deposition process was developed [54]. A bit later but still in parallel, the present PhD project was started to build a model to describe and optimize the CVD process parameters for producing W_f/W. Currently the results are used in another PhD project, in which ITER-like mock-ups are produced and tested.

Besides CVD, a second production route is investigated: randomly orientated W short fibers are mixed with a W powder and sintered under high temperature and pressure (e.g. by hot isostatic pressing (HIP), field-assisted sintering (FAST), or spark plasma sintering (SPS) [42, 55–60]). Overviews of the W_f/W development for both production routes are given in [16, 61]. For reference, the dissertations about W_f/W (from the FZJ-IPP cooperation) are listed in Table 2.1.

Table 2.1: FZJ and IPP dissertations about W_f/W produced by CVD or powder metallurgy (PM)

Du 2010	CVD	feasibility study, interface study, push out	[44]
Riesch 2012	CVD	proof of principle, mechanical testing, first models	[48]
Jasper 2017	PM	push-out testing	[42]
Gietl 2018	CVD	introduced W fabrics and continuously deposition	[54]
Mao 2019	PM	larger samples, promising experimental results	[59]
Raumann 2020	CVD	modeling and profound process understanding	this
Schwalenberg	CVD	mock-up production	in progress

2.4 Chemical vapor deposition (CVD)

Chemical vapor deposition (CVD) in general is the decomposition and/or chemical reaction of gaseous precursors into stable solids [62–64]. In a sealed vessel and an activating environment (e.g. by heat, light, plasma) the precursors can react to a powder in the gas phase or to a coating on a solid substrate, whereby mostly also at least one gaseous byproduct is formed.

The first application of this technique took place in 1897 with the deposition of W and molybdenum on carbon filaments (to increase their strength) [65]. Since the 1980s, W-CVD has been intensively used for the metallization of conductor paths in transistors with a very high number of integrated circuits (very/ultra large-scale integration (V/ULSI)) [64, 66–71]. For several decades, CVD is also used for the production of structural materials, composite materials, wear and heat resistance coatings and other functional thin layers [62]. For example, in 2001, approx. 10 million m^2 of architectural glass were coated via CVD with thermal insulation layers of fluorine-doped tin oxide [72]. Recently, CVD has been additionally used for the processing of nano-particles, -wires, -tubes, and -composite coatings [73].

With respect to the synthesis of W_f/W, the outstanding properties of CVD are the possibility of 3D uniform coatings and a good controllability [62, 63], after the process parameters have been optimized. Therefore, the fibers can be positioned and orientated arbitrarily to meet the stresses best as they will occur during the application, which is not possible with randomly orientated short fibers as in the powder metallurgic route. A disadvantage is that hazardous substances (reactants and/or byproducts) are often involved. In addition, CVD is a very complex process and thus difficult to set up [62, 63].

The CVD process used for the present work is a heat-activated W coating process [63, 64, 66]. The key factor for modeling a CVD process is the surface reaction kinetics. Therefore, the W-CVD reaction kinetics needed for the present work is reviewed in detail in the following section.

2.5 Tungsten CVD reaction kinetics

Tungsten (W) can be synthesized via CVD from various gaseous W carriers (e.g. WF_6, WCl_6, WBr_6 etc.) [74]. For the present work WF_6 was used and reduced by H_2, as this precursor combination has several specific advantages. WF_6 is gaseous at room temperature, the deposition takes place already at low temperatures starting at about 550 K, and it leads to very dense and pure W [75]. In addition, as this process is already used for decades in microelectronics production, the precursors are available in large quantities, technically sufficiently pure.

The net reaction for reducing WF_6 with H_2 is described by Equation 2.2.

$$\mathrm{WF_6} + 3\,\mathrm{H_2} \longrightarrow \mathrm{W(s)} + 6\,\mathrm{HF} \tag{2.2}$$

and can be divided into the following reaction steps [76]:

1. Adsorption of WF_6 and H_2 on the reaction surface
2. Stepwise dissociation of WF_6 and H_2 to W, F and H
3. Reaction of H and F to HF
4. Desorption of HF

Between 1970 and 2000, many experimental studies were conducted to identify an equation for the rate-limiting reaction step [76–85], aiming for the prediction of the overall W deposition rate R_W. As a result, Equation 2.3 was found and widely accepted.

$$R_\mathrm{W} = k_0 \exp\left(-\frac{E_A}{RT}\right) [p_{\mathrm{H_2}}]^{1/2} [p_{\mathrm{WF_6}}]^{n_{\mathrm{WF_6}}} \tag{2.3}$$

with k_0 : Constant for deposition rate equation $[\mathrm{m\,s^{-1}\,Pa^{-(1/2+n_{WF_6})}}]$
p_i : Partial pressure of species i [Pa]
$n_{\mathrm{WF_6}}$: Reaction order of WF_6 [-]
E_A : Activation energy $[\mathrm{J\,mol^{-1}}]$
R : Gas constant $[8.314\ \mathrm{J\,mol^{-1}\,K^{-1}}]$
T : Temperature [K].

Simplified rate equations, such as the one above, have the advantage of being able to predict R_W with a relatively small amount of input data. Once the semi-empirical constants E_A, k_0 and n_{WF_6} are known, (theoretically) only T, p_{H_2} and p_{WF_6} are needed. Thus, the efforts to find reasonable values for E_A, k_0 and n_{WF_6} were high. However, especially the search for the value of n_{WF_6} led to a controversial discussion. Mostly, it is stated that n_{WF_6} is zero [77–80] or that it is zero as long as there is sufficient WF_6 [81,82], with the H_2 dissociation being the rate-limiting step. For the case of n_{WF_6} being zero, several authors used Arrhenius plots ($\ln(R_\mathrm{W})$ vs. $1/T$, Figure 2.7) to obtain E_A and k_0 as listed in Table 2.2.

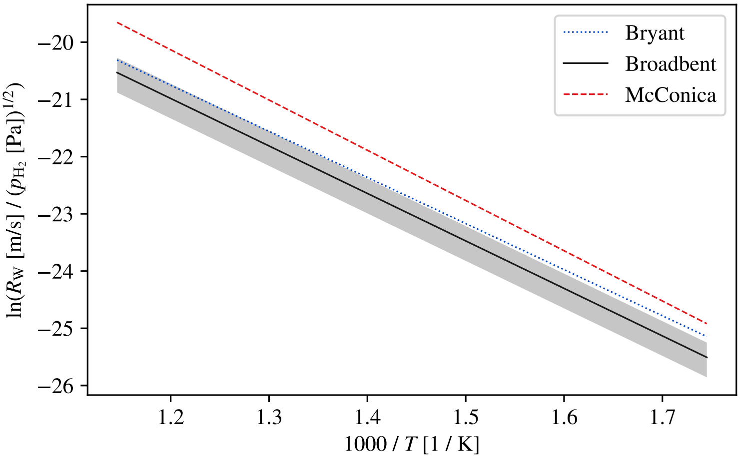

Figure 2.7: Arrhenius plot for W CVD. The values for E_A and k_0 can be found in Table 2.2.

Table 2.2: E_A and k_0 from different publications. The k_0 unit conversion is based on a W density of 19.25 g/cm^3 [86,87])

E_A [kJ/mol]	k_0 [$\times 10^{-6}$ Pa$^{-1/2}$m/s]	k_0 [Pa$^{-1/2}$mol/m^2/s]	
67.0	15.4 ± N.A.	1.57 ± N.A.	[81]
69.0	16.3 ± 4.8	1.70 ± 0.49	[77]
73.0	68.0 ± N.A.	6.93 ± N.A.	[79]

Van de Putte et al. [85] observed $n_{\mathrm{WF}_6} = 1/6$ for low p_{WF_6} and $n_{\mathrm{WF}_6} = 0$ for high p_{WF_6} within the same experimental setup for a fixed T and two different similar total pressures (P_{tot}). Bryant observed $n_{\mathrm{WF}_6} = 1/6$ [83], whereas Bryant reported in 1974 that HF desorption is the rate-limiting step for low T and low P_{tot}, and WF_6 diffusion is limiting for high T and high P_{tot} (the same author concluded five years later that $n_{\mathrm{WF}_6} = 0$, if the WF_6 diffusion towards the surface is sufficiently high [81]). On the other hand, in 1996 Oosterlaken et al. measured p_i in situ 17 mm above the reaction surface via laser Raman scattering and reported again a $n_{\mathrm{WF}_6} = 1/6$ also for higher p_{WF_6} [88]. HF formation and/or desorption was suggested to be the rate-limiting step [88] and to happen simultaneously [89, 90].

Further, McInerney et al. proposed $n_{\mathrm{WF}_6} = 1$ or $n_{\mathrm{WF}_6} = 1/6$ [84] depending on the WF_6 surface concentration. They investigated R_W within nanotrenches for different trench aspect ratios, T and WF_6 flow rates. Further, they found a way to express n_{WF_6} as a function of R_W and the reactive sticking coefficient S, without a need for p_{WF_6} near the surface. Since the trench widths were smaller than the free mean path of the WF_6 gas molecules, the WF_6 flow into the trench was simulated under consideration of geometric view factors. This took into account that the trench walls partially shaded the adsorption sites. S was refined with transient simulations iteratively, until the final R_W profiles, within the trenches, matched to experimental scanning electron microscopy (SEM) results. They concluded that the WF_6 adsorption limits the rate if the WF_6 surface concentration is very low ($n_{\mathrm{WF}_6} = 1$), and that HF desorption limits the rate if the surface is saturated with WF_6 ($n_{\mathrm{WF}_6} = 1/6$).

On the other hand, Creighton suggested that HF desorption is very unlikely the rate-limiting step as it happens very fast and with a low activation energy [91]. Further, Creigthon investigated R_W as function of p_{WF_6} varied over three orders of magnitudes and observed a decrease of R_W for too high p_{WF_6}, which can only be described with a negative n_{WF_6}. Creighton tried to apply a simple Langmuir-Hinshelwood mechanism to describe the observed trends and behaviors. In this mechanism adsorbents compete for surface sites with a deposition rate of zero for a 100% occupancy by either one of the species. Experimentally Creighton observed that if the H_2 to WF_6 ratio is too low (however, still >1), the deposition stops completely. This is explained by a full coverage of the W surface by F atoms, so that the H_2 cannot adsorb and dissociate anymore. It was observed further that R_W can become even negative due to etching of W atoms caused by WF_X subfluoride desorption [91]. Finally, Creighton suggested that the experimentally often observed zeroth order of n_{WF_6} is nothing else than the transition from a positive n_{WF_6} to a negative n_{WF_6}. However, Creighton was not able to describe the observed deposition rates quantitatively.

Arora and Pollard derived a 1D model using statistical mechanics, the transition state theory and bond dissociation enthalpies, to identify the major reaction pathways and rate constants [89]. Taking into account 21 subspecies and 65 surface processes, they reported the rate-limiting steps to be either the conversion of WF_4 to WF_3, or the removal of adsorbed F by H_2.

With better computers it became feasible to enhance the simplified or even detailed rate equations with fluid dynamics and heat transfer simulations, including reactor geometries. Thus, more realistic inner surface conditions could be calculated based on the external process conditions, leading to a better matching and understanding. Kleijn et al. implemented R_{W} from Equation 2.3 with a $n_{\mathrm{WF}_6} = 0$ into the commercial fluid flow simulator Phoenics for the optimization of CVD processes for "blanket" (covering) W depositions [82]. As rate equation they used Equation 2.4.

$$R_{\mathrm{W},eff} = \left(\frac{1}{R_{\mathrm{W}}} + \frac{1}{J_{\mathrm{WF}_6,max}} + \frac{3}{J_{\mathrm{H}_2,max}} \right)^{-1} \tag{2.4}$$

with $J_{i,max}$ being the maximum diffusive flux of species i towards the reaction surface.

Later on, Kleijn's group implemented the detailed rate equations from Arora and Pollard [69–71]. Their approach of combining the Arora model with CVD reactor simulations allowed for describing the selectivity loss of the W deposition. The term selectivity loss refers to the phenomenon that, at high P_{tot} and high T, W does not deposit anymore only on metallic but also on oxidic surfaces. This needs to be avoided for the ULSI circuit production. In addition, their approach covers the negative n_{WF_6} for WF_6:H_2 over-stoichiometry as observed experimentally by Creighton [91]. However, in addition to the higher computational effort, it does not result in a $n_{\mathrm{WF}_6} = 0$ as experimentally observed for changing p_{WF_6} over 2–3 orders of magnitude.

In summary, in the literature many different observations and conclusions have been made regarding the W-CVD deposition kinetics. Therefore, questions remained that were still not answered satisfyingly yet: Which rate equation and which values for n_{WF_6}, E_A and $k_{0,1,2..}$ should be used? Finding an answer was an important first step towards the goal of this thesis, which is the modeling of CVD to optimize the synthesis of W_f/W. New W deposition experiments with very carefully monitored process conditions were performed to acquire a solid basis for a model validation as described in the following Chapter 3.

3 Modeling and validation of W-CVD on single fibers

This chapter describes the development of a model, which is capable of predicting the W deposition rate (R_{W}) quantitatively as a function of the CVD process parameters (heater temperature T_H, total pressure P_{tot}, and gas flow rates $\dot{V}_i^{inlet}$). To reduce the number of unknown variables compared to the W_f/W synthesis, a simplified experiment has been designed, featuring W-CVD on a single fiber mounted coaxially within a heated tube.

3.1 Experimental

3.1.1 Setup

The goal of the experimental design was to acquire R_{W} values with high precision and spatial resolution for a wide range of the process parameters. In addition, a large range for $\mathrm{WF_6}$ conversion rate ($U_{\mathrm{WF_6}}$) values should be obtainable with respect to the process parameter limits of the CVD device. Finally, the setup should allow for a 2 D simplification to reduce the model complexity and thus the computational effort.

The resulting experimental setup is shown in Figure 3.1. Each sample was a unit consisting of a stainless steel (EN 1.4571) tube, a coaxially mounted W fiber, and two fiber holders (EN 1.4571). The W fiber had an outer diameter (OD) of 150 μm. The tube had an OD of 10 mm and a wall thickness of 1 mm. Both had a length of 220 mm. The W fiber allows a direct relevance towards W_f/W, and more data per experimental run. For each parameter set, an uncoated sample unit was firstly connected to the vacuum system of the CVD chamber via Swagelok compression fittings. Secondly, for a good thermal contact, cylindric heaters were clamped around very thick-walled half tubes, which were filling up the space between the heaters and the tube. In this way the heated surface was enlarged allowing for a higher power input. The filler half-tubes (EN 1.4571) had an inner diameter of 10 mm, an OD of 48 mm, a length of 53 mm and an axial distance of 13 mm. The heaters heated each sample from the outside along two zones via the filler half-tubes. The upper zone acted as a preheating zone, to ensure a well defined starting condition in the experiment as well as in the simulation. Here T was kept so low (533 K)

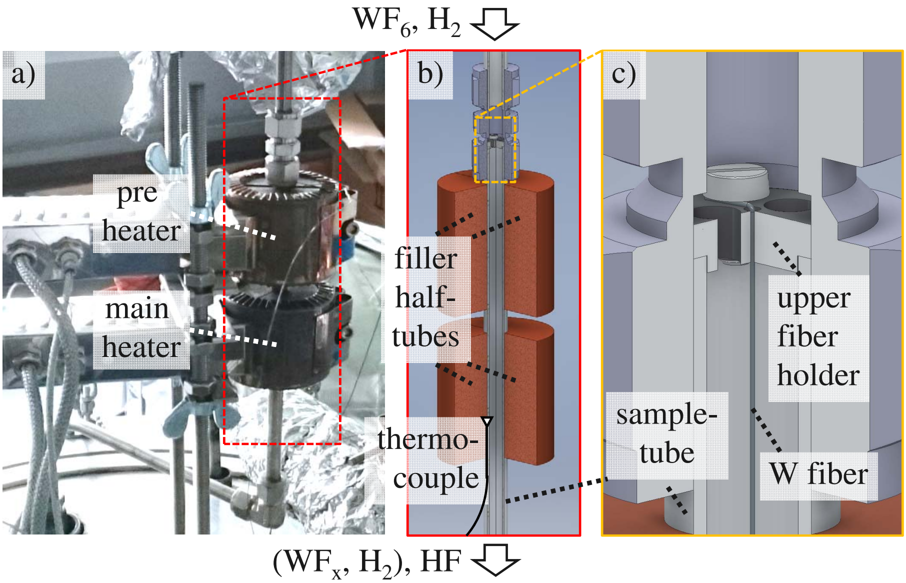

Figure 3.1: Experimental setup for the CVD of W inside a steel tube (sample) and on a coaxially aligned W fiber. a) Photograph, b) 3/4 slice through the sample unit and the filler half-tubes allowing for thermal contact between the heaters and the tube, c) Close-up of the upper fiber holder.

that U_{WF_6} can be neglected as the deposition rate is expected to be at least two orders of magnitude smaller than the rates achieved below in the main heating zone. Furthermore, the preheating zone allows for a reduced convective cooling of the main heating zone, in which the parameter study was done (T_H, 773–913 K). Thermocouples were inserted tightly into grooves cut into the inside of the filler half-tubes, so that their tips directly touched the outer surface of the sample tube. The position of the thermocouple tip to control the main heater temperature (T_H) is marked as $\triangledown$ symbol in Figure 3.1b. It was located 14 mm inwards from the bottom edge of the lower filler half-tubes, which is an important detail as the temperature is higher in the center and cooler towards the edges.

3.1.2 Procedure

The process parameters (T_H, $\dot{V}_{\mathrm{H}_2}$, $\dot{V}_{\mathrm{WF}_6}$, and P_{tot}) are listed in Table 3.1. They can be directly set within the control system of the CVD device. To avoid that T_H drops by more than few degree C, when the WF_6 gas flow is turned on, an Ar gas flow ($=2\cdot\dot{V}^{inlet}_{\mathrm{WF}_6}$) was applied until thermal equilibrium and turned off immediately before the WF_6 gas flow was turned on. P_{tot} was measured in front of the sample and controlled (and measured) behind the sample. For higher P_{tot} both measurements were equal, for low P_{tot} and thus higher flow speeds, the pressure behind the sample was lower, also without chemical reactions. The pressure drop can be explained by the flow cross-sectional area reduction at the upper fiber holder (two little holes, Figure 3.1, c). The gas amount that flows through the upper fiber holder should then not be slowed again at the lower fiber holder. Therefore, the P_{tot} measurement behind the sample should give P_{tot} inside of the sample more accurately than the average of both measurements. Thus, for the table and as simulation input only the measurement results from behind the sample were used.

Table 3.1: Measured and time-averaged CVD process parameters. The bold numbers belong to a series, where the respective parameter in the column head was varied while the other process parameters were kept constant, if possible.

	Process parameters				Further calculated parameters		
Exp. ID	T_H [K]	$\dot{V}^{inlet}_{\mathrm{H_2}}$ [sccm]	$\dot{V}^{inlet}_{\mathrm{WF_6}}$ [sccm]	P_{tot} [kPa]	$p^{inlet}_{\mathrm{H_2}}$ [kPa]	$p^{inlet}_{\mathrm{WF_6}}$ [kPa]	$\dot{V}^{inlet}_{tot}$ [sccm]
#1100	**773**	208	25	10.0	8.91	1.09	233
#1086	**873**	208	26	**10.1**	9.00	1.10	233
#1101	**913**	208	26	10.0	8.88	1.12	**234**
#1090	873	**808**	50	9.93	9.35	0.58	858
#1091	873	**407**	**51**	10.0	8.90	1.11	458
#1092	873	**208**	51	10.0	8.05	1.96	258
#1093	873	407	**100**	10.0	8.02	1.98	507
#1088	873	208	25	**2.50**	2.23	0.27	233
#1089	873	208	26	**0.60**	0.54	0.07	234
#1096	773	800	200	3.12	**2.49**	0.62	1000
#1095	773	889	111	5.61	**4.99**	0.62	1000
#1097	773	941	59	10.6	**10.0**	**0.63**	1000
#1098	773	980	21	10.2	10.0	**0.21**	1000
#1099	773	800	200	12.5	10.0	**2.50**	1000
#1094	913	808	101	9.96	8.85	1.11	**909**

The deposition duration (Δt) was set to values between 26 and 255 min, to obtain similar deposition thicknesses despite the different process parameters. The Δt estimation is based on Equation 2.3 with literature data and the machine process parameters as input.

Detailed temperature measurement

The T profiles along the surfaces of the fiber and inner tube, where the W deposition took place, have the largest impact on R_{W}, and are therefore crucial for the presented study. A further modified setup has been designed to measure these T profiles as a function of the process parameters (T_H, P_{tot}, $\dot{V}^{inlet}_i$), since it is not possible to determine an entire T profile from just a single T_H value, controlled by a fixed thermocouple on the outside of the tube. The setup is shown in Figure 3.2.

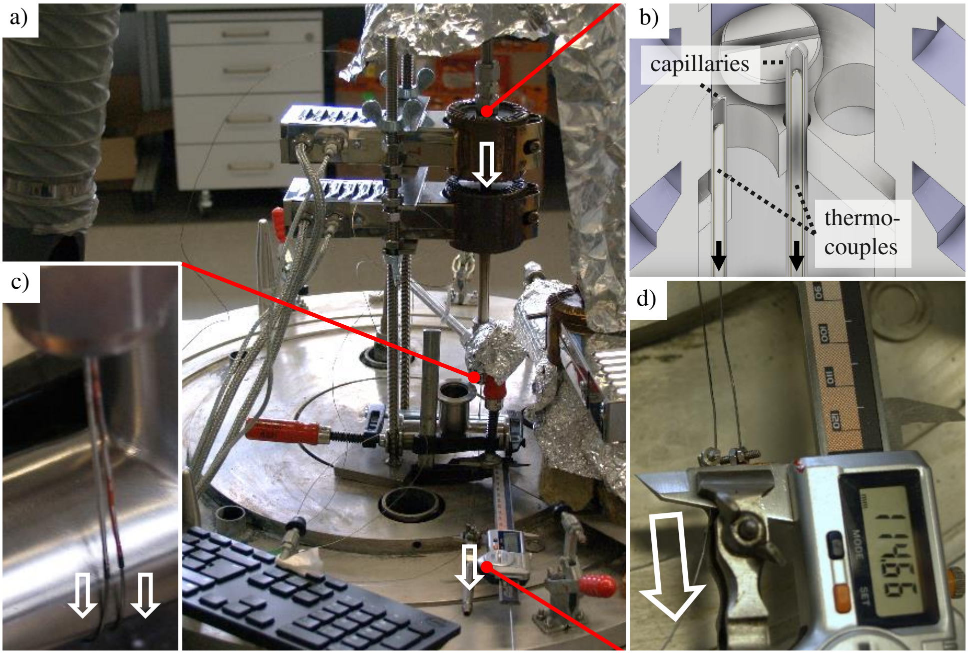

Figure 3.2: a) Modified experimental setup to measure T profiles along the fiber and inner tube surfaces with a high spatial resolution. b) 3/4 slice of the modified sample head. The thermocouples penetrated a T-shaped Swagelok connection behind the sample (c) and were clamped to a caliper (d).

Two graphite greased thermocouples with an OD of 0.5 mm were moved along the inner of two stainless steel capillaries with an inner diameter of 0.6 mm. One capillary was tightly fitted into a round groove, which had been eroded into the inner tube surface. The other one was placed in the tube axis replacing the W fiber (Figure 3.2b). To measure T close to the reaction surface, the wall thickness of the capillaries was chosen at only 0.1 mm. The fixed capillaries and movable thermocouples penetrated a T-shaped Swagelok connection at the bottom (Figure 3.1c). Below, the thermocouples were clamped both to the same digital caliper (Figure 3.1d). T profiles were acquired by opening the caliper in 3-4 mm steps manually, and thus pulling the tips downwards, while T and positional values were recorded.

The T profile measurements were carried out within a single sample. After moving the thermocouple tips, it took between five and nine seconds for reaching thermal equilibrium and recording. To keep the influence of the growing W layers on T low, only the eight experimental parameter sets that led to the lowest R_{W} were applied. Additionally, the entire T_H range (up to of 913 K) was tested with different P_{tot} and $\dot{V}_{\mathrm{H}_2}^{inlet}$ values before using WF_6 in order to have also sufficient data for the heat model validation with respect to the high T_H.

3.1.3 Evaluation

3.1.3.1 W deposition rate

The W deposition thickness on each fiber and inner tube surface was evaluated based on optical microscopy. For each fiber around 90 optical microscopic pictures were combined. In Figure 3.3 a part of such a picture is shown.

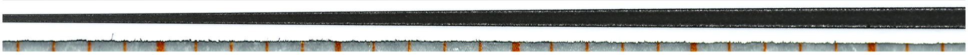

Figure 3.3: Part of a combined microscopic picture of a W-coated W fiber (here black) with millimeter paper at the bottom.

In order to preserve the axial position as mounted inside of the tube during the experiment, each coated fiber was taken out of the tube while being still fixed to its upper holder. Subsequently, as shown in Figure 3.4, the fiber was placed under tension on a transparent box, whereby the holder was placed in (a cut of) a tube again. Further, a caliper was used to measure the distance between the fiber holder and the beginning of the combined microscopic image, which was cut after capturing so that it started at the tip of the caliper (Figure 3.5).

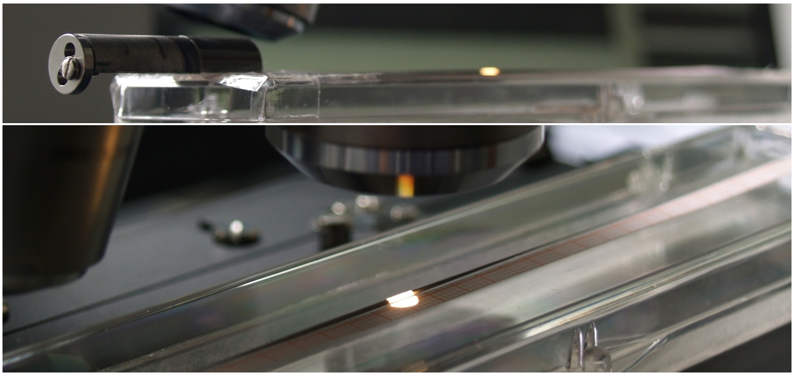

Figure 3.4: Microscopy of the W-coated W fiber within the fiber holder as in the experiment.

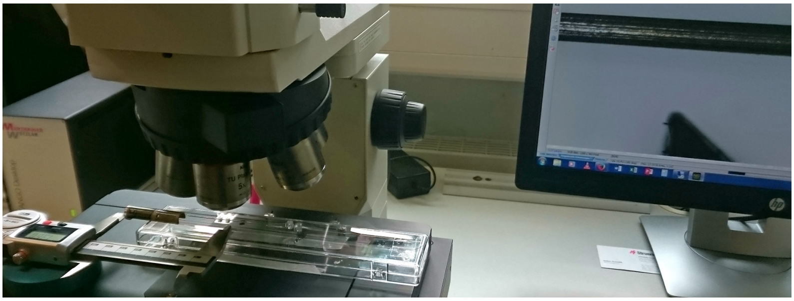

Figure 3.5: Caliper to preserve the axial position.

Using millimeter paper and a virtual overlay grid ensured that the fusing was carried out correctly and revealed a μm-to-pixel ratio of 1.35593. This high precision is necessary to reduce axial-positional uncertainties, which would add up significantly as the images have $> 10^5$ pixels in axial direction. To obtain such images also for the W thickness on the inner tube surfaces, the tubes were filled with epoxy, sliced lengthwise and polished. Otherwise, a similar procedure was performed.

The fiber and tube images were converted to binary pictures so that black equals the W-coated W fiber or the W coating within the tube and white equals the background or reflections of W grain facets (Figure 3.6).

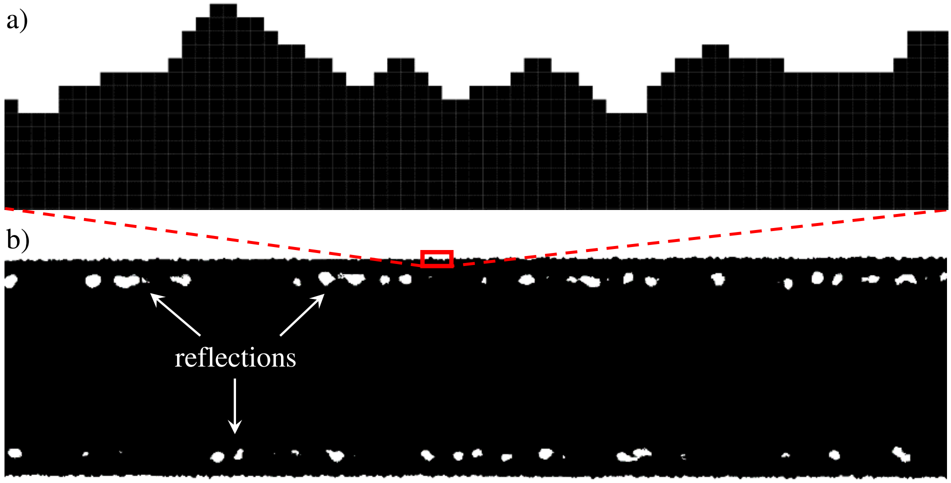

Figure 3.6: Sections of a binary combined microscopic image of a W-coated W fiber, with black = fiber, and white = background or light reflections, and With a) being the maginfication of the red rectangle in b).

A script has been written in Python to obtain the fiber thickness as function of the fiber length from these binary pictures. To avoid that the reflections falsify the W thickness measurements, the script calculates for each x the difference of the y values of the top and the bottom of the fiber, instead of counting the black pixels. A simplified pseudo-code of the script core part is shown in Figure 3.7.

An example of the thickness results is shown in Figure 3.8. The complete experimental results are shown comprehensively after the model description, while being directly compared to the simulation results.

[b]

```
Data: Binary picture of the fiber
Result: fiber thickness as function of
        the fiber length $x$
foreach $x$ do
    $y := 0$
    while pixelColor = white do
        $y := y + 1$
    end
    $y_{top} := y$
    $y :=$ pictureHeight
    while pixelColor = white do
        $y := y - 1$
    end
    Thickness[Pixel]:= $y - y_{top} + 1$
end
```

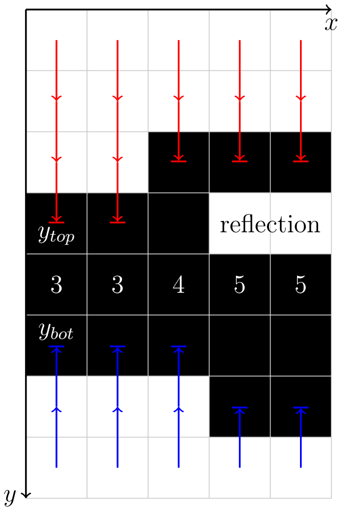

Figure 3.7: Algorithm for acquiring the fiber thickness

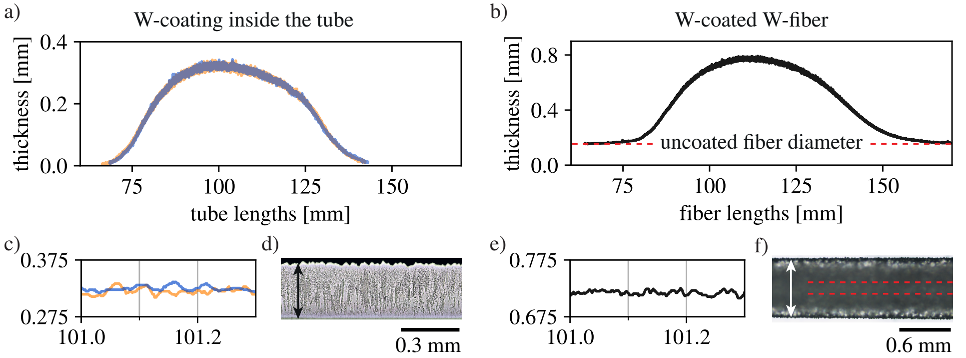

Figure 3.8: Example for the coating thickness measurements (here #1092). a) Inner tube coating thickness with two overlaid curves for each side of the sliced tube. b) Coated fiber thickness. c, e) Zoomed sections of the plots above, with evenly scaled axes to show that the graphs resolve the surface grain structure of the CVD-W. The envelopes of the graphs are the major part of the error bars of R_{exp}. d, f) Image sections near the thickness maxima.

Finally, the average deposition rates $R_{\mathrm{W},exp,fiber}$ and $R_{\mathrm{W},exp,tube}$ perpendicular to the surfaces are calculated via Equation 3.1. This equation set calculates firstly the tube thickness by averaging both sides of the tube slice cross section. Regarding the fiber, the uncoated fiber diameter (150 µm) is subtracted from the measured outer thickness, and halved afterwards to obtain the radially grown thickness. Finally, the interim results are divided by the deposition duration.

$$R_{\mathrm{W},exp,tube} = \frac{s_{tube,side1} + s_{tube,side2}}{2\Delta t_{dep}} \tag{3.1a}$$

$$R_{\mathrm{W},exp,fiber} = \frac{s_{fiber} - d_{fiber}}{2\Delta t_{dep}} \tag{3.1b}$$

with $R_{\mathrm{W},exp}$: experimental growth rate [m/s]

$s_{tube,sideX}$: thickness of coating inside the tube (y-axis in Figure 3.8a), X=1,2 for each side of the sliced tube [m]

s_{fiber} : thickness of coated fiber (y-axis in Figure 3.8b) [m]

d_{fiber} : uncoated fiber diameter (red dashed line in Figure 3.8b) [m]

Δt : deposition duration [s]

3.1.3.2 W coating mass and $\mathrm{WF_6}$ conversion rate

The total W mass gain ($\Delta m_{\mathrm{W},exp}$) was obtained by weighting each sample unit (tube, fiber, fiber holders) together with its Swagelok nuts and cutting rings before and after deposition.

The experimental $\mathrm{WF_6}$ conversion rate ($U_{\mathrm{WF_6},exp}$) was estimated according to Equation 3.2. $U_{\mathrm{WF_6},exp}$ equals the converted $\mathrm{WF_6}$ mass divided by the total $\mathrm{WF_6}$ mass, which was sent into the heated tube.

$$U_{\mathrm{WF_6},exp} = \frac{\text{converted } m_{\mathrm{WF_6}}}{\text{sent in } m_{\mathrm{WF_6}}} \cong \frac{\Delta m_{\mathrm{W},exp} \cdot \dfrac{M_{\mathrm{WF_6}}}{M_{\mathrm{W}}}}{\dot{V}^{inlet}_{\mathrm{WF_6}} \cdot \Delta t \cdot \rho^{0}_{\mathrm{WF_6}}} \tag{3.2}$$

The converted $\mathrm{WF_6}$ mass was estimated via $\Delta m_{\mathrm{W},exp}$ and the mole ratio of $\mathrm{WF_6}$ and W. The total amount of sent in $\mathrm{WF_6}$ mass was calculated via $\dot{V}^{inlet}_{\mathrm{WF_6}}$ multiplied by Δt and the standard density of gaseous $\mathrm{WF_6}$ (12.4 kg/m^3 [92]).

3.2 Model

3.2.1 COMSOL Multiphysics

The model for CVD of W is developed utilizing the commercial Finite Element Method (FEM) software COMSOL Multiphysics ® [93], from now on referred to as Comsol. *Heat Transfer, Chemical Reaction Engineering, and Microfluidics* have been chosen as additional modules.

From the commercially available tools, Comsol was the only option in which all needed physical phenomena could be included. In Comsol one starts with the geometries of the model. As next step, "interfaces" can be added, in which arbitrary equations can be applied to the domains and surfaces of the start geometry.

3.2.2 Model geometry

The simulation boundaries of the 2D axial symmetric model of the earlier described single fiber and tube setup (Section 3.1.1) are shown in Figure 3.9. It was verified with an extra 3D fluid dynamic simulation of the inlet that the upper fiber holder (Figure 3.1c) was far enough away to not violate the 2D axial symmetry within the 2D simulation boundaries.

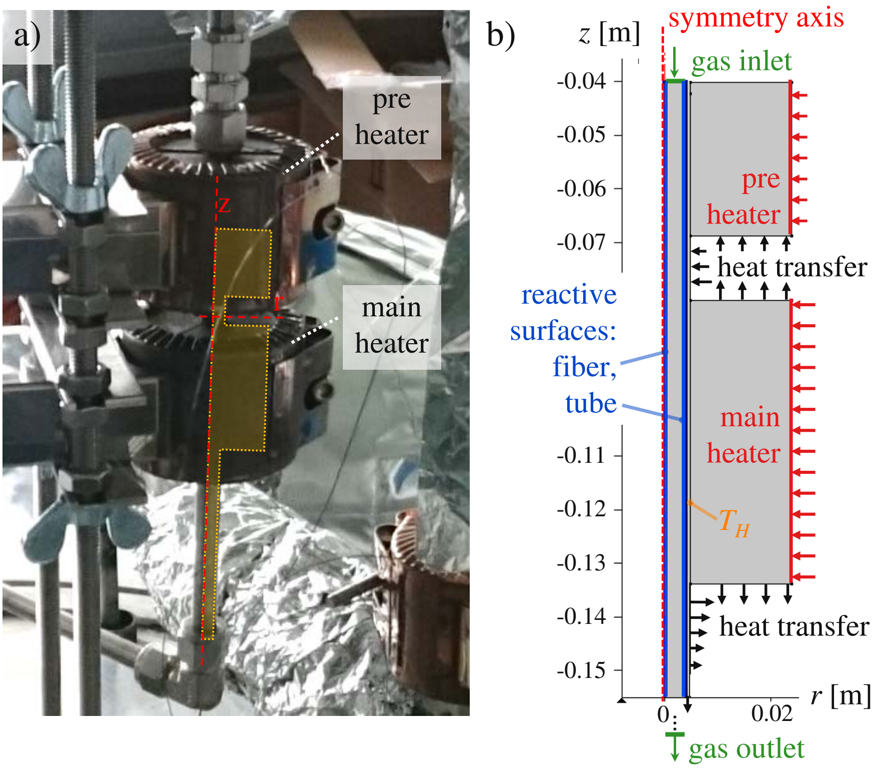

Figure 3.9: a) Location of the model within the experimental setup. b) Sketch of the model boundaries.

3.2.3 Fluid dynamics

The gas mixtures are considered as continua. For the pure species H_2, WF_6, and HF, the heat capacity was fitted to tabulated data from Barin (Ed.) [94], while the gas density, dynamic viscosity, and thermal conductivity are calculated from the Lennard-Jones parameters as in [95]. The spatially resolved gas mixture properties are calculated by

Comsol [93], based on the pure species values and the mass fractions. Similar equations can be found in [82]. Further, the gas flow was assumed to be laminar. This assumption was verified as final step again, by calculating via Equation 3.3 the Reynolds number *Re* to be $\ll 2000$, as described in [96].

$$Re = \frac{dv\rho}{\eta} \tag{3.3}$$

with the inner tube diameter $d = 8\,\mathrm{mm}$, the gas velocity averaged over the cross section (v), the gas mixture density ρ, and the dynamic viscosity η taken for each ID from the simulation results.

3.2.4 Diffusion

Diffusion (from Latin *diffundere* „pour out, spread“) can be divided into ordinary diffusion driven by concentration gradients, thermal diffusion driven by temperature gradients and Knudsen diffusion taking into account fluid-to-solid interaction in gap widths in micrometer ranges. The latter two are not yet needed for the present case and thus will be explained later shortly before they will be used.

The ordinary molecular diffusion is modelled following the Wilke approximation [97]. Fairbanks and Wilke proposed that the effective diffusion coefficients $D_{eff,i}$ can be described with Equation 3.4.

$$D_{eff,i} = (1 - x_i)\left(\sum_{i=1,j\neq i}^{N} \frac{x_j}{D_{ij}}\right)^{-1} \tag{3.4}$$

The binary diffusion coefficient D_{ij} can be estimated via the kinetic gas theory [95]. Kuijlaars specified the following empirical formula for D_{ij} [69] by using the empirical correction from Wilke and Lee [98]:

$$D_{ij} = (6.77 - k_M 0.0492)\, k_M \frac{T^{3/2} \times 10^{-4}}{P_{tot}\sigma_{ij}^2\, \Omega(T_{ij}^*)} \tag{3.5}$$

with $k_M = \sqrt{\frac{1}{M_i} + \frac{1}{M_j}}$ and with $\Omega(T_{ij}^*)$ being the collision integral, which is a stepwise defined function of the reduced temperature $T^* = k_B\, T/\epsilon_{ij}$, tabulated in e.g. [95]. Since gas molecules are not hard spheres, the collision diameter σ_{ij} of two species i and j is calculated commonly via their potential characteristic lengths σ_i and σ_j:

$$\sigma_{ij} = 0.5\,(\sigma_i + \sigma_j) \tag{3.6}$$

The reduced temperature T^*_{ij} is calculated as following:

$$T^*_{ij} = \frac{T}{\epsilon_{ij}/k_B} \tag{3.7}$$

with k_B : Boltzmann constant (1.3807×10^{-23}) [J K^{-1}]

ϵ_{ij}/k_B : Lennard-Jones parameter: Ratio of the maximum energy of attraction between the species ij, and k_B. This is treated as one quantity for practical reasons (no high exponent and a simple unit). [K]

Where ϵ_{ij}/k_B can be calculated via the geometric mean of ϵ_i/k_B and ϵ_j/k_B as in Equation 3.8.

$$\frac{\epsilon_{ij}}{k_B} = \sqrt{\frac{\epsilon_i}{k_B}\frac{\epsilon_j}{k_B}} \tag{3.8}$$

The molar masses and the Lennard-Jones parameters (ϵ_i/k_B, σ_i and $\mu_{D,i}$) for H_2, WF_6 and HF are listed together with all other used material data in the Appendix in Table 9.1.

To reduce the needed model input and the computational effort, $\Omega_{ij}(T^*)$ was fitted as a function of T for each species pair in the mixture of H_2, WF_6 and HF. These fits were inserted into Equation 3.5 and fitted again to simplified functions depending only on T and P_{tot}. The result of this procedure is shown in Equation 3.9. The error of using Equation 3.9 instead of Equation 3.5 is less than 0.64 % for T between 300 and 1200 K.

$$D_{ij} = \sum_{k=0}^{2} \frac{a_k \cdot T^k}{P_{tot}} \tag{3.9}$$

with a_0, a_1, a_2 listed in Table 3.2.

Table 3.2: Polynomials a_0, a_1 and a_2 to calculate D_{ij} according to Equation 3.9.

ij	a_0 [Pa m^2s^{-1}]	a_1 [Pa $K^{-1}m^2s^{-1}$]	a_2 [Pa $K^{-2}m^2s^{-1}$]
H_2 WF_6	-2.518	1.521×10^{-2}	1.459×10^{-5}
HF WF_6	-6.384×10^{-1}	2.922×10^{-3}	5.583×10^{-6}
H_2 HF	-4.832	2.885×10^{-2}	3.498×10^{-5}

In addition, it was tested to describe the ordinary diffusion using the more computationally costly Stefan-Maxwell formulation [99] instead of the Wilke approximation. The difference was negligible compared to using only the Wilke approximation. The reason is probably that the species transport in this setup is dominated by convection. In a further test, also thermal diffusion [95] was included. It turned out that thermal diffusion can be neglected as well in this setup due to only very small T gradients perpendicular to the reaction surfaces.

3.2.5 Heat transfer

Comsol's built-in functions were used for simulating thermal conduction, convection and radiation [93]. The heater temperature T_H was not simulated directly, but instead a simulated heating power was adjusted by a virtual PI controller to match T_H at the same position, at which the thermocouple was placed in the experiment. This was necessary to simulate the convective cooling of the inner surfaces by the inflowing gas. The simulations were conducted transiently, whereby the growing W coating was taken into account by a deforming mesh. The deposited W changes the effective heat conductivity, especially in axial direction. This effect leads to an increasing heating power during the deposition process, which was observed in the simulation and also in the experiment.

The real values of the thermal losses to the surrounding, and especially of the gap conductance between the outside of the steel tubes and the inside of the clamped filler half-tubes, are not accessible for validation. However, their values become more obvious by many experimental results, which are accessible. For example, a higher gap conductance increases the maximum and the broadness of the T profiles and thus increases also the WF_6 consumption. Further, a higher gap conductance reduces the influence of the convective gas cooling and therefore shifts the axial position of the W coating on the fiber towards the center of the heating zone.

Therefore, firstly the thermal losses and the gap conductance were chosen to satisfy 19 sets of experimentally recorded T profiles (at tube and fiber positions). The T profiles include measurements without gas flow or with only H_2 flow for different T_H and P_{tot}. They include further the measurements for the process parameters as in Table 3.1 for #1089, #1091, #1095 − 1100 (lower R_{W}). Secondly, the T profiles were modelled for the missing IDs with just the process parameters as changing input. Finally, the thermal losses and the gap conductance were refined to best meet additionally the experimental data of all 15 WF_6 consumption rates and axial positions of the W coating thickness peaks along the fibers. Since also the semi-empirical constants of the deposition rate equations influence the WF_6 consumption, this refinement had to be repeated several times. This procedure resulted in a gap conductance of $280\,\mathrm{W\,m^{-2}K^{-1}}$ for 773 K, increasing linearly to $420\,\mathrm{W\,m^{-2}K^{-1}}$ for 913 K. The uncertainty for the gap conductance was estimated to 25%, whereby the resulting uncertainties for the T profiles is $<\sim 3\%$. An increasing gap conductance with increasing T_H is meaningful as a higher thermal expansion leads to a higher contact pressure.

3.2.6 Chemistry and rate equations

Negative reaction orders $n_{\mathrm{WF_6}}$ or even negative deposition rates R_{W} are of no concern for the synthesis of W_f/W, since the H_2 to WF_6 ratio is kept > 3. Therefore, it is not necessary to include detailed subreactions and subspecies such as WF_X with $X < 6$. Gas bulk reactions were neglected as well. Furthermore, in the parameter regime used, the Y_2O_3-coated W fabric substrate is coated by W within the first minute. After that it is the same as coating pure W. Therefore, rate equations to describe subreactions with the Y_2O_3 substrate or a potential "selectivity loss" (the term is explained in second last paragraph of section 2.5) are neglected as well. Instead, fast solving simplified rate equations (3.10, 3.10a and 3.10b) were used to describe the chemical reactions at the surface. The finding of Equation 3.10 is the major outcome of the presented chapter and will be validated and discussed in the following sections. Equation 3.10a was used as suggested by McInerney et al. [84], since no further adjustment was necessary. Equation 3.10b, however, was adjusted in its semi-empirical constants E_A and k_0 with respect to the experimental and simulated data from this work. The adjusting procedure is described in the last section, before the summary. This section order was chosen, because the procedure, which inhabits several complicated iterative steps, is easier to understand after the experimental and modeling results have been shown and discussed.

The species mass fluxes, towards (WF_6, H_2) and originating from (HF) the reactive surface boundaries are calculated via the stoichiometry, resulting from Equation 2.2, in conjunction with the reaction rate (Equation 3.10). The heat of reaction is calculated via the thermodynamic properties of the species as listed in Table 9.1 in the Appendix. To achieve faster convergence without any practical relevance due to negligible deposition rates, R_{sim} (Equation 3.10) was smoothly reduced towards zero at $p_{\mathrm{WF}_6} < 0.3\,\mathrm{Pa}$ or $< 473\,\mathrm{K}$.

Further simulated quantities used for validation were $\Delta m_{\mathrm{W},sim}$ and $U_{\mathrm{WF}_6,sim}$. Since the simulated sample cannot just be weighted as the real one, $\Delta m_{\mathrm{W},sim}$ was obtained by multiplying the simulated deposited W volume with the density of CVD-W (19.25 g/cm^3 [86, 87]). $U_{\mathrm{WF}_6,sim}$ is easily accessible via Equation 3.11.

$$R_{sim} = \min(R_{\mathrm{WF}_6 indep.}, R_{\mathrm{WF}_6 dep.}) \tag{3.10}$$

with $R_{\mathrm{WF}_6 dep.}$ from Equation 3.10a and $R_{\mathrm{WF}_6 indep.}$ from Equation 3.10b.

$$R_{\mathrm{WF}_6 dep.} = \left(\frac{1}{k_1\, p_{\mathrm{WF}_6}} + \frac{1}{k_2 \exp\left(\frac{-E_A}{RT}\right) [p_{\mathrm{H}_2}]^{1/2} [p_{\mathrm{WF}_6}]^{1/6}} \right)^{-1} \tag{3.10a}$$

with $E_A = 64$ kJ/mol, $k_1 = (32.63 \pm 2.88) \times 10^{-9}\ \mathrm{m\,s^{-1}Pa^{-1}}$ and $k_2 = (45.79 \pm 1.28) \times 10^{-7}\ \mathrm{m\,s^{-1}Pa^{-2/3}}$, [84].

$$R_{\mathrm{WF}_6 indep.} = k_0 \exp\left(\frac{-E_A}{RT}\right) [p_{\mathrm{H}_2}]^{1/2} [p_{\mathrm{WF}_6}]^0 \tag{3.10b}$$

with $E_A = (73.7 \pm 0.9)\,\mathrm{kJ/mol}$ and $k_0 = (3.99 \pm 0.51)\,\mathrm{mol\,m^{-2}s^{-1}Pa^{-1/2}} = (38.22 \pm 4.85) \times 10^{-6}\ \mathrm{m\,s^{-1}Pa^{-1/2}}$.

$$U_{\mathrm{WF}_6,sim} = 1 - \frac{\int_0^{\Delta t} \dot{V}^{outlet}_{\mathrm{WF}_6,sim}\,dt}{\dot{V}^{inlet}_{\mathrm{WF}_6,sim}\,\Delta t} \tag{3.11}$$

with $\dot{V}^{inlet}_{\mathrm{WF}_6,sim}$ constantly being equal to $\dot{V}^{inlet}_{\mathrm{WF}_6}$ (Table 3.1), thus no integration is necessary; and with $\dot{V}^{outlet}_{\mathrm{WF}_6,sim}$ decreasing over time, because as the W grows, the T profiles become slightly broader. This indeed led to, depending on the process parameters, an increase of $U_{\mathrm{WF}_6,sim}$ between 0.02 and 3.3 % from the start to the end of a deposition.

3.3 Experimental vs. simulated results

Figure 3.10 shows simulation results within the 2D axial symmetric setup. It can be seen how the gas mixture flows in from above and is heated in the hot area, where the CVD reaction takes place and WF_6 and H_2 are consumed. At the bottom the gas flow rate is increased due to the gaseous product HF having a stoichiometric ratio of 6:4 compared to the sum of the educts (Equation 2.2). With respect to the larger $\dot{V}^{inlet}_{tot}$ the flow rate at the length $z = 15.5$ cm is additionally increased due to the gas expansion caused by a higher T behind the main heating zone.

These kind of plots are well suited to develop a first process understanding and to check the simulation for plausibility, however, not to precisely compare the simulated and experimental results.

Therefore, as next step T and R_W are plotted as lines (simulation) and as symbols (experiment) along the fiber and the inner tube surface in z direction. Lines for p_i are included as well to give an overview of all important quantities, which determine R_W.

In Figure 3.11 the comparison for the $p^{inlet}_{\mathrm{H}_2}$ variation is depicted. The simulated results match very well the experimental results. The results were averaged over Δt, except for the experimentally acquired T, which was measured only once as described in the last part of the experimental procedure (Section 3.1.2). The deposition rate R_W starts with nearly zero showing that T of the preheater was chosen low enough. R_W rises with increasing T within the main heating zone and with increasing p_{H_2}.

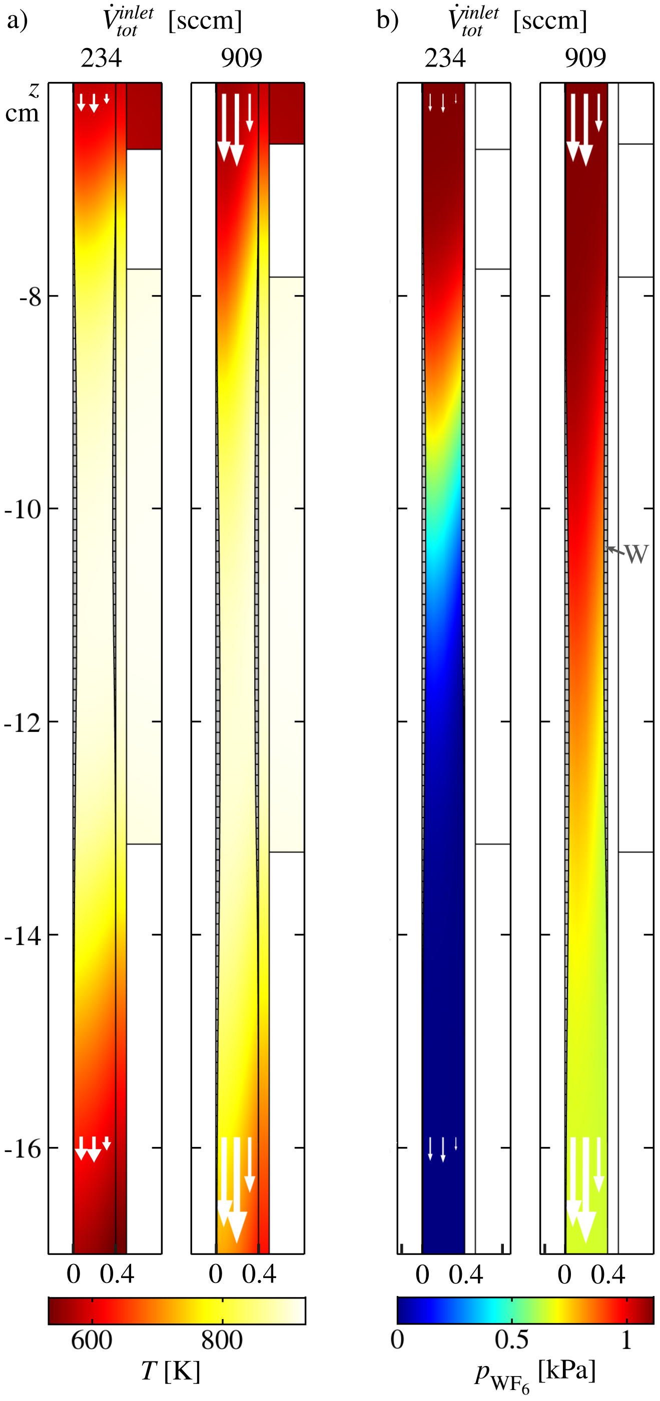

Figure 3.10: Color maps for a) T and b) p_{WF_6} for different $\dot{V}_{tot}^{inlet}$ (Exp. IDs #1101 and #1094). The vector lengths are proportional to $\dot{V}_{tot}$. At the fiber surface (radius $r = 0.075$ cm) and the inner tube surface ($r = 0.4$ cm) the simulated W coatings can be seen within the hot area.

The experimental error bars originate from measurement uncertainties. For the fiber depositions they are so small, because there were no thermal stresses (W on W) and no metallographic preparation artifacts. The error bands for the simulation result from uncertainty in input parameters as e.g. T_H or the gap conductance of the thermal contacts.

$\dot{V}_{tot}^{inlet}$ was chosen high, so that p_i stayed almost constant along the tube length. This was done in order to nearly rule out the influence of depletion intending a modeling simplification. However, it turned out that for such high $\dot{V}_{tot}^{inlet}$ thermal effects need to be considered more carefully. The reason is that the different outlet pressures lead to different gas velocities. Consequently, especially on the fiber having a low mass, the different gas velocities lead to different amounts of convective cooling (T drop) and on the fiber to an x-axis shift of the R_{W} peak as it can be seen in Figure 3.11, right subplots.

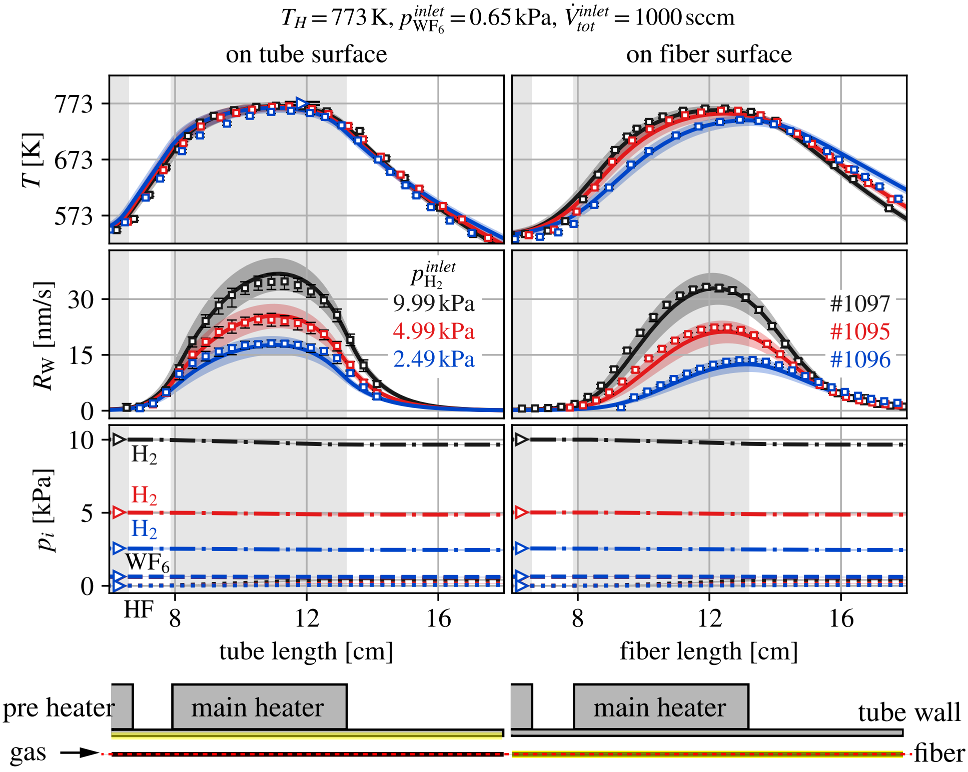

Figure 3.11: Model validation for the variation of $p_{\mathrm{H_2}}^{inlet}$ with subplot rows for T, R_{W} and p_i. The left and right subplot columns show the results along the tube and fiber surface, respectively. Each color represents the data from one CVD process parameter set (same as one row in Table 3.1 with the corresponding ID). In the header the constant process parameters are given. The symbols (□, ▷) represent experimentally measured results with (▷) being data used as input for the simulation. The solid lines represent the simulated T or R_{W}. The dashed, dash-dotted, and dotted lines represent the simulated $p_{\mathrm{WF_6}}$, $p_{\mathrm{H_2}}$, and p_{HF}, respectively. The gray areas mark the pre- and main heater positions.

In Figure 3.12 the $p_{\mathrm{WF}_6}^{inlet}$ variation is presented. On the tube surface R_{W} is not affected by a variation of $p_{\mathrm{WF}_6}^{inlet}$ down to 0.21 kPa, at least in conjunction with the other parameters used. However, on the fiber surface there is on first glance an opposite trend: with increasing $p_{\mathrm{WF}_6}^{inlet}$ the deposition rate decreases. But this is just a side effect of the T change, as with higher $p_{\mathrm{WF}_6}^{inlet}$ the heat capacity of the gas mixture is increased and thus, near the fiber, the incoming gas is not heated up entirely towards T_H.

Therefore, R_{W} is decreased here by higher $p_{\mathrm{WF}_6}^{inlet}$ only indirectly via T and R_{W} can be described also on the fiber very well with the rate equation being independent of p_{WF_6} (Equation 3.10b). However, this does not mean that R_{W} is always independent of p_{WF_6}.

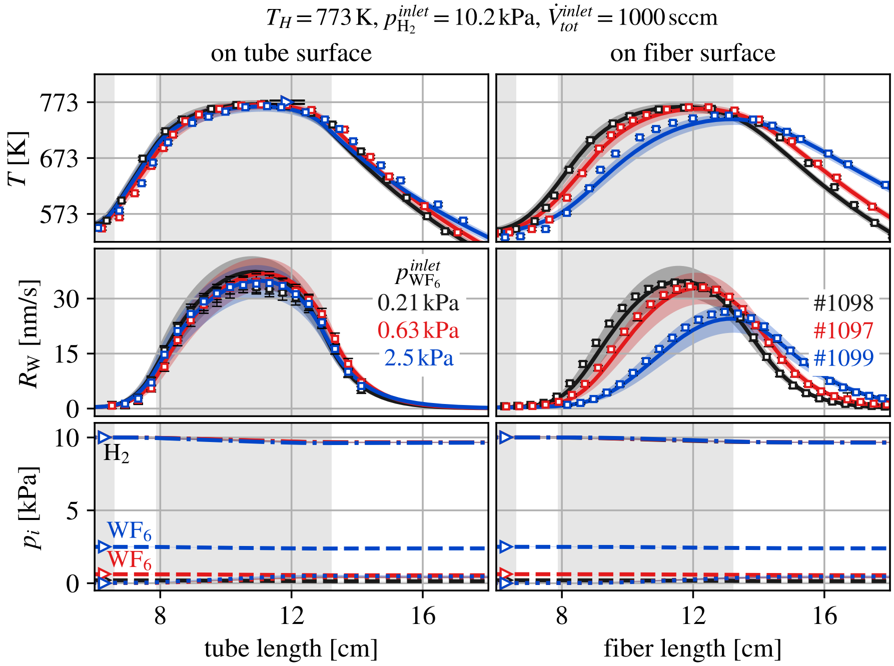

Figure 3.12: WF_6 variation; apart from that the labeling is identical to that of Figure 3.11.

The next plot group, Figure 3.13, shows the model validation for the variation of T_H. Besides the higher T_H, $\dot{V}_{tot}^{inlet}$ is significantly lowered compared to the series shown before. This was done to also investigate the effect of $\mathrm{WF_6}$ depletion on R_W. The lowest subplot row shows how $p_{\mathrm{H_2}}$ and $p_{\mathrm{WF_6}}$ decrease while p_{HF} increases. As expected this conversion increases with increasing T_H. As it can be seen in the left subplot column, with $T_H = 913\,\mathrm{K}$, R_W collapses to zero still within the hot area indicating that the $\mathrm{WF_6}$ consumption ($U_{\mathrm{WF_6}}$) is 100 %. This collapse (black curve) leads to an intersection with the R_W curve for 873 K (red curve), since here $U_{\mathrm{WF_6}}$ is only 90 % so that R_W does not drop as far within the main heating zone. This effect can be observed experimentally and is also covered well by the model. Regarding R_W on the fiber the same can be observed in the right subplot column but less pronounced. The reason for this is that $U_{\mathrm{WF_6}}$ is slightly lower on the fiber due to a smaller surface area and due to a slightly narrower T peak, caused by the convective cooling from the incoming gas.

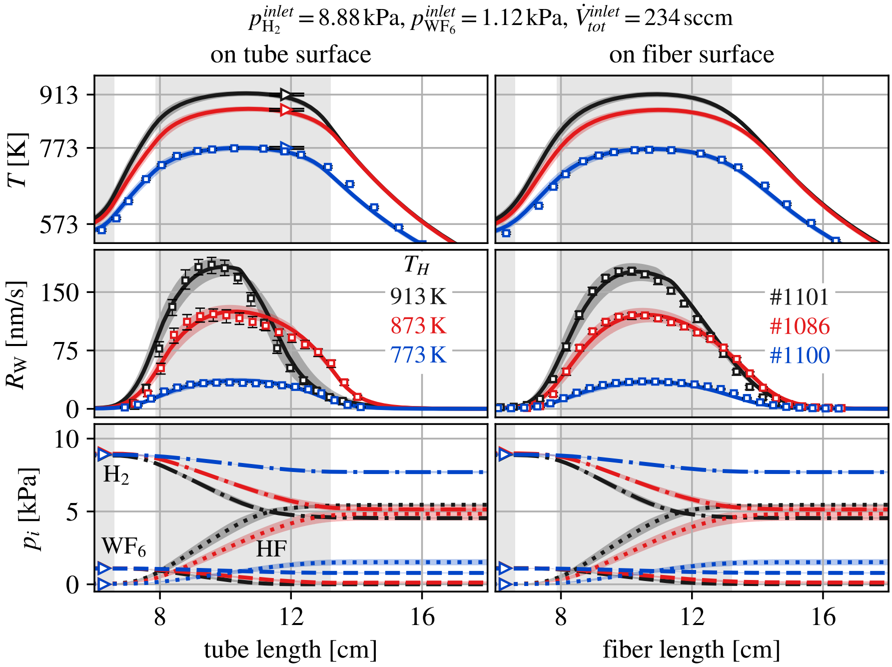

Figure 3.13: $T_H$variation; apart from that the labeling is identical to that of Figure 3.11.

The special case of the R_W collapse for $T_H = 913\,\mathrm{K}$ at the inner tube surface is depicted in Figure 3.14a more detailed. Here, the results of the deposition rate equations (3.10a, 3.10b) are shown together with $p_{\mathrm{WF_6}}$. It can be seen that $R_{\mathrm{WF_6}dep.}$ (Equation 3.10a) results in an overestimation of R_{exp} before the intersection point at $x = 10.8\,\mathrm{cm}$, while $R_{\mathrm{WF_6}indep.}$ (Equation 3.10b) results in an overestimation of R_{exp} after the intersection.

Only by taking the minimum of both rate equations, as it is done by R_{sim} (Equation 3.10), the experimental results match well along the complete tube lengths.

The idea behind another tested parameter set was that if more process gas is offered, the complete depletion of WF_6 should not happen for otherwise identical conditions. This was proven with #1094 experimentally and in the simulation. Here, $\dot{V}_{tot}^{inlet}$ was increased from 234 sccm to 909 sccm for otherwise same parameters compared to #1101. The result is shown in Figure 3.14b. In subplot b) the simulated p_{WF_6} (right y-axis, —) stays high and no change in the limiting rate equation takes place.

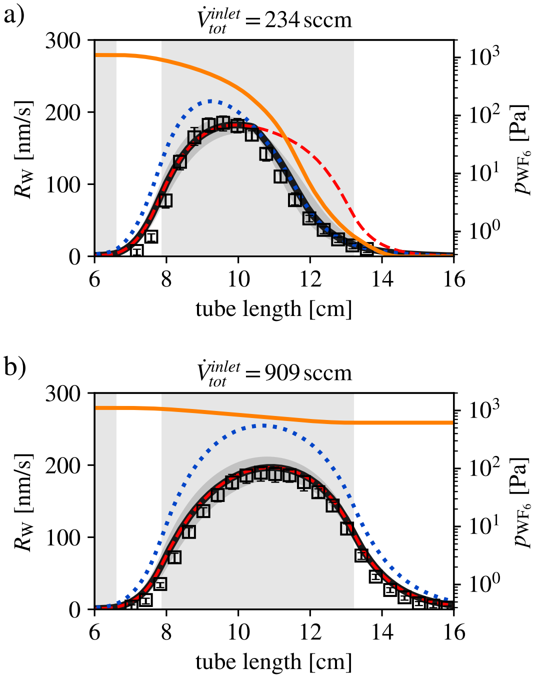

Figure 3.14: p_{WF_6} (—) and R_W at the inner tube surface versus the tube length for different $\dot{V}_{tot}^{inlet}$, with R_{exp} (□) and R_{sim} (▬) following the minimum of $R_{\mathrm{WF}_6 dep.}$ (⋯⋯) and $R_{\mathrm{WF}_6 indep.}$ (- - -). $T = 913\,\mathrm{K}$, $P_{tot} = 10.0\,\mathrm{kPa}$, $[\mathrm{WF}_6\text{:}\mathrm{H}_2]_{inlet} = 1\text{:}8$. a) $\dot{V}_{tot}^{inlet} = 234\,\mathrm{sccm}$, #1101, b) $\dot{V}_{tot}^{inlet} = 909\,\mathrm{sccm}$, #1094. For these IDs the 2D color maps were shown in Figure 3.10.

With #1094 having the highest T and $\dot{V}_{tot}^{inlet}$ combination, Figure 3.14b shows also that W did not deposit outside of the samples, which would be at x-axis values $> 22\,\mathrm{cm}$, whereby R_W approaches already zero at $x = 16$. This is important for a correct validation of the deposited W mass (Δm_W) and the WF_6 consumption rate (U_{WF_6}).

Figure 3.15 provides an overview of the experimental versus the simulated results. It compares the maximal deposition rates R_{max} in the tubes and on the fibers as well as Δm_{W} and U_{WF_6}. As can be seen from the slopes of the fitting lines (=1.0), $R_{sim,max}$ and $R_{exp,max}$ are very well in agreement for both on the fiber and inside the tubes. Since R_{max} matches, the comparison of Δm_{W} gives an indication about how well the integrals of the R_{W} profiles (as in Fig. 3.11 – 3.14b) match. Also here the agreement is good for all process parameter sets. Finally, $U_{\mathrm{WF}_6,sim}$ (Equation 3.11) matches also well to $U_{\mathrm{WF}_6,exp}$ (Equation 3.2), validating the chemical model part in an additional way. To conclude, Figure 3.15 combines the successful validation of the experimental results regarding the in situ process parameter measurements and the post deposition optical and gravimetric measurements.

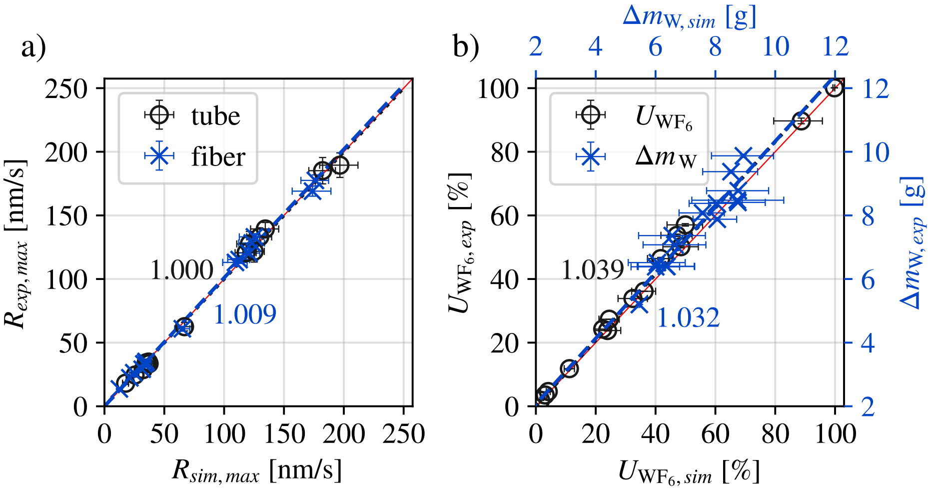

Figure 3.15: Overview of the comparison between experimental and simulated results for a) $R_{exp,max}$ and $R_{sim,max}$, which are also tabulated in the Appendix, and for b) U_{WF_6} and Δm_{W}.

3.4 Discussion

Apart from W_f/W as motivation, one of the main goals of this study is to improve the understanding of the W deposition rate and to find a simple rate description that is valid for a broad parameter regime. All experiments of this study can be described successfully by using Equation 3.10. As next step it will be shown that this approach can even be applied to acquire for the first time a coherent description of different experimental results from literature – even though these results lead on their own to contradicting conclusions, especially regarding the p_{WF_6} dependence as reviewed earlier (Section 2.5).

In Figure 3.16 experimental data from this study and from the literature is plotted together with calculated results using Equation 3.10. As input for Equation 3.10 the averaged T and p_{H_2} were taken from the experimental data as described by the respective authors in [76, 78, 85]. Equation 3.10 describes the transition in the WF$_6$ reaction order (n_{WF_6}) from 1/6 (····), for low p_{WF_6}, to zero (- - -), for high p_{WF_6}. This transition point matches well with the experimental observations by Van der Putte et al. (□) [85].

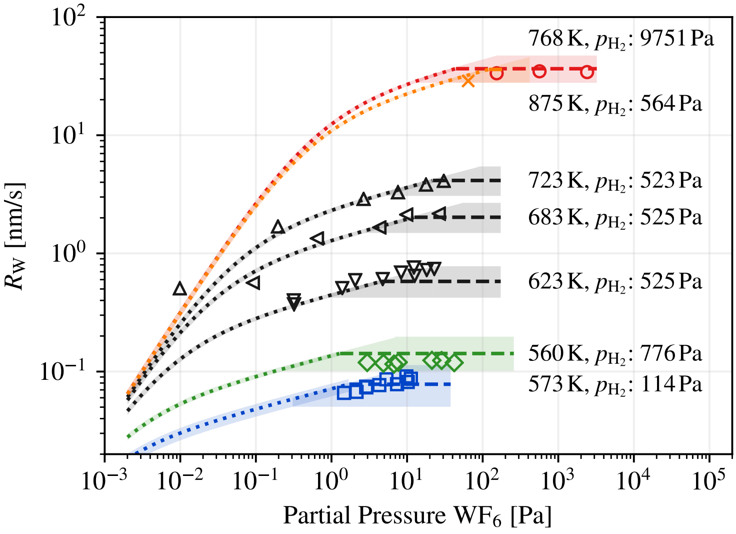

Figure 3.16: Lines: R_W [Equation 3.10], as minimum of $R_{WF_6 dep.}$ (····) and $R_{WF_6 indep.}$ (- - -), vs. experimental data: ×○ this work, with $R_{max,tube}$ for #1089 (×) and #1097 – 1099 (○), △◁▽ Oosterlaken [76], ◊ Pauleau [78], □ Van der Putte [85].

Furthermore, the experimental results of Pauleau et al. (◊) [78] show always $n_{WF_6} = 0$, even though p_{WF_6} reaches lower values than at the transition point observed by Van der Putte et al. (□) [85]. This is just as well covered by Equation 3.10, as the p_{WF_6} value, for which n_{WF_6} changes, is strongly depending on T. Therefore, the transition point shifts to lower p_{WF_6} in the case of lower T, as it was used by Pauleau (◊) compared to Van der Putte (□). In addition, the reason for the higher R_W, despite the lower T (still ◊ vs. □), is the higher p_{H_2}.

This explains why Pauleau et al. [78] and many others did not observe any p_{WF_6} dependence, even though partly reaching higher R_W and/or lower p_{WF_6} compared to the authors reporting a clear p_{WF_6} dependence. On the other hand McInerney [84] and Oosterlaken [76] observed only a p_{WF_6} dependence, because most of their experiments had significantly lower p_{WF_6} and higher T. Although Oosterlaken et al. [76] reported the p_{WF_6} dependence for all their data, with this updated point of view, the data points on the right side of the series (◁, ▽) may well be reinterpreted to follow the change in rate equations. Using a rate equation being independent of $p_{\mathrm{WF_6}}$ down to very low $p_{\mathrm{WF_6}}$ of few Pascal, as suggested by Kleijn et al. and Hasper et al. [100, 101], would overestimate R_{W} compared to the results of McInerney (····), Oosterlaken (△◁▽) and Van der Putte (□). In addition it would also not fit to the experimental results from this study such as #1089, and #1101 (Figure 3.14a). The rate equations are limited to $p_{\mathrm{WF_6}} < p_{\mathrm{H_2}}/3$ as there is not yet sufficient data for higher $p_{\mathrm{WF_6}}$. Furthermore, the experimental $p_{\mathrm{WF_6}}$ variation of Creighton [91] is not included due to unknown T values and due to unusually high R_{W} for the reported pressure regime.

Taking into account the results of various authors together with the new findings of this work, the overall understanding of the W deposition kinetics is proposed as follows. Figure 3.17 shows a sketch, which is divided into four zones for the different reaction orders.

Zone I For $p_{\mathrm{WF_6}} << p_{\mathrm{H_2}}$, R_{W} increases linearly with $p_{\mathrm{WF_6}}$ [82, p. 95] [84, 91]. Here the surface is saturated with H_2 so that $n_{\mathrm{H_2}}$ goes against zero and the incoming F atoms of each adsorbed WF_6 molecule can be directly carried away by already on the surface dissociated H atoms [91, 102]. Thus WF_6 adsorption is the rate-limiting step.

Transition zone I → II With increasing $p_{\mathrm{WF_6}}$ the amount of H on the surface is reduced continuously. Thus, near the transition for I → II, $n_{\mathrm{WF_6}}$ changes smoothly from 1 to 1/6 and $n_{\mathrm{H_2}}$ from 0 to 1/2 [84]. In fact, Creighton's investigations of the $p_{\mathrm{H_2}}$ dependence [91, Fig. 3] showed the existence of this transition with $n_{\mathrm{H_2}}$ values between 0 and 1/2

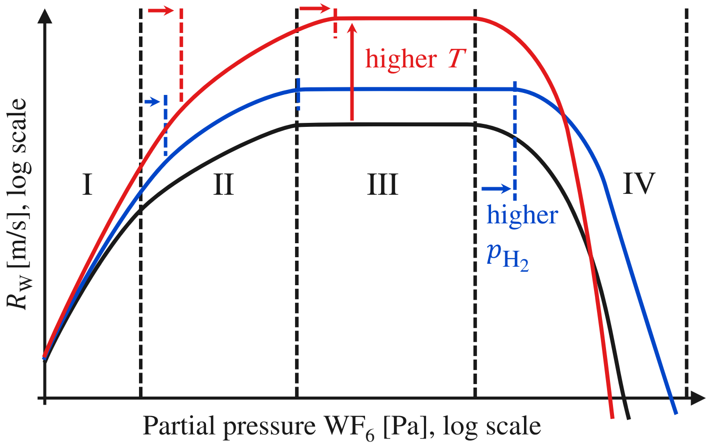

	$n_{\mathrm{H_2}}$	$n_{\mathrm{WF_6}}$
I	0	1
II	1/2	1/6
III	1/2	0
IV	n.a.	< 0

Figure 3.17: Schematic behavior of R_{W} versus $p_{\mathrm{WF_6}}$ divided by black dashed vertical lines into four zones of different reaction orders $n_{\mathrm{H_2}}$ and $n_{\mathrm{WF_6}}$, which allows to combine different results from literature and this thesis. The colored dashed vertical lines mark the repositioning of the zone transitions for changing T or $p_{\mathrm{H_2}}$. In this sketch the curves are based on equations only in the zones I–III.

Zone II The rate-limiting step in this zone is suggested to be HF desorption [76, 84] or the conversion of WF_4 to WF_3 [89].

Transition zone II → III Finding the existence of the transition from Zone II to III (Figure 3.14a, Figure 3.16) and a quantitative description (Equation 3.10), is a major outcome of the presented work. However, it should be noted that the transition is in reality smoother than it results from Equation 3.10 (s. Figure 3.14a). It is possible to smoothen the transition by using Equation 3.12.

$$R'_{sim} = \left(\frac{1}{[R_{\mathrm{WF}_6 dep.}]^m} + \frac{1}{[R_{\mathrm{WF}_6 indep.}]^m} \right)^{-1/m} \tag{3.12}$$

with $m = 1$ resulting in that R'_{sim} significantly underestimates R_{exp}, and with $m \to \infty$ resulting in that R'_{sim} converges to R_{sim} (Equation 3.10). A value in between would result in a better match. However, Equation 3.12 is not involved in the presented simulations, because it strongly increases the computational effort while having only a small influence on the results, and this only at the transition. In addition, more experimental data would be required first to acquire a value for m.

Zone III Most results in the literature and this work can be found for this zone with $n_{\mathrm{WF}_6} = 0$ (p_{WF_6} independence) and H_2 dissociation being the rate-limiting step [77–82]. The height and width of the plateau in Figure 3.17, as a function of T and p_{H_2}, is determined by the semi-empirical constants E_A and k_0. This zone provides typical and stable process conditions for ULSI technology without oversaturation of any of the species, so that R_{W} is least affected by depletion. Therefore, also pore infiltration processes, such as the synthesis of W_f/W, should be driven here for the most possible uniform pore filling. With the help of the presented model, $\dot{V}^{inlet}_{\mathrm{WF}_6}$ can be determined to be as low as possible for low production costs, and as high as necessary to safely stay in Zone III.

Zone IV For p_{WF_6} higher than a value in between $p_{\mathrm{H}_2}/3$ and p_{H_2}, F becomes the majority surface species and hinders H_2 adsorption and dissociation, so that R_{W} decreases again [89, 91]. As shown by Creighton, this can lead to the extreme that R_{W} becomes even negative due to etching [91]. To safely avoid this the ratio of p_{H_2} to p_{WF_6} should be kept ≥ 3.

3.5 Simulation enhanced input for the Arrhenius plot

This section describes the procedure for obtaining the values for E_A and k_0 as they are given in Equation 3.10b. By dividing Equation 3.10b by $p_{\mathrm{H}_2}^{1/2}$ and taking the natural logarithm one obtains a linear equation. E_A and k_0 can be obtained from the slope and y-axis section, respectively. To plot the data points to which the linear fit can be applied, R_W data with its corresponding T and p_{H_2} is needed. R_W can be obtained *post* deposition (Section 3.1.2). For the R_W data in the Arrhenius plot $R_{exp,max}$ along each fiber and tube was taken (Table 9.2, Table 9.3), as here, transient effects play a minor role in contrast to at the flanks of the R_W curves. However, the corresponding T and p_{H_2}, which were actually present *during* the deposition, cannot be obtained trivially:

Step 1 As first estimation, T was set to T_H, and p_{H_2} was estimated via P_{tot} multiplied by $\dot{V}^{inlet}_{\mathrm{H}_2}$ divided by $\dot{V}^{inlet}_{tot}$. This data was used to create an Arrhenius plot ($\ln(R/p_{\mathrm{H}_2})$ vs. $1/T$) with two data points (fiber, tube) for each of the 15 process parameter sets. The result is shown together with literature data in Figure 3.18a. Using Python SciPy [103] for linear fitting, E_A results here in $(75.9 \pm 1.6)\,\mathrm{kJ/mol}$, and k_0 in $(10.34 \pm 1.08)\,\mu\mathrm{m\,s^{-1}Pa^{-1/2}}$.

Step 2 The estimation of T and p_{H_2} at the position, where $R_{exp,max}$ was measured, can lead to large errors. For example, at the fiber surface of #1096 T was significantly lower than T_H due to convective cooling (similar to the final result shown in Figure 3.11). Furthermore, p_{H_2} near the fiber and tube surface of #1101 was significantly lower than p_{H_2} at the inlet, due to its consumption (similar to Figure 3.13 in Section 3.3).[1]

Higher T (moving left in the Arrhenius plot) lead to larger U_i, lower p_{H_2}, and thus lower R_W (points are shifting downwards in the Arrhenius plot), resulting in the underestimation of E_A if the value for p_{H_2} is taken from the inlet. A model is capable of taking this as well as convective cooling into account. Therefore, as next input for the Arrhenius plot the estimated T and p_{H_2} values were replaced by simulated (Section 3.2) values taken from the same location at which the corresponding R_{sim} values were maximal. However, changing E_A and k_0 as input for the simulation results also in new values for the simulated T and p_{H_2}. This loop dependence was solved iteratively. As convergence criterion was chosen that E_A remains constant in a tenths of a kJ/mol.

Step 3 The described procedure is applicable for determining E_A and k_0 with respect to the case that R_W is independent of p_{WF_6} (Zone III). However, for #1089, $R_{sim,max}$ does not match to $R_{\mathrm{WF}_6 indep.,max.}$ (Equation 3.10b) but instead to $R_{\mathrm{WF}_6 dep.,max.}$ (Equation 3.10a). Therefore, it should not be considered in this Arrhenius plot and was removed. The final Arrhenius plot resulting from another iteration cycle is shown in Figure 3.18b. R_W, T and p_{H_2} used as input are provided in the Appendix in Table 9.2 and Table 9.3.

---

[1] The latter could have been also the reason for an underestimation of E_A in a previous work (57.5 kJ/mol, [80]), where a very low P_{tot} of 20 Pa but a still relative high T of > 800 K was used. Thus, due to consumption, the assumption of a constant p_i at the position of R_W measurement was most likely not valid anymore.

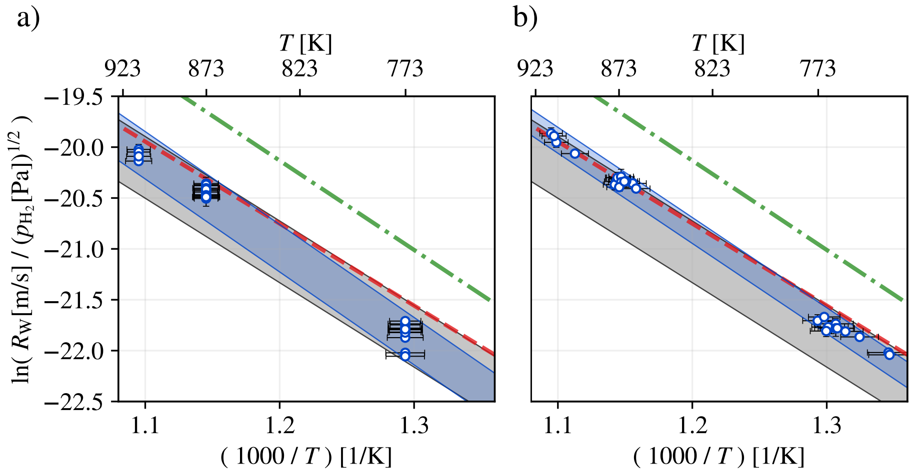

Figure 3.18: Arrhenius plots with linear fits (▭) to the data points (○), which result from $R_{exp,max}$ and a) $T = T_H$, and p_{H_2} estimated via inlet flow ratios, b) T and p_{H_2} taken from the simulation, where $R_{sim} = R_{sim,max}$, and using only the data being independent of p_{WF_6}. Literature data: -·- McConica [79], --- Bryant [81], ▒ Broadbent [77].

The resulting E_A of (73.7 ± 0.9) kJ/mol is similar to that of McConica [79], however, with a lower k_0 of $(38.22 \pm 4.85)\,\mu\text{m}\,\text{s}^{-1}\text{Pa}^{-1/2}$, so that the y values match to the results of Bryant [81] and Broadbent [77].

The changes in E_A and in the relative k_0 fitting error ($\Delta k_0/k_0$), resulting from the different Arrhenius plot inputs, are summarized in Table 3.3. Due to the enhanced input from the iterative simulations the final values after Step 3 should be suited best. This is supported by the fact that the resulting $\Delta k_0/k_0$ got significantly smaller.

Table 3.3: Influence of different Arrhenius plot input on E_A and on the relative k_0 fitting error, as explained in the three steps in this section.

	Input for			E_A	$\frac{\Delta k_0}{k_0}$	
Step	T	p_{H_2}	filter	[kJ/mol]	-	Fig.
1	T_H	inlet, estimated	none	75.9	0.23	3.18a
2	simulated at $R_{sim,max}$		none	72.8	0.18	
3	simulated at $R_{sim,max}$		p_{WF_6} indep.	**73.7**	**0.13**	3.18b

3.6 Chapter summary and conclusions

The dependence of the W deposition rate (R_{W}) on the $\mathrm{WF_6}$ partial pressure ($p_{\mathrm{WF_6}}$) is discussed controversially in the literature. The experimental results and considerations of Van der Putte [85] and Creighton [91] indicated already that the $p_{\mathrm{WF_6}}$ dependence is determined by $p_{\mathrm{WF_6}}$ and $p_{\mathrm{H_2}}$. However, no quantitative description was available. This gap was addressed in this work. For the commonly used case of $\mathrm{H_2}$ over-stoichiometry, the resulting rate equation describes well the most experimental data in the literature and all the data in this thesis.

The rate equation (Equation 3.10a) from McInerney et al. [84], which depends on $p_{\mathrm{WF_6}}$, is found to be valid only for low $p_{\mathrm{WF_6}}$. On the other hand the commonly used rate equation, which is independent of $p_{\mathrm{WF_6}}$ (Equation 3.10b), is found to be valid only for higher $p_{\mathrm{WF_6}}$ (but $< 3\,p_{\mathrm{H_2}}$). The $p_{\mathrm{WF_6}}$ value, which marks the transition between the low and high $p_{\mathrm{WF_6}}$ regime, depends mainly on the temperature (T) and negligibly on $p_{\mathrm{H_2}}$. This dependence can be included self-consistently by taking always the minimum of Equation 3.10a and Equation 3.10b, which describes the reaction limiting step. The resulting combined rate equation (Equation 3.10) was implemented in a transient 2D axial symmetric Comsol model, including the complex coupling of energy and mass transport phenomena with chemical reaction kinetics. In addition to the validation of R_{W} via optical microscopy, simulated T profiles were validated by measuring near-surface T profiles in high spatial resolution. Furthermore, the simulated partial pressures were validated indirectly via the $\mathrm{WF_6}$ consumption rate, deduced from experimentally $\mathrm{WF_6}$ flow rate and W mass gain measurements.

For the low $p_{\mathrm{WF_6}}$ regime, the semi-empirical constants E_A, k_1, and k_2 from Ref. [84] led already to a good agreement. However, for the high $p_{\mathrm{WF_6}}$ regime, the values for E_A and k_0 found in literature had to be adjusted. By simulating T and $p_{\mathrm{H_2}}$ at the actual reaction location, the input for an Arrhenius plot was improved, which lowered the fitting error significantly. In this way, E_A and k_0 resulted in $(73.7 \pm 0.9)\,\mathrm{kJ/mol}$ and $(38.22 \pm 4.85)\,\mu\mathrm{m\,s^{-1}Pa^{-1/2}}$, respectively.

In this chapter, W-CVD was successfully described on a single W fiber. As next step and in the following chapter, W-CVD is described on multiple W fibers. For this, the new rate equation presented and validated in this chapter will be applied. The new equation allows to predict R_{W} quantitatively as function of T, $p_{\mathrm{H_2}}$ and $p_{\mathrm{WF_6}}$ for a much larger $p_{\mathrm{WF_6}}$ range compared to what was previously available in the literature. This is particularly necessary to comprehensively model the production of W_f/W, where $p_{\mathrm{WF_6}}$ should start high, but eventually decreases to zero within the pore structure. Furthermore, to model the $\mathrm{W}_f\mathrm{W}$ production, the complex interaction between the gas and the CVD-W surfaces growing until contact must be added as described in the following chapter.

4 Modeling and validation of W-CVD between multiple fibers

The structure of this chapter is illustrated in Figure 4.1. The first section is dedicated to the experimental part. It is subsectioned in CVD substrate (W fabrics) production, CVD procedure, and pore structure evaluation. Regarding the modeling, a multi-scaled approach had to be chosen to reduce the needed computational power. A macro-scaled stationary CVD model for the entire reactor geometry, which will henceforth be referred to as "Reactor Model" is presented in the second section. This model gets as input

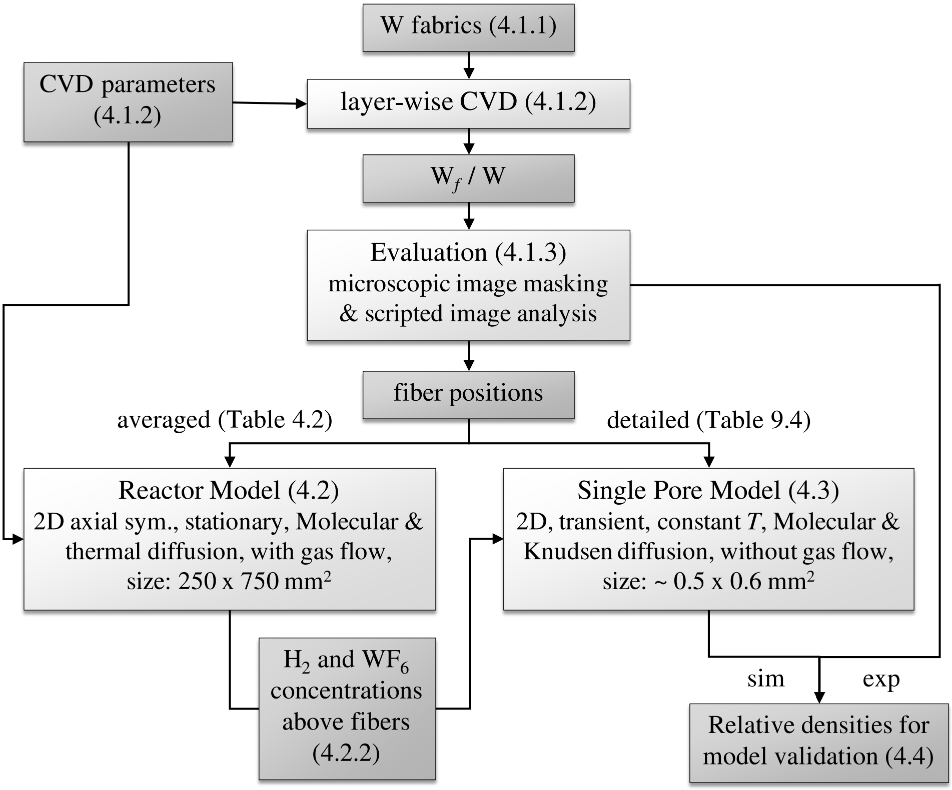

Figure 4.1: Flow chart illustrating the structure of the present Chapter 4, including the relations between the sections.

the averaged fiber positions from the experimental evaluation, and the CVD process parameters as used in the experiment. As output, the model returns the gas species concentrations above the fibers, which are needed as input for a separate transient microscaled model, which will henceforth be referred to as "Single Pore Model". This model is presented in the third section. Additional inputs are the detailed experimental fiber positions. This model returns the relative densities (ρ_{rel}) for each pore, which are compared to the experimental results in the fourth and last section, with the validation of the models being the goal of this chapter.

4.1 Experimental

Three layered W_f/W samples have been produced in cooperation with Hanns Gietl from the IPP Garching, as described in the following sections.

4.1.1 Substrate production (fabric weaving)

As first step, W fabrics were produced with a shuttle loom [54] in cooperation with the ITA [104] at RWTH Aachen University. After around fifty iterations, the result was to produce five fabric types with different warp fiber distances (Figure 4.2), with a weft fiber distance of ca. 3 to 4 mm, and with the warp and weft fibers having a diameter of 150 µm, and 50 µm, respectively. To increase the fabric stability and the fiber volume fraction, the shuttle loom (Figure 4.3a) was equipped with a roll (Figure 4.3b) to flatten the fabric after weaving under plastic deformation of the weft fiber (Figure 4.3c → d) [105].

4.1.2 Setup and procedure

The fabrics were cut, clamped into holders, coated by physical vapor deposition with an Y_2O_3 interface of 1–2 µm thickness (Section 2.3), and mounted into the CVD device "WILMA" (W infiltration machine) located in the Research Center Jülich, IEK-4 [106]. A photo of WILMA and the present geometries is shown in Figure 4.7 within Section 4.2 (Reactor Model description). The fabrics were placed on a heating table within the vacuum vessel. The precursor gas entered from top of the table and the gas outlet was located below the table. The vacuum vessel was heated to 523 K in order to reduce the adsorption of WF_X. As developed by J. Riesch [48], the W_f/W was produced layerwise, which means that for each fabric layer a separate CVD run was done.

A uncoated fabric for the next layer was placed on an already W-CVD-coated fabric of the previous CVD run (see labels for previous and next layer in Figure 4.4). With each of the fabrics (Figure 4.2) three-layered W_f/W samples were produced. The applied CVD process parameters are listed in Table 4.1. The deposition time for each layer has

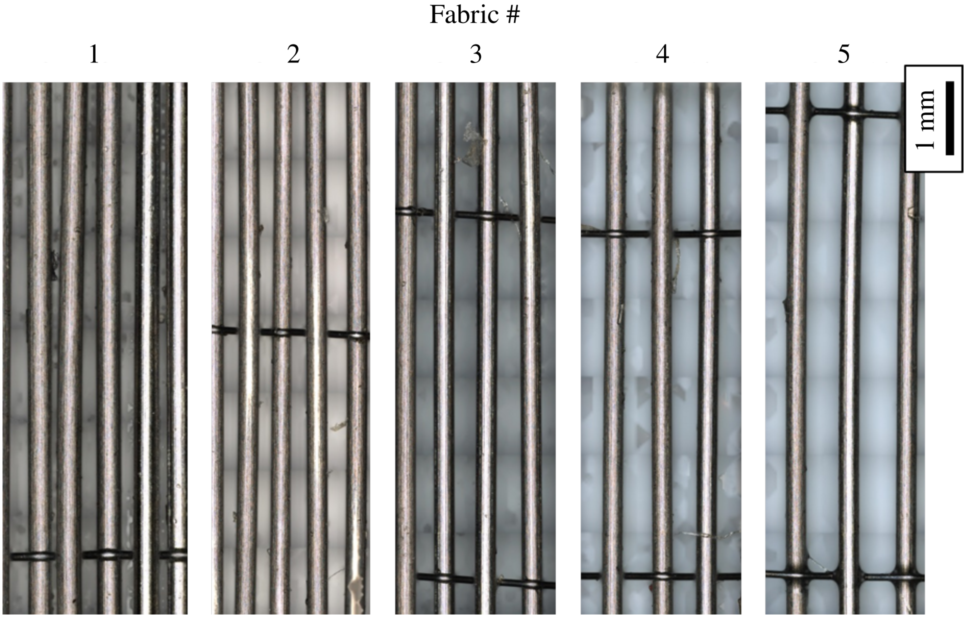

Figure 4.2: Sectioned photos of the five fabrics with different warp fiber distances, which were used as substrate for the W_f/W synthesis via CVD [54, 105].

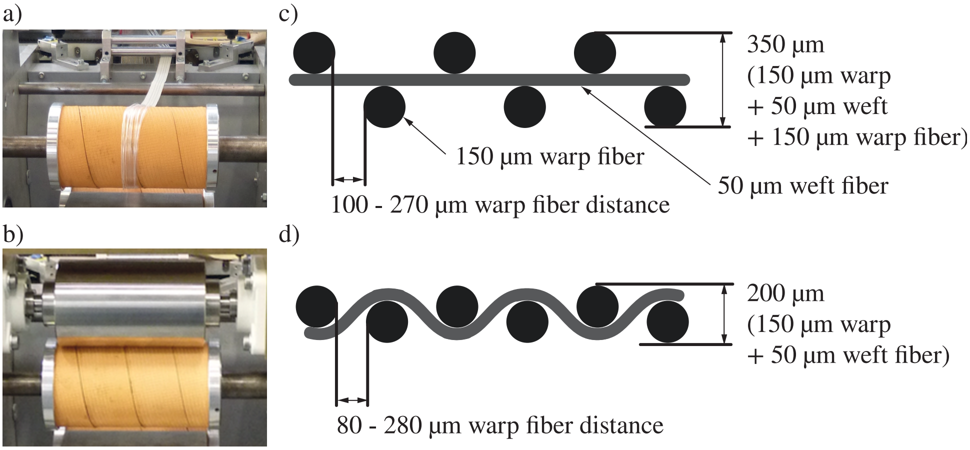

Figure 4.3: W fabric production. Photographs of the shuttle loom without (a) and with (b) the additional roll, and schematics of the produced W fabrics without (c) and with (d) the additional roll [54].

been estimated with a large margin, so the CVD-W surfaces growing on adjacent fibers will certainly grow until surface-to-surface point contact and beyond.

A thermocouple, which was plugged centrally into the inner of the heating plate, was controlled to 873 K (T_{heater}). Another thermocouple (for $T_{surface}$) was placed onto the

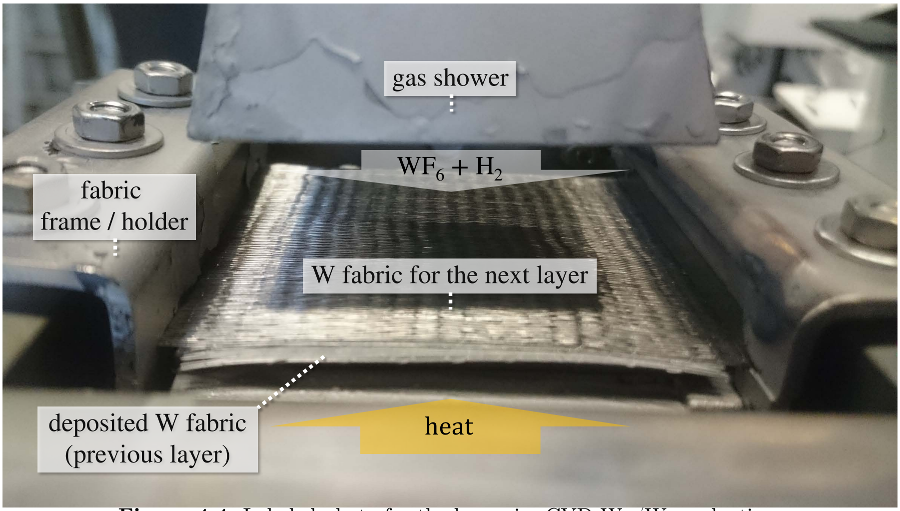

Figure 4.4: Labeled photo for the layerwise CVD W_f/W production.

Table 4.1: CVD process parameters used for the first layerwise W_f/W production.

T_{heater}	873	K
$T_{surface}$	830 ±10	K
P_{tot}	9.5	kPa
$\dot{V}_{H_2}^{inlet}$	1500	sccm
$\dot{V}_{WF_6}^{inlet}$	400	sccm
Δt	45	min

fabric at an outer edge. $T_{surface}$ was 786 K at the beginning and raised to 839 K until the end of the deposition. The reason is that, while the CVD-W grows, firstly the thermal contact between thermocouple and fabric is improved. Later on, the thermocouple is covered by CVD-W reducing the convective cooling. As simplification $T_{surface}$ is estimated to the constant averaged value of 830 ±10 K.

4.1.3 Sample selection and evaluation

Modeling the infiltration of a W fabric with remaining pores is a lot more complex than without pores. The reason is that stronger precursor gradients have to be taken into account, which also influences the diffusion mechanisms. Therefore, it was decided to focus the evaluation and modeling on fabric #1 (the left one in Figure 4.2), which had the most and the largest pores as the warp fiber distances were the smallest.

The W_f/W samples were embedded, sliced in the middle, and polished for microscopy. With the normal view mode of the microscope and with medium brightness, the pores appear larger than they are. The reason for this is that the W edges within the metallographic cut are rounded during polishing. Therefore, much of the incoming light is scattered instead of being reflected into the camera. With respect to SEM images, a match of the pore appearance with the correct edge locations could be achieved also for optical microscopy by using maximum brightness and the dark-field mode. The dark-field images were masked with a procedure described in detail in the Appendix (Section 9.3.1). An example for the masking input and outcome is shown in Figure 4.5 a) and b), respectively.

The fiber coordinates, relative density (ρ_{rel}), and fiber volume fraction (Φ_{V_f}) were obtained via a scripted image analysis as described in the next subsection.

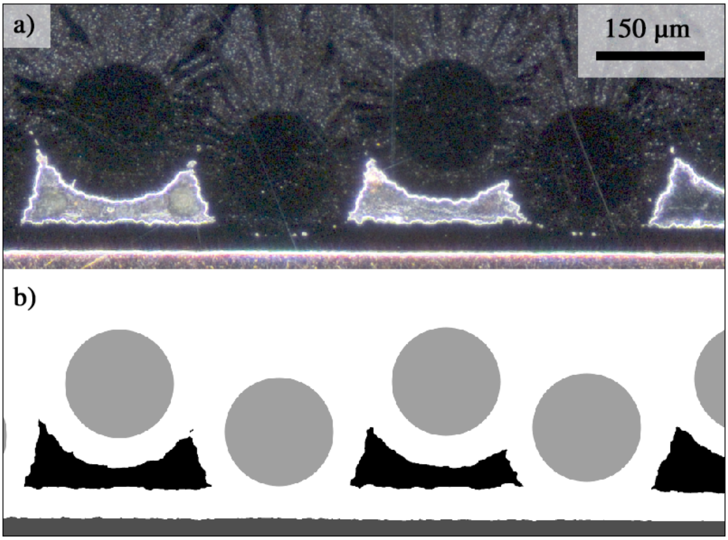

Figure 4.5: Part of the first layer of W_f/W produced by deposition of fabric 1. a) dark-field optical microscope image, b) masking result used as input for the following Python script.

4.1.3.1 Python script to evaluate W_f/W

Input: Masked microscopic image of a W_f/W first layer cross section.
Output: For each pore between 3 fibers: local fiber x-, y-coordinates, ρ_{rel} and Φ_{V_f}.

1. The masked image is converted to a 2D array with one value per pixel, whereas 0 = pore, 0.33 = ground, 0.66 = fiber, 1 = CVD-W. The µm-to-pixel ratio was 0.5052955.

2. The Skimage library for Python [107] was implemented to find firstly the edges or contours between the different masked areas, and secondly, based on that, the fiber centers (marked as + in Figure 4.6).

3. By comparing the values of the array from step 1, the script finds for each fiber the y position of the ground surface (marked as × in Figure 4.6).

4. By using the coordinates from the steps 2 and 3, the control area ($A_{control}$), marked as green transparent and asymmetric trapeze in Figure 4.6, is defined for each pore and its area in pixel^2 is calculated via Equation 4.1.

$$A_{control} = x_2 \frac{y_1 + y_2}{2} + (x_3 - x_2)\frac{y_2 + y_3}{2} \tag{4.1}$$

with $A_{control}$: control area [m^2]
x, y : fiber center coordinates [m]
1, 2, 3 : left, middle, and right fiber

5. In each $A_{control}$, the area of the pore (A_{pore}) and of the fiber parts (A_{fiber}) are calculated. The script loops through the entries in the array from step 1, and adds the ones with a value = 0 to A_{pore} and with a value = 0.66 (see step 1) to A_{fiber}.

6. For each pore, ρ_{rel} and Φ_{V_f} are calculated via Equation 4.2a, and b, respectively, and tabulated together with the ground surface and fiber coordinates in µm. The coordinates refer to a single pore-based local coordinate systems, with the origin being defined at the x-value of the left fiber and at the surface of the ground (heating plate) below the left fiber as shown in Figure 4.6. Since the x-axis of the local coordinate system was already almost parallel to the global system, the coordinates were not rotated but just shifted in y direction, so that the y values of the surface below the middle and right fiber became zero as well.

$$\rho_{rel} = 1 - \frac{A_{pore}}{A_{control}} \tag{4.2a}$$

with ρ_{rel} : relative density [-]
A_{pore} : pore area [m^2]

$$\Phi_{V_f} = \frac{A_{fiber}}{A_{control}} \tag{4.2b}$$

with Φ_{V_f} : fiber volume fraction [-]
A_{fiber} : fiber area [m^2]

The above described script can be found in the Appendix (Section 9.3.2) and downloaded from [108]. This method of masking the fibers first and then using Python for finding the centers was much faster and more precise than using a microscope software to find circle centers by clicking three or more points along the circumference.

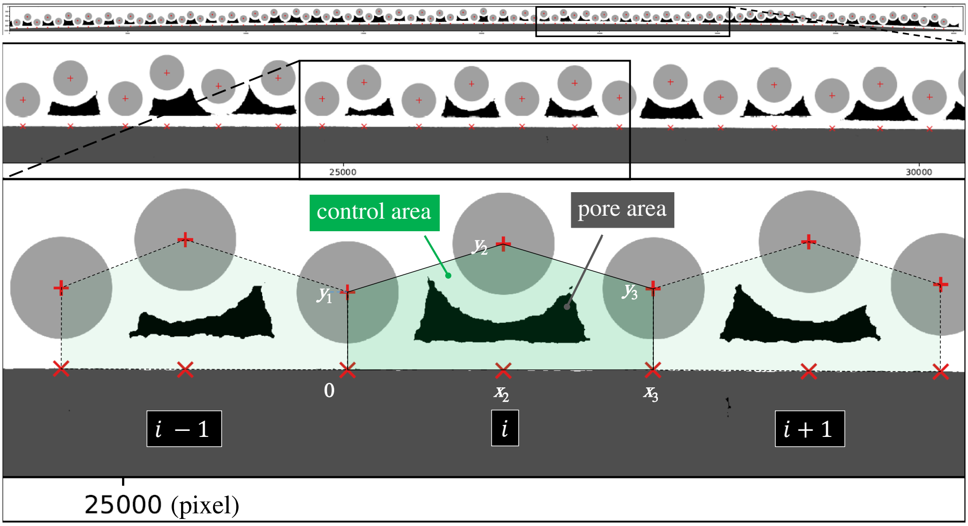

Figure 4.6: Scheme for the evaluation of the fiber coordinates and the pore area of a pore i. The control area is used to calculate ρ_{rel} and Φ_{V_f}.

4.1.3.2 Python script results

The averaged results for the experimental fiber positions and relative densities can be found in Table 4.2. The detailed results can be found in the Appendix in Table 9.4 and will be plotted together with the simulated results after the model description.

Table 4.2: Averaged Python script results for the evaluation of fabric #1, first layer (Figure 4.6).

within the green-marked area from Figure 4.6:			
fiber volume fraction	Φ_{V_f}	22.5 ± 2.5	%
relative density	ρ_{rel}	77.3 ± 7.3	%
fiber coordinates as in Figure 4.6:			
	x_2	222.7 ± 21.6	µm
	x_3	441.0 ± 22.0	µm
	y_1	142.7 ± 25.3	µm
	y_2	225.8 ± 24.3	µm
	y_3	143.4 ± 25.1	µm
averaged values assuming "symmetric" pores:			
horizontal distance between fiber surfaces	X_{ff}	70.5 ± 20.6	µm
vertical distance between lower fiber and ground surface	Y_{fg}	68.1 ± 24.5	µm
vertical fiber displacement	Y'_{ff}	82.1 ± 25.0	µm

The positional deviations are quite noticeable. The reason is that the weft and warp fibers are held together only by low friction and low tension due to the (low) fiber stiffness. Regarding the model validation the deviations have the advantage that each pore is slightly different and thus can be seen as individual small experiment with its own fiber positions, ρ_{rel}, and Φ_{V_f}. The deviations allow for the necessary variation and statistics for a solid model validation of ρ_{rel} with the fiber positions as input. Φ_{V_f} does not need to be validated, since it is already determined geometrically by the fiber positions (model input).

4.2 Reactor Model

4.2.1 Model description

The goal in modeling the CVD reactor is to obtain an estimate for the species concentrations needed as input for the Single Pore Model. The model is in large parts, such as the deposition kinetics and material properties, identical to the Single fiber model (Chapter 3). Therefore, only the differences will be described:

1. CVD process parameters as in the corresponding experiment (Table 4.1).
2. Stationary simulation in order to be able to simulate single 150 µm fibers despite of the large model scale of 0.25 × 0.75 m.
3. New geometry and boundary conditions, which will be explained in the following together with the necessary assumptions (Section 4.2.1.1).
4. Thermal diffusion is included as described in Section 4.2.1.2, as in this setup the thermal gradients perpendicular to the surface become significant.

4.2.1.1 Geometry and boundary conditions

In Figure 4.7 the Reactor Model geometry is shown. As in the experiment, the gas enters through a steel tube that connects to a gas shower, which is aligned above the W fibers and the heating table. The gas outlet is located below the heating table. The background heating temperature T_{bg} is 523 K as in the experiment. The surface temperature of the heating plate $T_{surf} = (830 \pm 10)$ K was also applied directly to the warp fiber surfaces, since in reality there is conductive thermal contact through the weft fibers, which is not considered in this 2D cross section.

The axial symmetry was chosen in order to have a similar gas flow behavior as in reality, where the gas comes from a tube and spreads radially in all directions when hitting the plate. The fibers were modeled via two circles that were cloned by two arrays. The fiber coordinates equaled the averaged values resulting from the image analysis for fabric 1, first layer (Table 4.2). In this way the substrate geometry is identical between experiment and simulation, for the investigated 2D cross section. As the fibers are coated

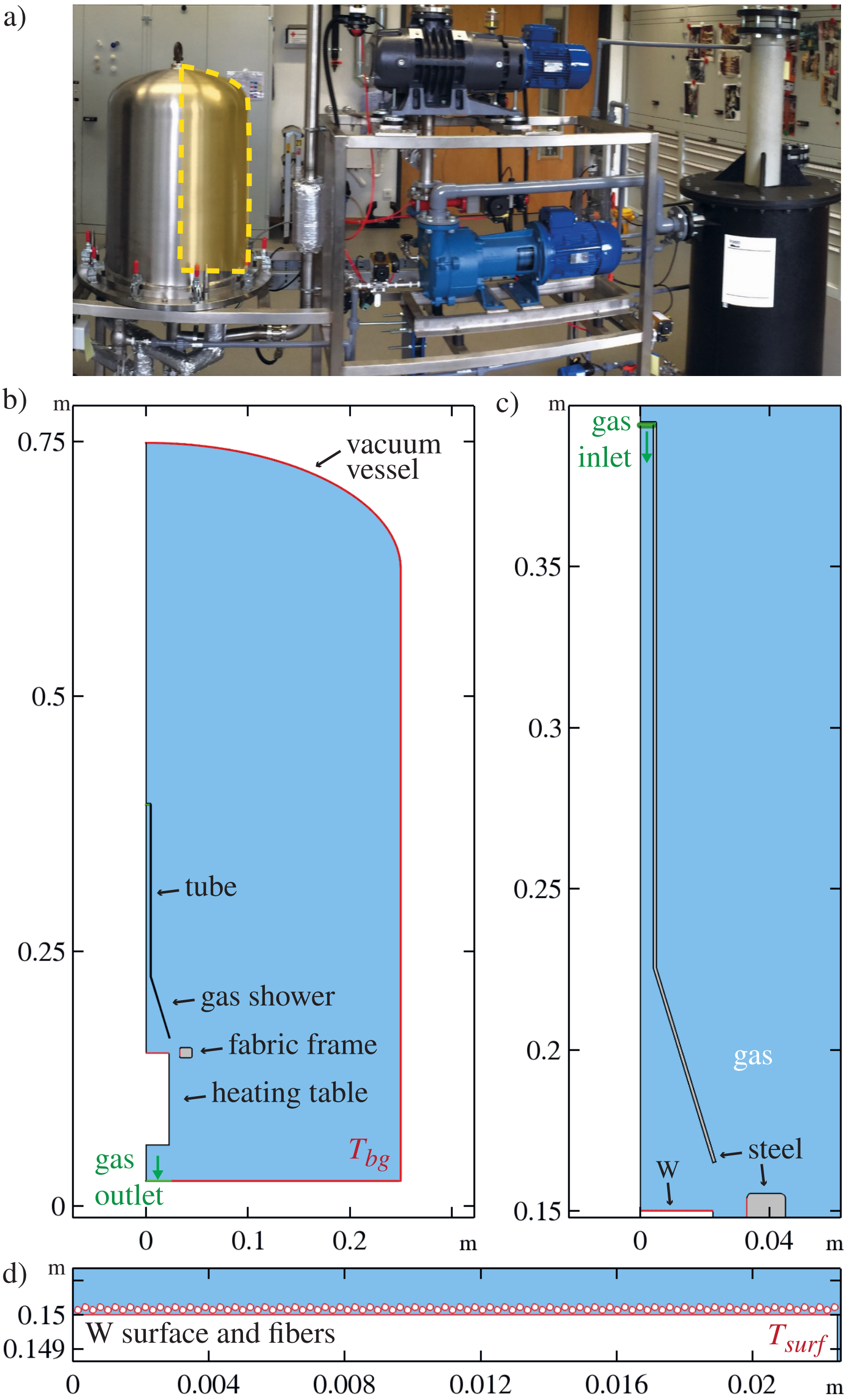

Figure 4.7: a) Reactor Model position within the experimental CVD device, b–d) model geometry with labeled domains and boundaries, c) close-up of the gas shower and heating plate, and d) the heated W fibers.

with CVD-W, their outer radii and thus their total reaction area grow until the surfaces are bonded together after a certain period of time (Δt_c). To take this into account in the simplification of the stationary model, the fiber radius was increased to the value that it would have reached after $\Delta t_c/2$. This is approximately the initial radius (here 75 µm) plus a quarter of the distance between two adjacent fiber surfaces (here 21.3 µm).

4.2.1.2 Thermal diffusion

In a gas mixture with a certain number of species (N) that contains heavy and light molecules, the heavy molecules are repelled from hot surfaces or gas domains and thus the light molecules are concentrated there [76]. This effect is described by thermal diffusion, whereby heavy molecules have a positive thermal diffusion coefficient ($D_{T,i}$) and light molecules a negative $D_{T,i}$. $D_{T,i}$ is depending on the temperature and the mole fractions of the species in the mixture. Its calculation includes the division of the determinants of a ($2N \times 2N$)- and a ($2N \times 2N + 1$)-matrix, whereby each element of the matrices has to be calculated by complex formulas. The calculations and formulas can be found for H_2-WF_6-HF in [82]; however, with two small typographical errors, where one of them has a quite strong impact on the results (In Eq. 2.91 needed for a subelement of the matrices is an i-index, which should be a j-index, as in [95]). To save a lot of computational effort a Python script was written, which prepares the values for $D_{T,i}$ as a lookup table that can be imported and interpolated in Comsol. The script is provided in the Appendix (Section 9.4) and can be downloaded from [108].

In Figure 4.8 D_{T,WF_6}, D_{T,H_2}, and $D_{T,\mathrm{HF}}$ are plotted for different temperatures and for a mole fraction slice from 25% WF_6 and 75% H_2 to 100% HF.

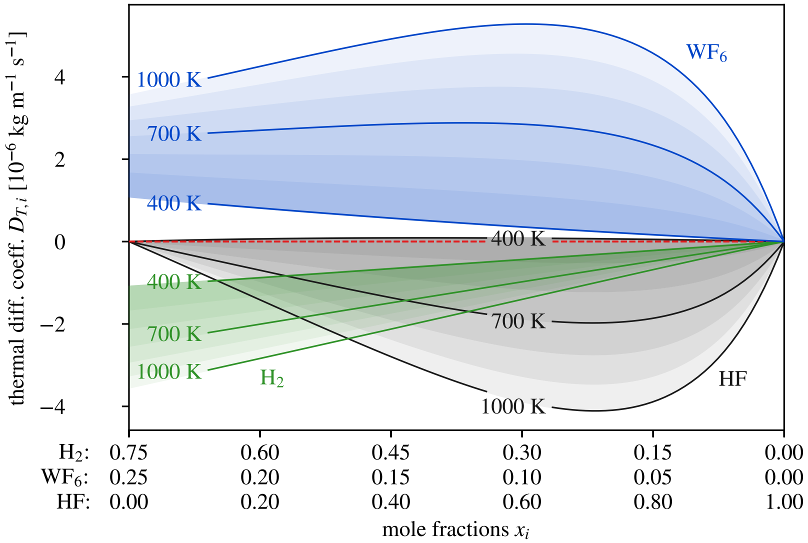

Figure 4.8: Thermal diffusion coefficients of WF_6, H_2 and HF as function of gas composition and T.

As mentioned above, a positive value results in a repelling diffusive flux away from hot surfaces. This flux adds to the ordinary diffusive flux, which is based solely on concentration gradients, and the fluxes due to chemical reactions, until a quasi-stationary equilibrium is reached.

4.2.2 Results

Figure 4.10 to Figure 4.12 show 2D maps of T, gas flow speed, p_{H_2}, and p_{WF_6}. As it can be seen the gas streams out from the gas shower, hits the fabric, is heated up, and is redirected in r direction. The educts WF_6 and H_2 are consumed on the hot substrate, thus their partial pressures decrease in parallel to the gas flow above the surface.

In Figure 4.9 the partial pressures p_i of WF_6, H_2, and HF are plotted as solid lines. The values refer to a distance above the fibers visualized as red marker lines in e.g. Figure 4.10c. These p_i are used as input for the upper boundary of the Single Pore Model. As expected, for the simulated p_i results WF_6 and H_2 decrease while HF increases radially. In Figure 4.9 the p_i values are additionally compared to constant calculated values based only on the inlet gas flow ratio and P_{tot} (dashed lines).

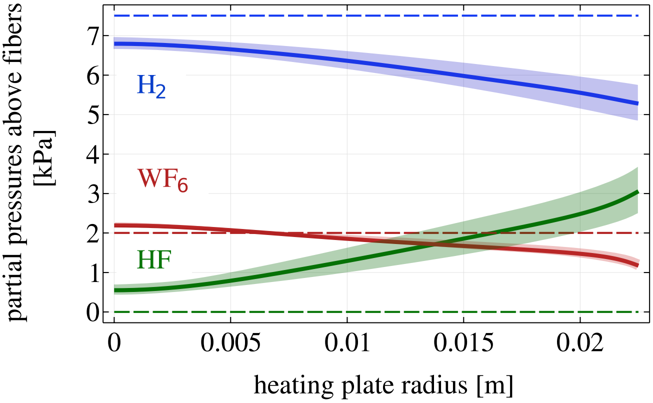

Figure 4.9: Partial pressures p_i above the fibers for H_2, WF_6, and HF versus the heating plate radius. (—): simulation result, (- - -): estimation based on inlet gas flow ratio and P_{tot}.

p_{H_2} starts lower than in the estimation, since HF is already present in the center. However, interestingly, the simulated p_{WF_6} near the center is actually higher than in the estimation. The reason can be seen by comparing Figure 4.11 to Figure 4.12: Within the gas shower the H_2 molecules diffuse outwards much faster than the WF_6 molecules, as H_2 has a much higher diffusion coefficient than WF_6. This phenomenon, caused by the geometry design of the first gas shower, offers an advantage that was only understood after other geometries were tested by simulation. One of those tests was to sent the gas through a tube ending few millimeters above the surface and to redirect it with a plate parallel to the surface.

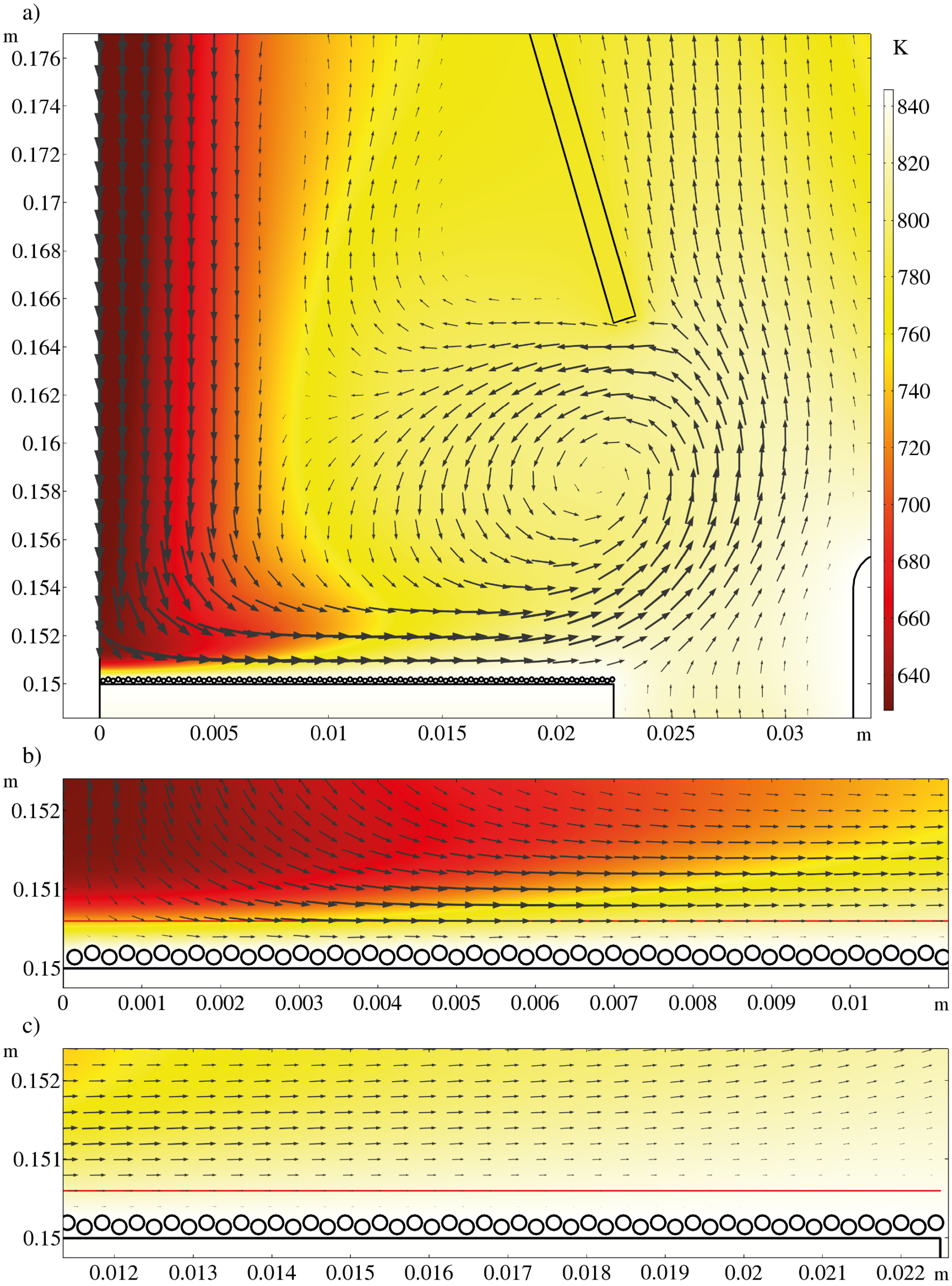

Figure 4.10: Temperature map for the Reactor Model coordinates (y: height, x: radius), and vectors for the total gas flow. a) below the gas shower, b,c) zoomed view around the fibers with b) towards the center and c) towards the edge of the heating plate. The red line marks the height for the Single Pore Model.

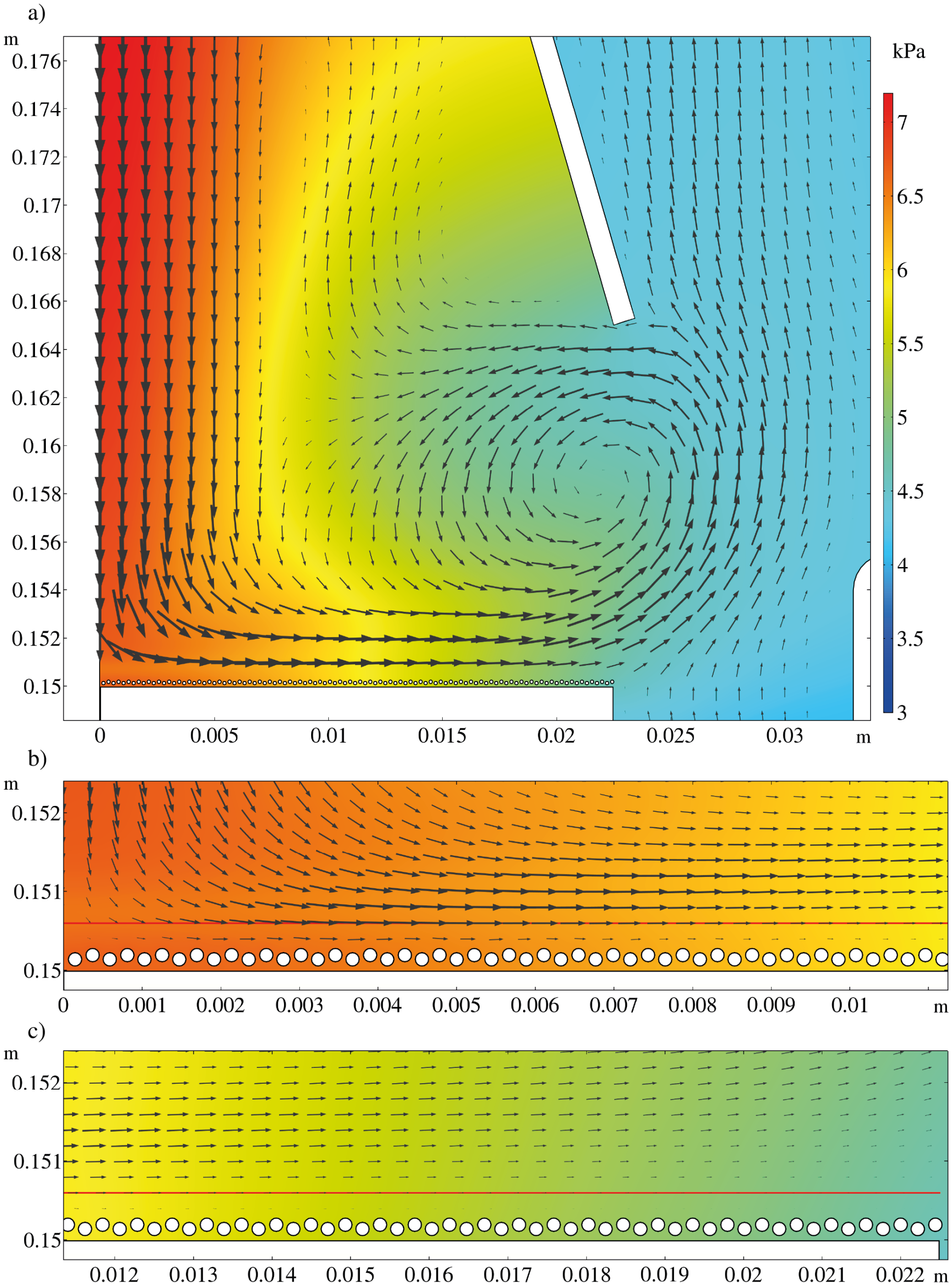

Figure 4.11: H_2 partial pressure in the Reactor Model. Otherwise, same as in Figure 4.10.

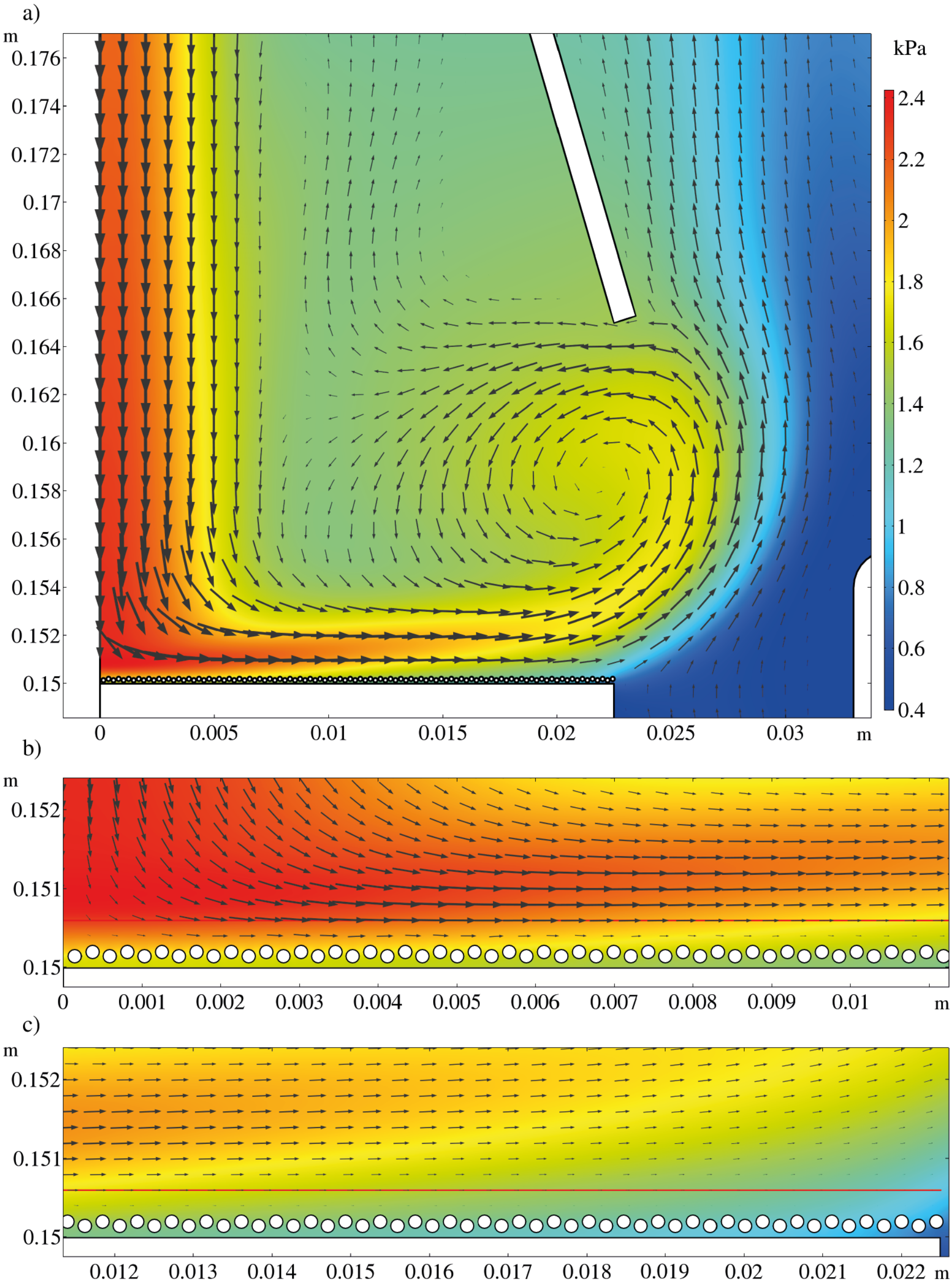

Figure 4.12: WF_6 partial pressure in the Reactor Model. Otherwise, same as in Figure 4.10.

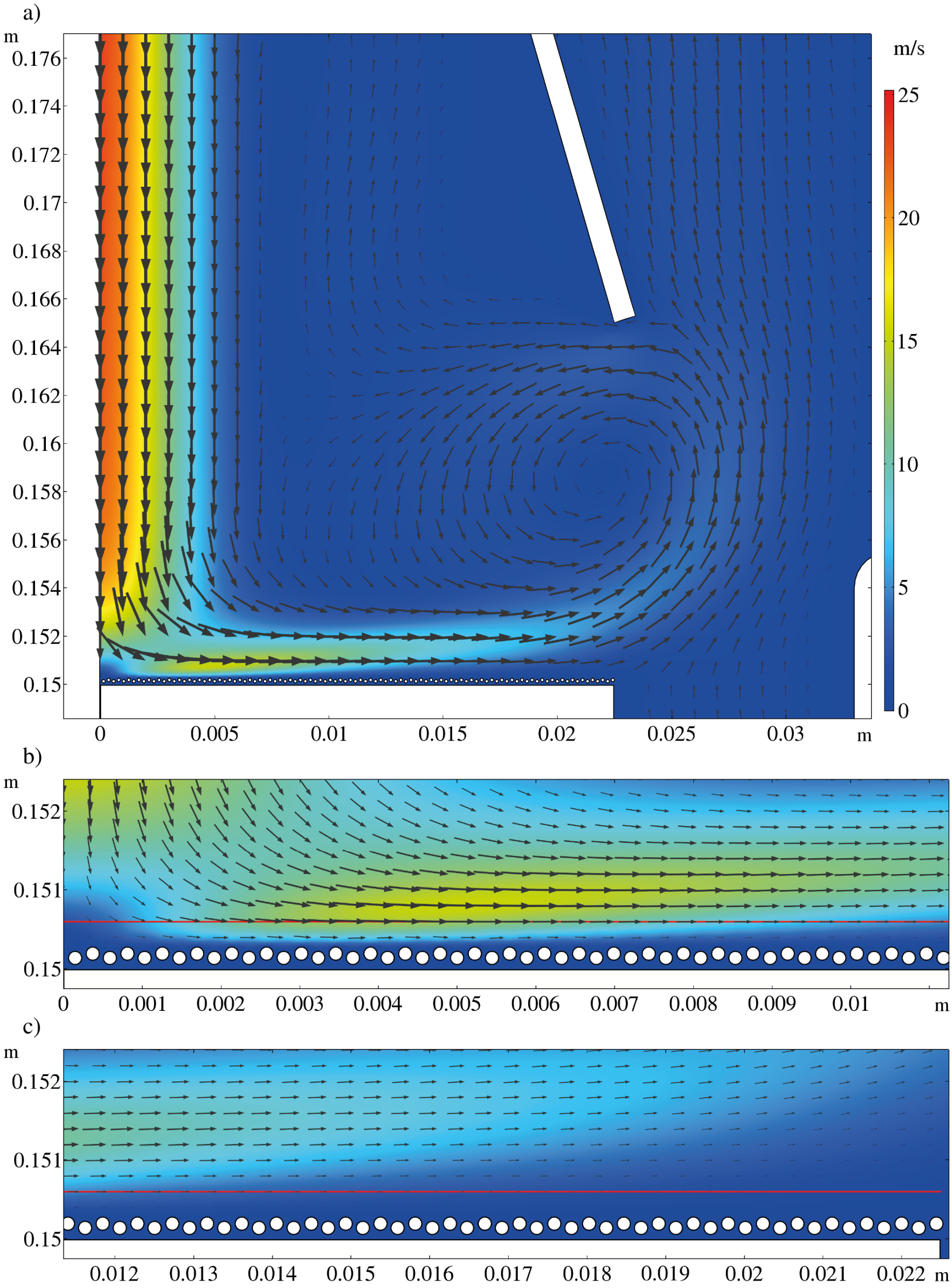

Figure 4.13: Total gas flow speed in the Reactor Model. Otherwise, same as in Figure 4.10.

The result was that R_W was higher in the center, due to a higher p_{H_2}, but lower towards the edge of the fabric, which leads to an increased unwanted macroscopic "bump"-shape of each W_f/W layer. These bumps would stack for each layer making it more and more difficult to place the fabrics evenly. Another test was to use a diffuser within the gas shower (e.g. steel wool), which would result in a radially much more evenly distributed flow rate. The result was that HF was not flushed away well enough leading to a WF_6 depletion at the center of the sample. To conclude, the currently used setup has the advantage that unconsumed WF_6 flushes the HF out of the center, while fresh H_2 diffuses in from above step by step for increasing heating plate radii (r), which leads to a rather uniform R_W along r. By increasing p_{H_2} the difference of R_W in the center and at the edge can be reduced even further as long as R_W stays independent of p_{WF_6} (Zone III).

4.3 Single Pore Model

4.3.1 Model description

The goal of the Single Pore Model is to achieve the same pore structure as obtained experimentally, so that a validated model can be used to tweak the CVD process parameters to improve the W_f/W production with the currently used setup, and to assist in designing new setups in the future. The differences to the Reactor Model are:

1. No axial symmetry (still 2D).
2. Downsized scale by three orders of magnitude regarding model and element sizes.
3. Adjusted boundary conditions and assumptions (constant T, no convective gas flow, constant p_i^{top}, as described in Section 4.3.1.1).
4. Transient simulation for a detailed consideration of the growing CVD surface interaction (Section 4.3.1.2) including Knudsen diffusion (Section 4.3.1.3).
5. Nonstandard configuration of the mesh and the solver in Comsol (Section 4.3.1.4).

4.3.1.1 Geometry and boundary conditions

In Figure 4.14 the geometries and boundaries for the transient Single Pore Model are shown. The weft wire is neglected and included only indirectly via the vertical displacements of adjacent fibers. From the Reactor Model results several simplifications can be justified. Firstly, the quasi stationary equilibrium shows that the p_i gradients in the scale of a single pore, surrounded by three fibers and the ground, can be neglected horizontally. The major gradient is vertical, which can be seen best for p_{WF_6} (Figure 4.12b,c).

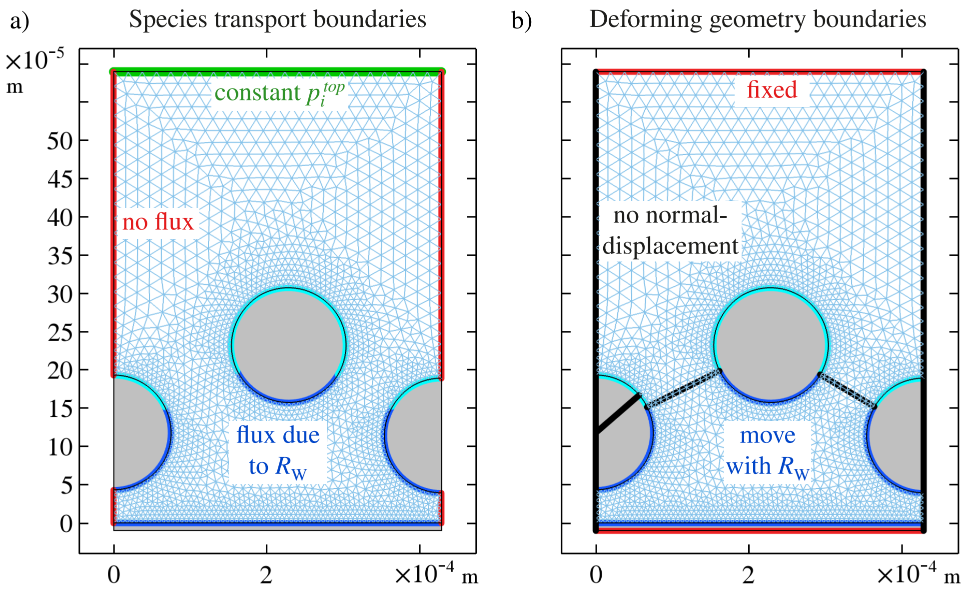

Figure 4.14: Single Pore Model boundaries for a) species transport, b) deforming geometry. Following figures with the same geometry as in this figure have the same axes.

Therefore, the species flux at the geometric side boundaries of the Single Pore Model is set to zero (Figure 4.14a).

Secondly, in the Reactor Model, the gas flow provides fresh educts near the upper fiber surface, whereby the gas flow between the fibers is close to zero (Figure 4.12) and the major species transport into the pores takes place by diffusion. Therefore, in the Single Pore Model the gas flow can be neglected and the transport can be modeled only based on diffusion. p_i^{top} is set constant at the top boundary, which is thus the inlet for H_2 and WF_6 as well as the outlet for HF. The value for p_i^{top} is obtained from the Reactor Model (Figure 4.9), whereby the corresponding radial position (r) is calculated based on the pore ID (Pore#) and the averaged pore distance, with the Pore# being zero in the center and increasing outwardly in integers. Thirdly, it can be seen in Figure 4.10 that T is constant within the pores. Therefore, another valid simplification is to neglect T gradients and thus thermal diffusion at this microscale.

To consider the CVD-W growth, the deforming mesh interface was configured in Comsol as shown in (Figure 4.14b). The cyan boundaries equal the blue boundaries until the pore is sealed. Afterwards, the flux and motion stop at the blue boundary. How this is achieved will be explained next in Section 4.3.1.2.

4.3.1.2 Fiber-to-fiber surface contact problem

If in the current Comsol version (v. 5.4) two domain surfaces approach each other in a transient simulation, two things can happen without extra care. First, the simulation crashes, if the solid domains overlap, caused by a too large final time step. Or second, the simulation will not crash but take infinitely long as the time steps and wall distance become infinitely small. Both outcomes are not favorable. Therefore, the moving surfaces have to be decelerated and then stopped at a certain minimal gap distance. The deceleration is necessary to avoid simulation instabilities caused by discontinuities in R_W along the surface. Furthermore, it helps the simulation to maintain reasonable time step sizes and computing times. The deceleration and stopping can be achieved by adding a factor to R_W, which is a smoothed step function (f_{step}) running from one to zero in dependence of a characteristic length between nearest walls (L_{char}), monitored for each time step. Equation 4.3 is capable of returning L_{char} as needed.

$$L_{char} = \min\left(d_{w,s,f_{1,3}} + d_{w,f_2},\ d_{w,s,f_{1,3}} + d_{w,g},\ d_{w,f_2} + d_{w,g}\right) \tag{4.3}$$

with $d_{w,s,f_{1,3}}$, d_{w,f_2}, and $d_{w,g}$ being the wall distances to the walls as marked in blue in Figure 4.15a, b, and c, respectively.

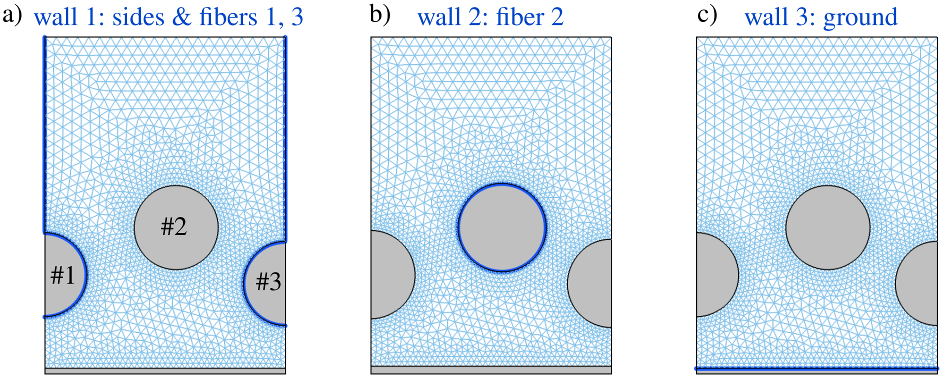

Figure 4.15: Boundary selections to define walls, needed to calculate wall distances.

An example for the results of the wall distances and L_{char} is shown in the following Figure 4.16a, and b, respectively.

As mentioned before, L_{char} can be used as input for f_{step} to slow down and stop R_W. However, by using the reciprocal of L_{char}, instead of L_{char}, the simulation duration is further decreased, and the simulation stability is improved (which is remarkable, since those behave often contradictory, as it is the case for e.g. using a finer mesh). The reason is that the reciprocal of L_{char} changes the stronger the closer the walls approach each other. Thus, the reciprocal is more sensitive within the distance range being of interest

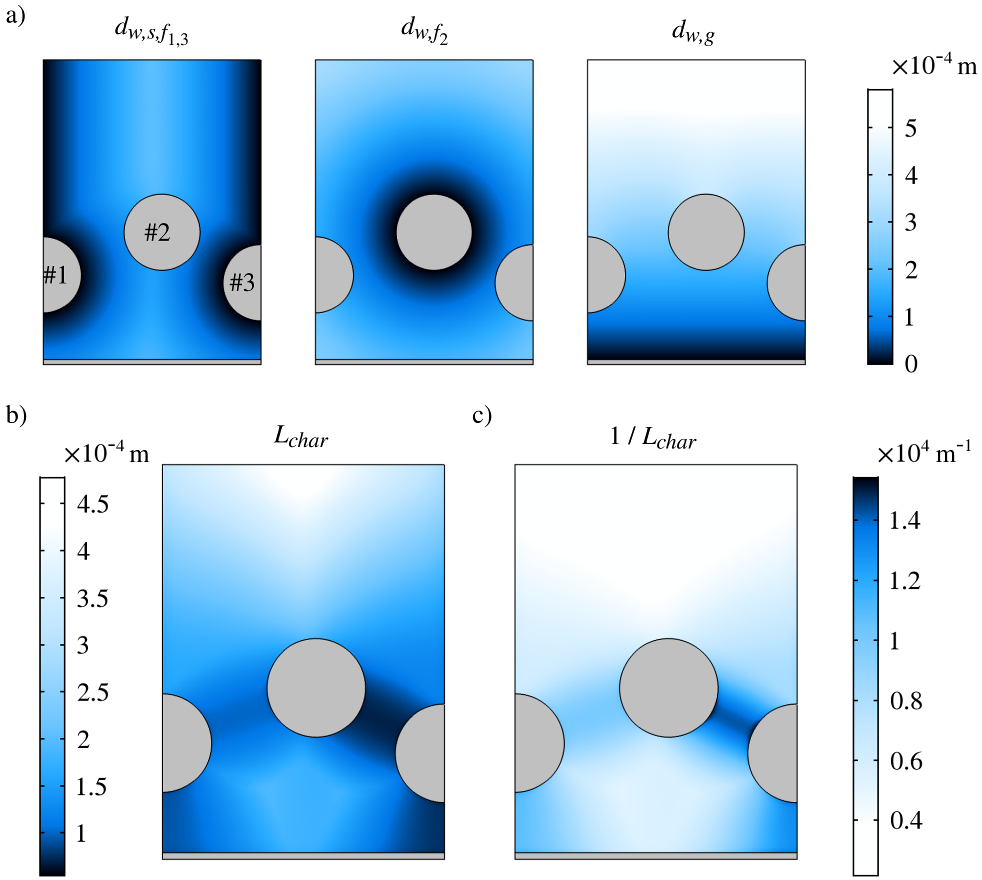

Figure 4.16: 2D color maps for a) the wall distances $d_{w,s,f_{1,3}}$, d_{w,f_2}, and $d_{w,g}$, b) characteristic length between nearest walls L_{char} (Equation 4.3), and c) $[L_{char}]^{-1}$, which can be seen as a field variable tracking the wall to wall distance very sensitively with respect to smaller gap sizes.

for decelerating and stopping R_{W}. The reciprocal of L_{char} is shown in Figure 4.16c). Furthermore, the final wall distance (d_{final}) at which R_{W} becomes zero was chosen to 2 µm. The distance at which the deceleration starts ($d_{decel.start}$) was chosen to $2\,d_{final}$ = 4 µm. The step function $f_{step}([L_{char}]^{-1})$ is plotted in Figure 4.17.

The deceleration and stopping solves the firstly mentioned problem (mesh collision or infinite long simulation), however it causes a series of new problems. The gap is not there in reality and still has got the properties of the gas, since it belongs to the gas domain. Therefore, the gas species can diffuse through this gap into the pore, even if it is only 2 µm broad or less. This phenomenon keeps the deposition reaction and thus pore filling going, which would have stopped already in reality. As of writing this thesis it is not possible in Comsol to transiently divide a domain. If such a feature will be implemented

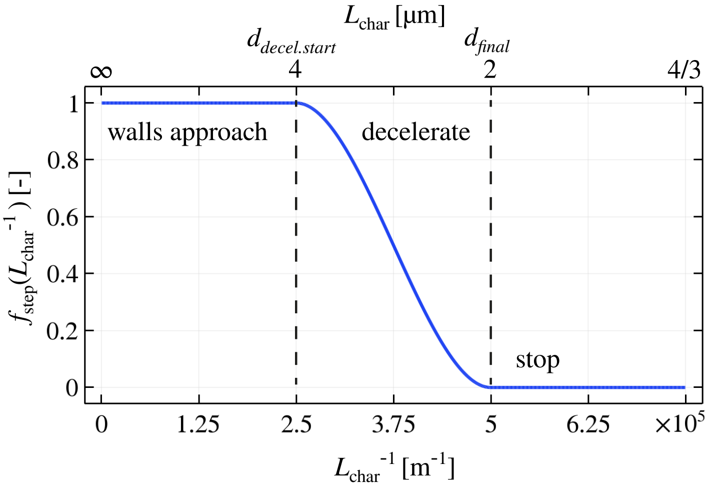

Figure 4.17: Smoothed step function $f_{step}([L_{char}]^{-1})$, which is multiplied with R_W to decelerate R_W if $L_{char} \leq d_{decl.start}$ and to set R_W to zero if $L_{char} \leq d_{final}$.

in future, it will make the simulation of the presented model much easier, much faster, and also more accurate. In the present case the gas domain could then be divided in two separate domains as soon as the gap between the two solid fiber surfaces undercuts a certain threshold. But as this is not (yet) possible, another work-around had to be found, as it is essential that the growing W matrix is able to block off the fresh gas in order to model the resulting pore structure.

Without the needed artificial deceleration and stopping, the pore would be sealed in a point contact when both fiber radii reach half of the connecting line between the fiber centers (l). The point contact cannot take place in Comsol as the radii cannot reach $l/2$ along l. However, at $\geq \omega$ (Figure 4.18), the radii $r(t)$ can reach $l/2$ without being affected by the artificial deceleration. Based on this the stop condition Equation 4.4 was implemented.

$$\text{if} \quad r(t) \geq l/2: \quad R_\mathrm{W} \text{ in pore } = 0 \tag{4.4}$$

The simplification that R_W is not significantly different along l, and both $r(t)$ may be justified by the fact that T is equal and p_i nearly equal at these positions. Based on the varying fiber positions, ω ranged from 9.5 to 11.1 degree calculated by Equation 4.5.

$$\omega = \arccos\left(\frac{\frac{l}{2} - \frac{d_{decel.start}}{2}}{\frac{l}{2}}\right) = \arccos\left(1 - \frac{d_{decel.start}}{l}\right) \tag{4.5}$$

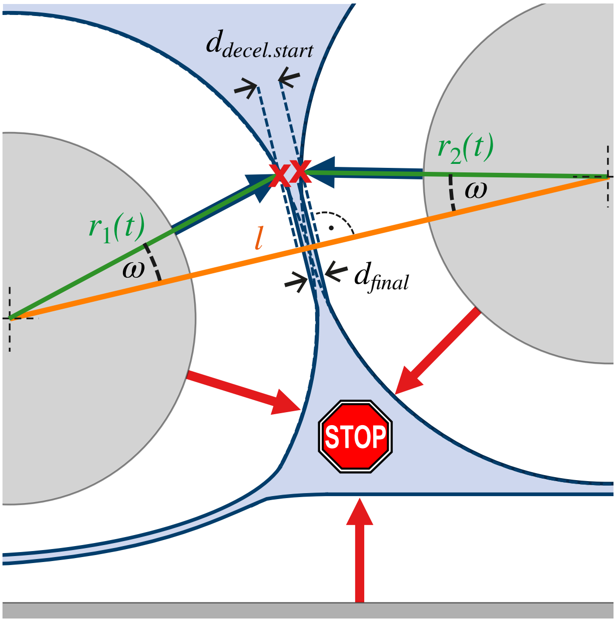

Figure 4.18: Illustration of the workaround for the surface-to-surface contact problem in Comsol. $d_{decel.start}$ is the distance between the transiently simulated CVD surfaces, at which the surfaces start to decelerate from R_{W} towards zero (compare to Figure 4.17). l is the connecting line between the fiber centers. $r(t)$ is the fiber radius plus the transient coating thickness at an angle ω towards l so that the point at the surface ($\times$) is as close as possible to the pseudocontact point, while still being unaffected by the deceleration of R_{W}. For better visibility, ω and the final gap size are roughly doubled in this sketch.

4.3.1.3 Knudsen diffusion

If a gas diffuses between walls, which have a distance in the order of magnitude of the free mean path of the gas molecules, the ordinary diffusion is slowed down by collisions with the wall [109]. This effect can be taken into account by using Equation 4.6.

$$D_{eff,i} = \left(\frac{1}{D_{mix,i}} + \frac{1}{D_{Kn,i}} \right)^{-1} \tag{4.6}$$

with $D_{mix,i}$ from Equation 3.4 and $D_{Kn,i}$ from Equation 4.7.

$$D_{Kn,i} = \frac{d}{3} \cdot \left(\frac{8RT}{\pi M} \right)^{\frac{1}{2}} \tag{4.7}$$

with d = diameter of the pore [109].

In the Single Pore Model the gap between the fibers shrinks during the CVD process, thus Knudsen diffusion becomes relevant. To calculate the Knudsen diffusion coefficient $D_{Kn,i}$ for Equation 4.7, the wall distances are needed. The minimum gap size of two adjacent parallel fibers, with an arbitrary y displacement and which change in radius, can be calculated relatively easily. However, since the fibers are not two parallel walls, this minimum gap size should not be applied on all gas molecules in the model setup. Slightly further out or further in the gap widens again. Therefore, the field variable L_{char} (Equation 4.3), which was defined in the previous section, is taken for d in Equation 4.7. This changes $D_{Kn,i}$ into a time depending and spatial quantity.

By using L_{char} the side boundaries above fiber #1 and #3 are treated as walls as needed for the deforming mesh interface. In reality, they do not exist and thus do not influence diffusion. However, this inaccuracy has only a minor influence. The effective diffusion coefficients ($D_{eff,i}$, Equation 4.6) are lowered by only 1–4 % (depending on the species) near the side walls. This small influence is further decreased by the low consumption at this position and thus low concentration gradients. Thus, using L_{char} also as d for the Knudsen diffusion has no physically meaningful influence on the pore structure results. Nevertheless it saves a lot of computational effort.

4.3.1.4 Mesh and solver configuration

For the Single Pore Model a free triangular mesh was chosen. Since the geometry changes drastically over time, the configuration of the automated meshing algorithm in Comsol has to be done very carefully to ensure working meshes for all time steps. With the automatic standard settings convergence cannot be achieved. The time-dependent solver was set to remesh the geometry of the time step after which an element distortion would have reached a value of 1.1. As consistent initialization option "Backward Euler" was selected. The maximum simulated time step size was limited to 5 seconds. The low limits in distortion and step size improve the robustness of the model.

The settings for the automated initial meshing and remeshing are listed in Table 4.3. The general settings are applied on the complete model geometry. Here the maximum element size and element growth rate are chosen rather coarse for faster calculations. At the W surface these settings have to be overwritten by finer mesh settings.

Table 4.3: Comsol mesh settings to meet the challenges of the transient Single pore infiltration model.

	general	W surface	first contact
max element size [µm]	20	10	
min element size [µm]	0.8		
max element growth rate [-]	1.2	1.1	
curvature factor [-]	0.3	0.12	
resolution of narrow regions [-]	1		3

Firstly, the elements along the entire W surface were limited in their maximum size and growth, which also reduces the size of the elements that represent the near surface gas. This is necessary to model near surface steep gradients in p_i and wall distances in sufficiently high resolution. Secondly, around the pseudocontact and in the area of the moving entrance of the pseudogap, quantities such as the wall distances, the diffusion coefficient, and the wall velocity (equal to R_{W}) change spatially rapidly. Therefore, despite of the smoothed deceleration of R_{W}, a very high mesh resolution is still necessary to avoid the simulation crashing due to discontinuities. To further increase the mesh resolution only where needed, the curvature factor at the W surface is decreased significantly. A lower curvature factor causes more elements to be used to approximate the true shape of a curve. As the curvature of the W surface is particularly high at the entrance of the pseudogap, a high mesh resolution is created automatically only where needed. Thirdly, a high mesh resolution is already required for the first contact of two opposing and moving surfaces. In this case, however, the lower curvature factor does not solve the problem as there are no sharp radii before a surface-to-surface contact. This is solved by increasing the resolution of narrow regions from 1 to 3 at the auxiliary lines, which connects the surface points at which the first contacts will take place (two lines for fiber to fiber and two more for fiber to ground, visible in Figure 4.14b). These settings lead to robust and computation time optimized meshes for the present model as shown in Figure 4.19.

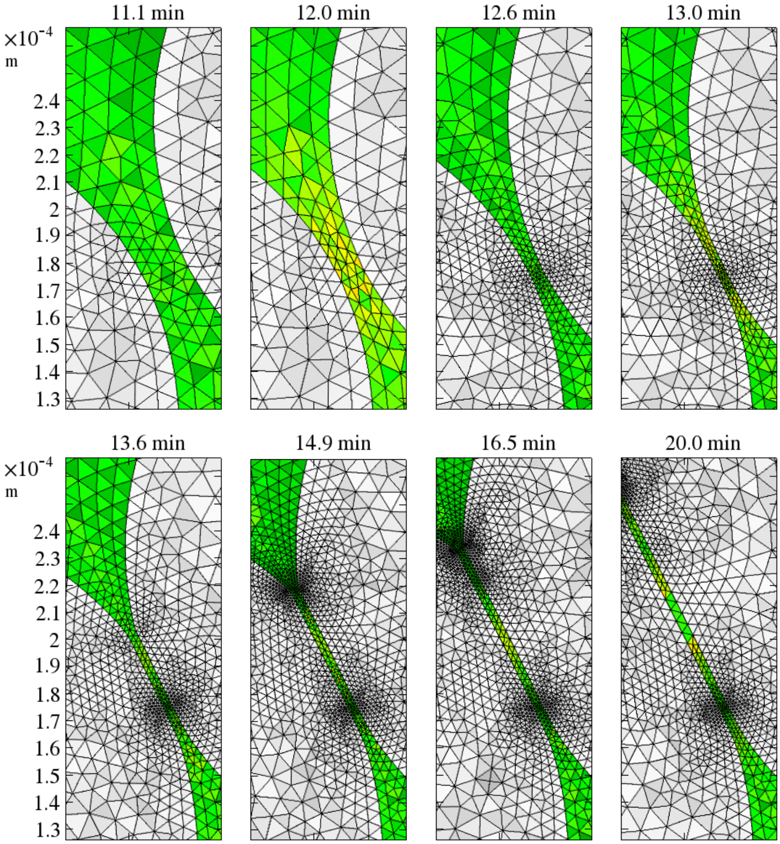

Figure 4.19: Mesh evolution during a CVD-W pseudocontact. The filling color of the elements illustrates the element skewness, which is a measure for the element quality. The color bars (from bad to perfect quality) run from black to white for solid W, and from red to dark green for the gas. As it can be seen, the element quality remains very good.

From 11.1 to 12.0 min, the mesh movement can still be covered by mesh deformation, since it only slightly reduces the element quality between the fibers. At 12.6 min, the element deformation would be too high. Therefore, a remeshing is done resulting in a finer mesh without mesh deformation around the contact point due to the adjustment of the resolution of narrow regions. Between 13.0 and 13.6 min the pore is sealed, the lower part no longer moves. The upper part continues to grow, while the fine mesh area moves upwards. The remeshing settings allow also for a recovery to a coarser mesh, where a fine mesh is no longer required. For example at 20.0 min the pseudogap width is resolved by only one element, if it is far enough away from sharp radii, which saves computational time.

4.3.1.5 Calculation of the simulated relative density

The simulated relative density ($\rho_{rel,sim}$) was calculated similar to Equation 4.2 used for the experimental relative density. Only the simulated pore area ($A_{pore,sim}$) is acquired differently. Instead of counting the pixels, it is calculated via a Comsol-internal area integration of the step function f_{step} (Figure 4.17) within the pore area, which is the gas domain below the fibers after the pore got sealed (Figure 4.20b). The pore area (A'_{pore}) still includes the pseudo gap, due to the reasons explained in Section 4.3.1.2. By modifying the argument of f_{step} from $(L_{char})^{-1}$ (Figure 4.20c) to $(L_{char} - d_{final}/2)^{-1}$ (Figure 4.20d), the pseudo gap does not add up to the integration of the pore area (Equation 4.8), since the gas within the pseudo gap is always zero. Therefore, it is treated as being completely filled with solid W for the relative density calculation, which is more correct. This can become especially useful for more complex calculations (e.g. 3D ones), in which the final pseudo gap size d_{final} has to be increased to reduce the needed amount of elements and thus to achieve bearable computational times.

$$A_{pore,sim} = \oiint_{0}^{A'_{pore}} f_{step}\left((L_{char} - d_{final}/2)^{-1}\right) dA \tag{4.8}$$

with $A_{pore,sim}$: (corrected) simulated pore area [m^2]
A'_{pore} : pore area including the pseudo gap [m^2]
f_{step} : step function (Figure 4.17) with $(L_{char} - d_{final}/2)^{-1}$ as argument [-]

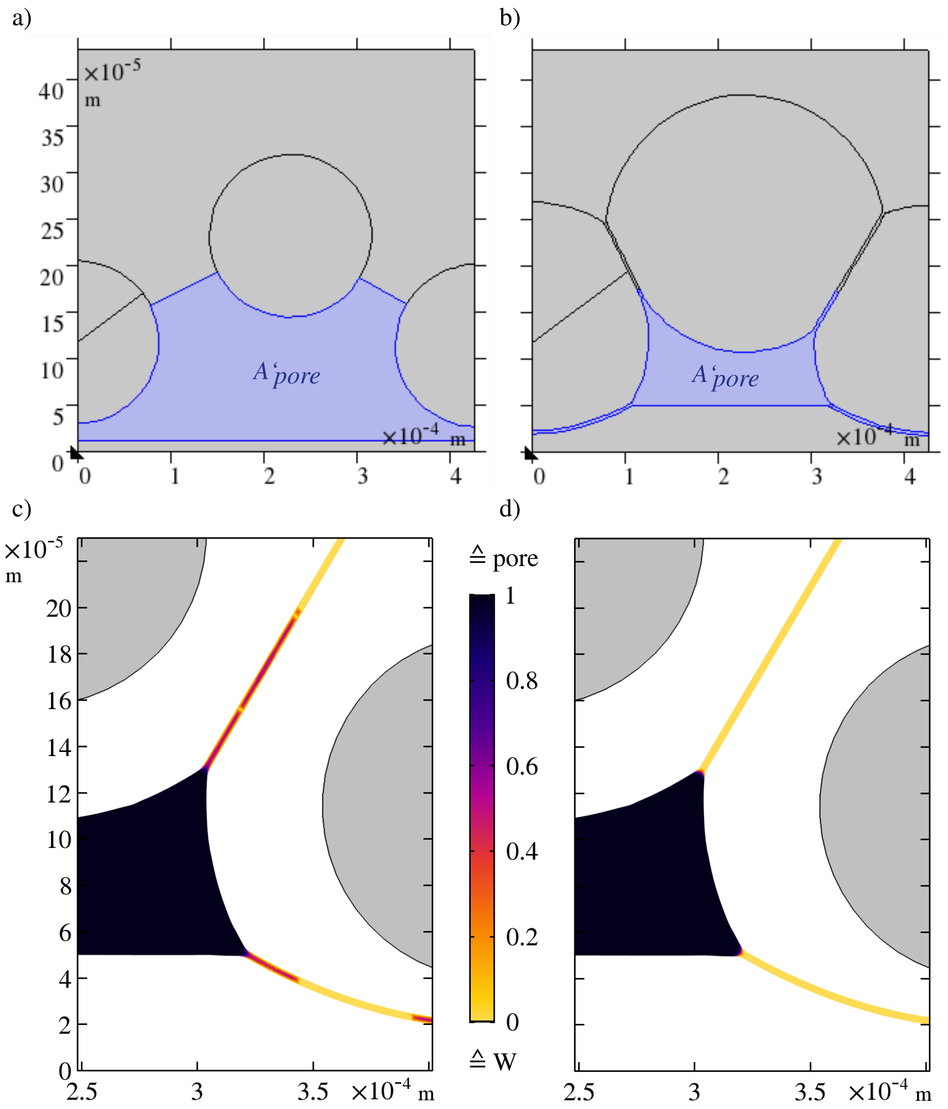

Figure 4.20: During the model setup, the A'_{pore} domain has to be selected for $t = 0$ (a). $\rho_{rel,sim}$ increases transiently during the simulation and stays constant after the pore got sealed (b). Color maps are plotted within A'_{pore} for c) $f_{step}\left((L_{char})^{-1}\right)$ and d) $f_{step}\left((L_{char} - d_{final}/2)^{-1}\right)$, whereby for the pore area integration, black is counted as 1 and orange as 0 (solid).

4.3.2 Results

In Figure 4.21 an example for the transient W-CVD growth is shown.

For t = 0 to 8 min: As the pore entrance becomes narrower, p_{WF_6} decreases within the pore and the diffusive flux increases due to larger concentration gradient.

At t = 10 min the right entrance is sealed, whereby the technically necessary pseudo gap remains. The diffusion speed within the pseudo gap is strongly reduced due to the implementation of Knudsen diffusion. This causes the diffusive flux to switch direction in the upper right part of the pore, as it would happen in reality as well.

At t = 12 min the pore is almost sealed. The diffusive flux through the remaining real gap is maximal and p_{WF_6} within the pore is near zero.

At t = 13 min the pore is sealed and R_{W} as well as the consumption of WF_6 within the pore is set to zero. Therefore, the pore is quickly filled with WF_6 again, due to diffusion through the gap, which would not happen in reality. In reality p_{WF_6} would stay zero (blue) within the pore for $t \geq 13$ min. However, there is no influence by this effect on R_{W} since R_{W} is already zero within the pore and outside of the pore WF_6 is abundant. Similar as above, all 45 pore shapes were simulated in two sets of parameter sweeps (all in one could not be handled by the RAM). With the fiber positions as simulation input, the Φ_{V_f} values are identical to the experimental results (Table 4.2). The corresponding simulated ρ_{rel} were calculated as described in Section 4.3.1.5. The averaged value resulted in 76.1 ± 8.1 %. The values for each pore are listed in the Appendix (Table 9.4) and plotted in the following comparison to the experimental results.

4.4 Experimental vs. simulated results

In Figure 4.22 an example for the graphical comparison between the experimental and simulated W_f/W pore structure is shown (fabric #1, first layer, pores #29-35). As it can be seen, the match is excellent. The pore structure looks almost identical. Furthermore, the coating thickness on top of the fibers in the first layer matches very well between experiment and simulation, if one considers that only for the experimental results the thickness of the second fabric layer coating is added (red arrows in Figure 4.22c).

As the graphical comparison is not very precise and seven pores are eventually not representative, Figure 4.23 shows the direct comparison of ρ_{rel} around all 45 pores. $\rho_{rel,exp}$ and $\rho_{rel,sim}$ were obtained as described in Section 4.1.3 and Section 4.3.1.5, respectively.

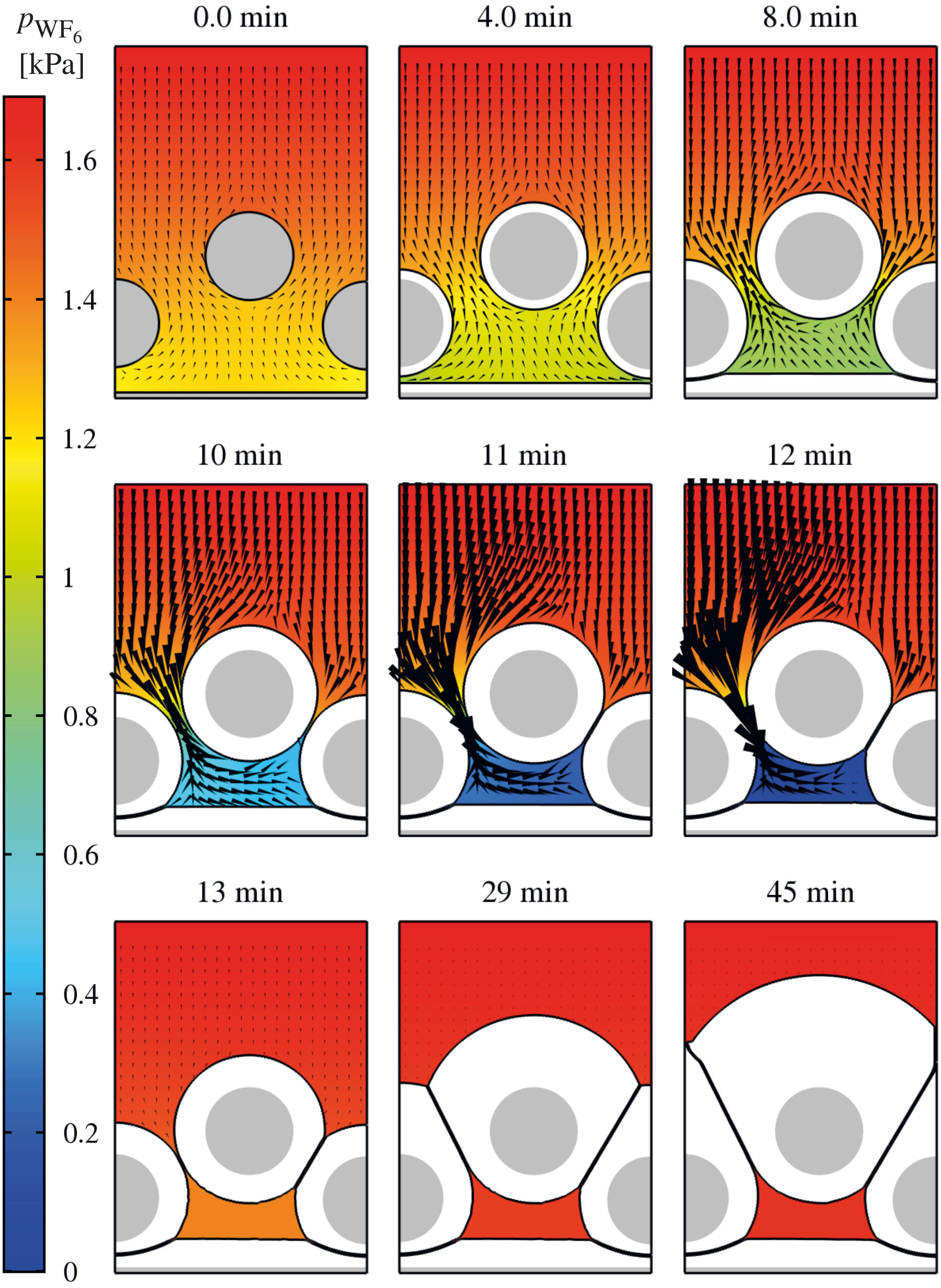

Figure 4.21: Frame series for the Single Pore Model (pore #0). Grey domains: substrate (fibers and ground), white domains: growing CVD-W, colored domains: gas, showing p_{WF_6} with black arrows for the total diffusive flux of WF_6.

a) experimental

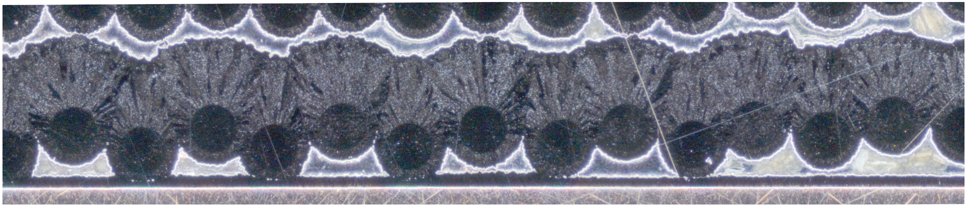

b) simulated

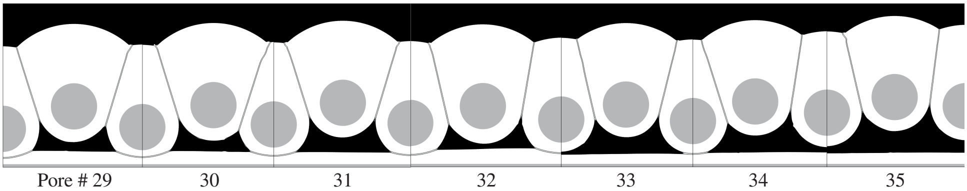

c) overlayed

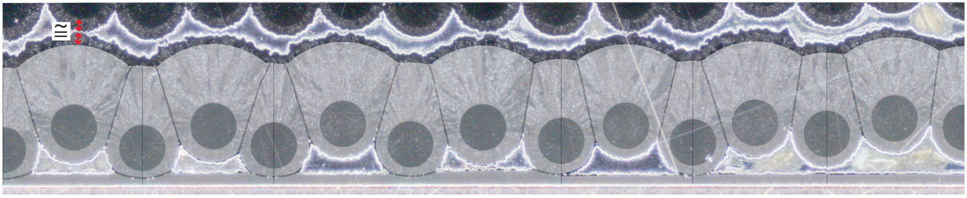

Figure 4.22: Pore structure result comparison example. a) section of the dark field microscopic image of the experimental result, b) concatenation of the seven single pore simulation results c) direct comparison via overlaying.

During experiment, six pores were filled a bit further even after both upper pore entrances were already sealed. Regarding these pores at least one of the lower side fibers was positioned so high that the educts could still defuse sidewards through the gap between the lower fiber and the ground. These pores should not be compared to the simulated results as for each simulation only one pore without neighbors was modeled. Therefore, Algorithm 4.1 (page 80) was written to detect these pores based on the fiber positioning. The corresponding ρ_{rel} data points (×) were excluded from the linear fit in Figure 4.23. An example for an excluded pore is #33 in Figure 4.22. Here the CVD-W connects the left fiber with the ground in the experiment, but not in the simulation, for the reason described above.

Figure 4.23a includes the simulated results for a uniform growth, which can be easily obtained by just deactivating the interface transport of concentrated species (tcs) in Comsol. This causes the species concentrations to remain at their initial values and thus R_{W} to remain constant over the entire geometry. In Figure 4.23a this simplification results in an linear fitting slope of 1.15, since the simulated pore filling is

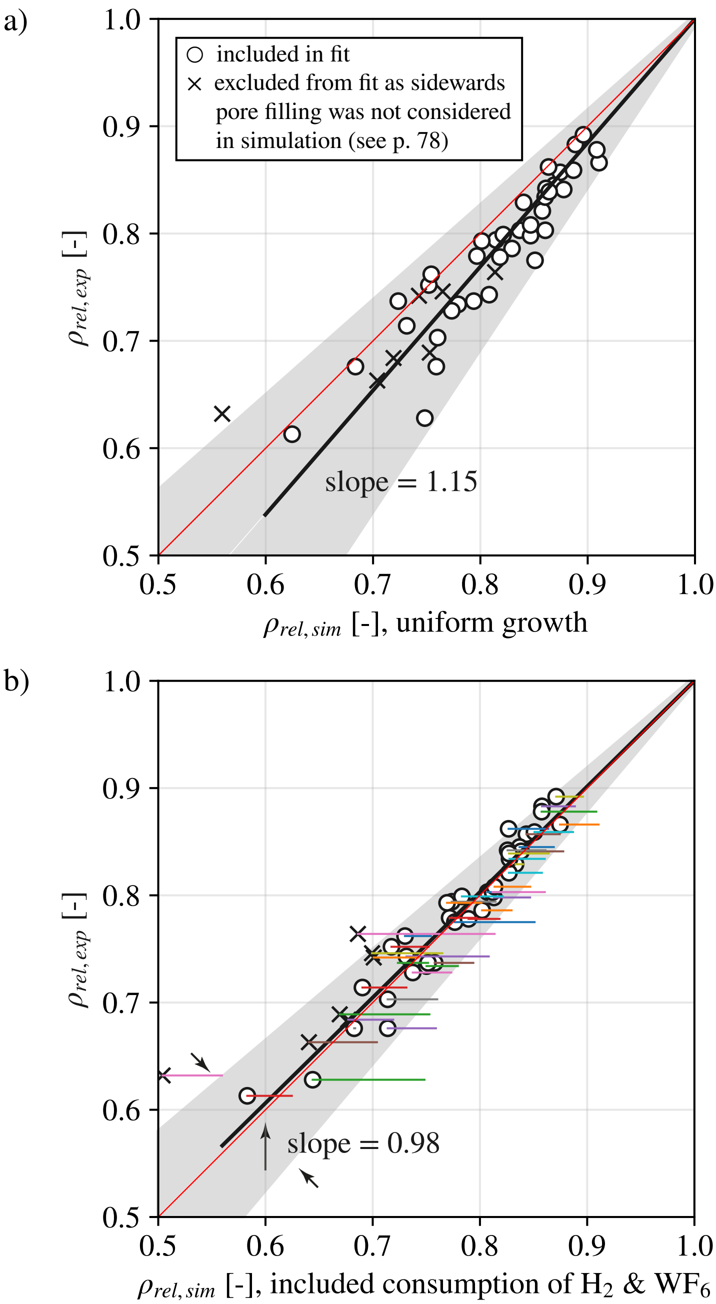

Figure 4.23: $\rho_{rel,exp}$ vs. $\rho_{rel,sim}$ for a) uniform simulated growth and b) nonuniform simulated growth. The latter considers the higher consumption of the educts while going deeper into the pore. The colored lines mark the shift of $\rho_{rel,sim}$ from a) to b).

overestimated without considering the gas consumption. On the other hand, by including the consumption and Knudsen diffusion, the fitting slope is with 0.98 very close to a perfect match (=1.0) and additionally the scattering of the data points is reduced significantly (Figure 4.23b).

To conclude, the validation of the model for the pore infiltration is very successful. As next step, this model can be used for a CVD process parameter study, which will be presented in the next chapter.

Algorithm 4.1: Pore# filter

Input: pore# (i), and fiber positions

Result: list of pore#s, which still got experimentally filled sideways through the gap between the ground and a side fiber, after the top got sealed already

```
Result:
foreach $i$ in [1, 2, ..., 45 - 1] do
    if $d_{ff,max}(i-1) > d_{ff,max}(i)$ or $d_{ff,max}(i+1) > d_{ff,max}(i)$ then
        if $d_{fg,max}(i) > d_{ff,max}(i)$ then
            add i to Result
        end
    end
end
```

with $d_{ff,max}$: maximum of the surface to surface distances between the left and middle fiber, and the middle and right fiber [m]

$d_{fg,max}$: maximum of the surface to surface distances between the left fiber and the ground, and the right fiber and the ground [m].

---

5 Parameter studies towards relative density and fiber volume fraction

This chapter covers the parameter study for a single pore. It is divided in two main parts with different input parameter variations. The first one focuses on the physical CVD parameters (T, p_i) and the second one on the geometry parameters of the fabric. The fiber geometric setup from the model validation was simplified by introducing a vertical symmetry axis through the former middle upper fiber (#2). For the CVD parameter study, the fiber positions were kept constant, so that Φ_{V_f} stayed constant, leaving the influence on ρ_{rel} as output. For the fiber position study, the CVD parameters were kept constant and ρ_{rel} as well as Φ_{V_f} were investigated as output.

5.1 Physical CVD parameter variation

For the physical CVD parameter variation, the constant fiber positions were chosen rather disadvantageous for ρ_{rel} by placing the fibers close together, as shown in Figure 5.1a. This was done to see larger differences in the results due to the resulting larger consumption rates. Further, instead of performing a time-consuming transient simulation for each parameter set, quick stationary simulations were done. This procedure can be justified by the fact that the CVD parameters, which lead to a most uniform infiltration, will also lead to the highest possible ρ_{rel}. Thus, the quotient of R_{W} deep inside of the pore ($R_{\mathrm{W},2}$) and at the pore entrance ($R_{\mathrm{W},1}$) is investigated as output (y). The geometry and locations of $R_{\mathrm{W},i}$ can be seen in Figure 5.1a. The study concept is summarized in Figure 5.1b. In order investigate also transient effects, caused by e.g. the shrinking pore entrance size, three different fiber radii and ground heights were taken as geometries for the stationary simulations. These geometries are shown as different colors in Figure 5.1c and can be seen as pseudo time steps as the geometry would change from black to green to blue similarly in a transient simulation with the CVD-W growing.

The results for the variations in $p^{top}_{\mathrm{WF}_6}$, $p^{top}_{\mathrm{H}_2}$, and T are shown in Figure 5.2 together with the starting geometry as series (black, green, blue). The key outcome is that the most uniform W deposition (y values nearest 1), and thus the best pore infiltration, can be achieved by low T, low $p^{top}_{\mathrm{WF}_6}$, and low $p^{top}_{\mathrm{H}_2}$, as long as the W deposition is not depending on p_{WF_6}. The reasons will be explained in detail in the following.

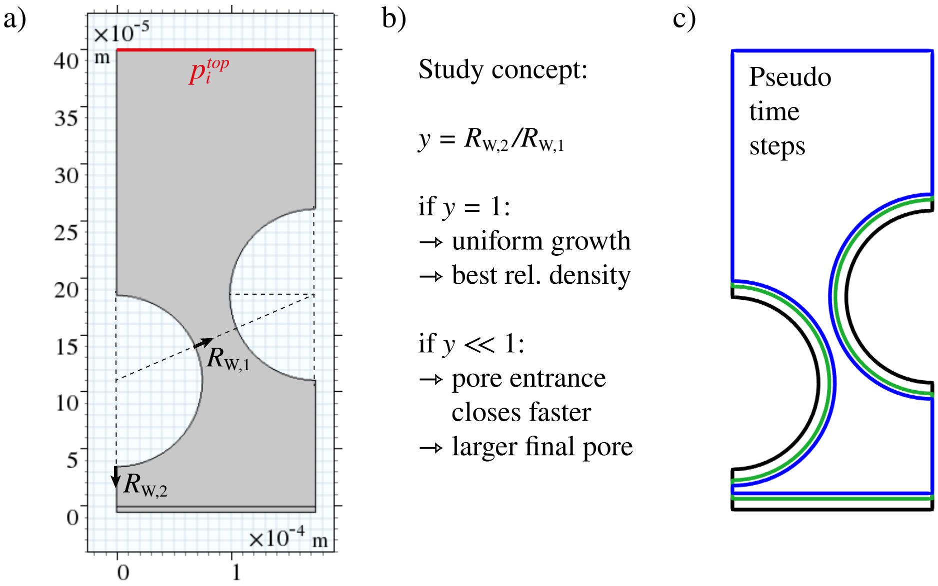

Figure 5.1: Setup and concept for the parameter study regarding the infiltration of a single symmetric pore adjacent to two W fibers. a) Model geometry showing the positions of $R_{W,1}$ and $R_{W,2}$, needed for the y-axis in Figure 5.2. b) Study concept. c) Visualization of three different geometries (pseudo time steps) of the stationary W infiltration simulation resulting in (shrinking) pore entrance sizes of 39.8, 20.9, and 11.4 µm.

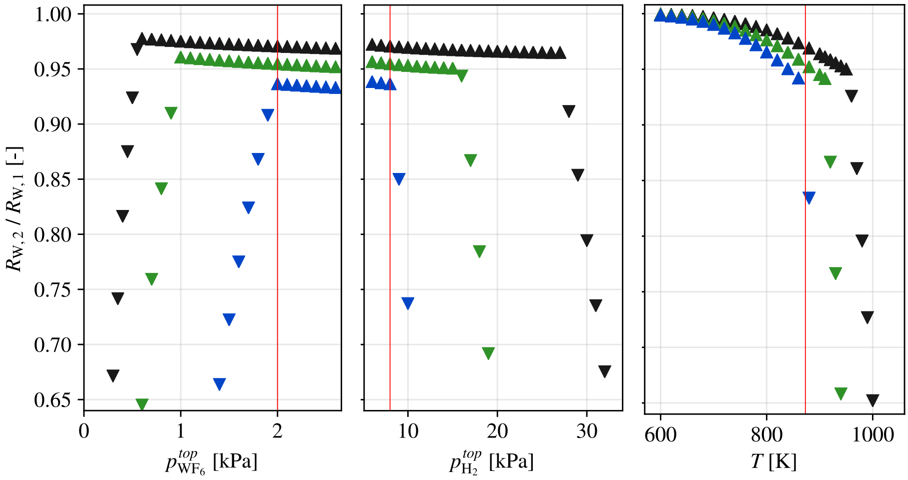

Figure 5.2: Parameter study results: $R_{W,2}$ / $R_{W,1}$ versus $p_{WF_6}^{top}$, $p_{H_2}^{top}$ and T, with △: $R_{W,2}$ independent of p_{WF_6} (Section 3.4, Zone III) and ▽: $R_{W,2}$ being dependent on p_{WF_6} (Section 3.4, Zone II). The constant parameters, if not varied, were $T = 873\,\mathrm{K}$, $p_{WF_6}^{top} = 2\,\mathrm{kPa}$, $p_{H_2}^{top} = 8\,\mathrm{kPa}$, marked as red lines, and $p_{HF}^{inlet} = 2\,\mathrm{kPa}$. The series correspond color-wise to the different geometries as shown in Figure 5.1c, representing the pseudo time steps.

$p_{\mathrm{WF_6}}^{top}$ variation

The diffusion coefficient is reciprocal to the pressure (Equation 3.4). A lower gas pressure results in less collisions and faster diffusion and thus in smaller species concentration gradients and hence in a more uniform W deposition within the pore. $\mathrm{WF_6}$ is the largest molecule in the mixture, so its partial pressure has the biggest impact with respect to the just described phenomena. However, this trend is overridden as soon as $\mathrm{WF_6}$ starts to deplete at the bottom of the left fiber, which leads to an immediate and significant decrease in infiltration uniformity. Therefore, there is a sweet spot for $p_{\mathrm{WF_6}}$ right before this happens. However, a safety margin should be considered as well.

$p_{\mathrm{H_2}}^{top}$ variation

For low $p_{\mathrm{H_2}}$, where R_{W} is independent of $p_{\mathrm{WF_6}}$, two effects overlay. The first is again that a lower pressure enhances diffusion. As $\mathrm{H_2}$ molecules are small, this effect is less pronounced compared to the variation of $p_{\mathrm{WF_6}}$. Secondly, R_{W} is proportional to the square root of $p_{\mathrm{H_2}}$ (Equation 3.10b). Therefore, with lower $p_{\mathrm{H_2}}$, R_{W} decreases and thus the $\mathrm{H_2}$ consumption is lowered, leading again to smaller concentration gradients and thus more uniform infiltration. For very high $p_{\mathrm{H_2}}$, $R_{\mathrm{W,1}}$ becomes so large that $\mathrm{WF_6}$ starts to become the limiting factor for $R_{\mathrm{W,2}}$ at the bottom of the pore. This leads again to an extreme drop in uniformity. Thus, the sweet spot for the infiltration is a low $p_{\mathrm{H_2}}$ whereby it should be kept $\geq 3 \cdot p_{\mathrm{WF_6}}$ to match the reaction stoichiometry (Equation 2.2) and to avoid F covering the reaction surface and thus hindering the adsorption and dissociation of $\mathrm{H_2}$ as explained in Section 3.4 (Zone IV). Finally, it should be pointed out that the impact of $p_{\mathrm{H_2}}$ on the uniformity within the high-uniformity regime is one order of magnitude smaller than the impact of $p_{\mathrm{WF_6}}$, as it can be seen by comparing the x-axis scales. This will become important later for deciding the overall best process parameters under consideration of also other effects such as the grain fineness.

T variation

With lower T the pore infiltration becomes more uniform. Although higher T also increases the diffusion speed, this is strongly counteracted by the exponential increase of R_{W} and thus of the educt consumption. By decreasing T to values at around 673 K, and lower, it seems that even with this rather unfavorable fiber positioning, practically perfect uniformity can be achieved. This is a good and important result.

However, by lowering T, also the deposition duration increases exponentially. Therefore, T values at around 773 K are more reasonable for the production of W_f/W.

Transient effects and the influence of the Knudsen diffusion

As the CVD-W grows (black → green → blue, Figure 5.1c), the infiltration uniformity worsens (blue < green < black, y-axis in Figure 5.2a–c). On the one hand, this is caused by the reaction surface within the pore becoming larger and thus the consumption becoming higher. On the other hand, the educt supply is slowed down as the pore entrance becomes smaller. The reason for this is that collisions of the gas molecules with a wall become more frequent, slowing down the diffusion speed, which was implemented into the model via Knudsen diffusion.

As a side study, the effect of the Knudsen diffusion was quantified to see if it has a significant influence. In Figure 5.3, the numbers in the color maps are reciprocal to the influence of the Knudsen diffusion on the (overall) effective diffusion speed, whereby a value of 1 would results in Knudsen diffusion having no influence. The numbers result from $D_{eff,i}/D_{mix,i}$, with $D_{eff,i}$ being the effective diffusion coefficient with implemented Knudsen diffusion (Equation 4.6), and with $D_{mix,i}$ being the mixture averaged diffusion coefficient (Equation 3.4) without Knudsen diffusion. Beside the wall distance, different input parameters for the gas molecules and $p_{\mathrm{WF_6}}$ are compared.

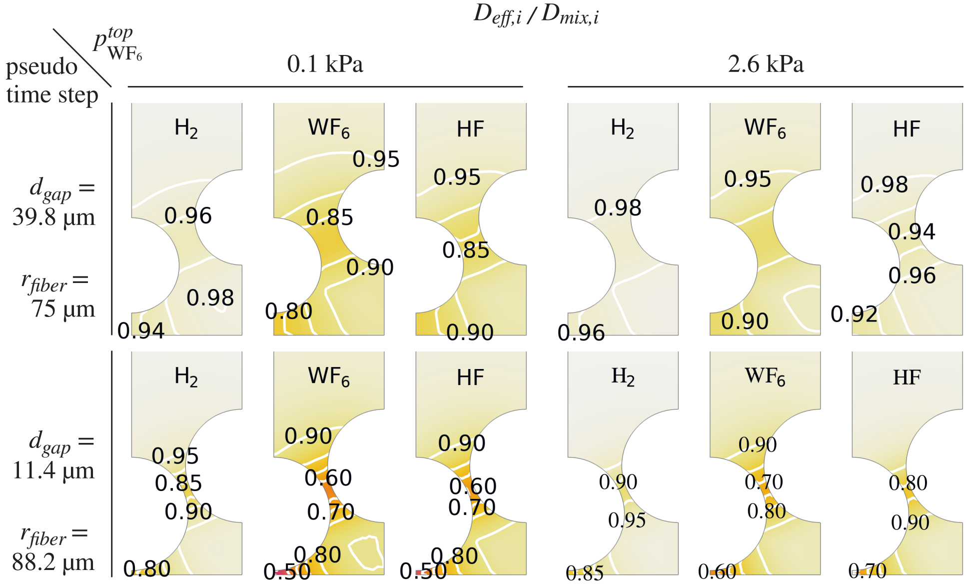

Figure 5.3: Influence of the surface-to-surface distance on the factor $D_{eff,i}/D_{mix,i}$ (Equation 4.6 divided by Equation 3.4). The columns feature different $p^{top}_{\mathrm{WF_6}}$ and the rows feature the first and last pseudo time step from Figure 5.1c. The other parameters are, again, T = 873 K, $p^{top}_{\mathrm{H_2}}$ = 8 kPa, and p^{top}_{HF} = 2 kPa.

As result, smaller numbers can be seen where the walls are more narrow (within each plot and especially for the subplot *row*-comparison), and for lower $p^{top}_{\mathrm{WF_6}}$ (subplot *column*-comparison). Furthermore, the numbers are reciprocal to the molecule size (H_2 < HF < WF_6).

The Knudsen diffusion is important for the simulation at low pressures or at small gap sizes. In the shown setup the Knudsen diffusion reduced the diffusion speed by up to factor 2 (0.5 values in the lower left). To conclude this side study, Knudsen diffusion should indeed be implemented for modeling W_f/W synthesis, especially as the pore entrance size always becomes small during a transient simulation with pore closure.

5.2 Fabric geometry parameter variation

In Section 5.1 was shown that for certain process parameters the W_f/W pores can be filled nearly uniformly (<1% R_W deviation for 740 K, $p_{WF_6} = p_{HF} = 2$ kPa, $p_{H_2} = 8$ kPa, despite of narrow fibers). Therefore, the fiber position study for the symmetric pore infiltration was done by writing a very fast solving Python script (few seconds for all parameters), which calculates ρ_{rel} vs. Φ_{V_f} based on the simplifications of uniform growth, parallel warp fibers, neglect of the weft fiber, and which is thus based on simple geometry. The script (Section 9.5, [108]) is capable of showing the trends and a good estimation of the ρ_{rel} and Φ_{V_f} value combinations for all kind of warp fiber positions. The results are presented in Figure 5.5.

As stated earlier, the goal is to maximize ρ_{rel}. Regarding Φ_{V_f}, there is theoretically an optimal upper limit with respect to the fiber-reinforcing mechanisms with a yet unknown value. However, this value can most likely not be reached with the current layerwise W_f/W production procedure. Thus, the goal is also to to maximize Φ_{V_f}.

For an easier understanding of the following it is recommended to memorize the parameters in Figure 5.5a.

If the roll (Figure 5.4) achieves perfect flattening of the fabric, the vertical fiber displacement (Y'_{ff}) oscillates along the warp fiber axis between $\pm D_{weft}$ (= weft fiber diameter, here = 50 µm). For $Y'_{ff} = 0$, the vertical distance (Y_{fg}) between the lower fiber [illegible] wo[illegible] become [illegible]ximal wit[illegible] $D_{weft}/2 = 25$ µm. This value is [illegible] Figure 5[illegible] With th[illegible]ot, the ne[illegible]d horizontal fiber surface [illegible] timated to achieve certain Φ_{V_f} and ρ_{rel} value combinations. For [illegible] 105 µm, Φ_{V_f} and ρ_{rel} result in 0.35 and 0.90, respectively (b,

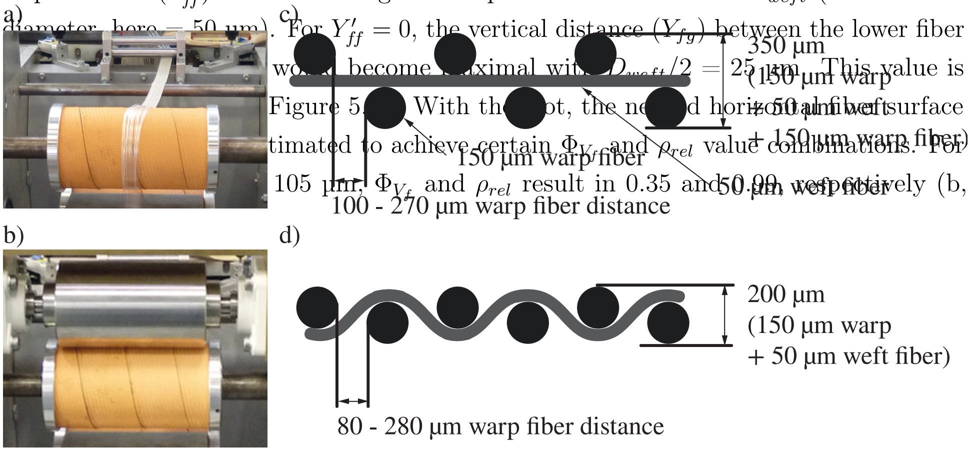

Figure 5.4: Roll to flatten the W fabric [54] (shown again).

orange marking). As another example, with a $X_{ff} = 150$ µm, Φ_{V_f} and ρ_{rel} result in 0.30 and 0.999, respectively (b, violet marking).

The other extreme for the warp fiber position is where it contacts with the weft fiber, as in Figure 5.4. Here, Y'_{ff} equals $D_{weft} = 50$ µm, and Y_{fg} becomes ideally zero. This case is plotted in Figure 5.5c. In comparison to the first case (b), Φ_{V_f} remains the same and ρ_{rel} increases hardly by 0.0013 for $X_{ff} = 105$ µm, and by 0.0002 for $X_{ff} = 150$ µm.

It should be noted that at this position, in reality, the weft fiber would increase Φ_{V_f} (for this cross section as well as for a complete 3D W_f/W structure) and it would seal the pore for this 2D cross section, right from the start, whereby in 3D this pore can still be infiltrated via bypassing the weft fiber. To which degree the pore would be infiltrated, can be considered only in a 3D simulation. However, the quick and simple Python script results presented still clarify trends regarding Φ_{V_f} and ρ_{rel} as function of the fiber positioning, which are valid with and without simplifications.

As it can be seen in Figure 5.5b,c, it should be always aimed for reducing Y_{fg} and $Y^{'}_{ff}$ as much as possible, which will increase Φ_{V_f} and ρ_{rel} simultaneously. To have throughout the entire sample low Y_{fg}, the fabric should be as even and flat as possible and placed under tension directly on the heating plate. As simple as this sounds, very large Y_{fg} can be locally caused by deformation due to suboptimal storage (e.g. by coiling with a too small radius). An uneven or not well placed fabric results easily in W_f/W with extremely large pores leading to weaker mechanical and thermal properties.

X_{ff} behaves proportional to ρ_{rel} (until $\rho_{rel} = 1$) and reciprocal to Φ_{V_f}. Here, a compromise has to be made, whereas a ρ_{rel} near one has priority. By placing additional fabric layers onto this first layer, the absolute values for Φ_{V_f} and ρ_{rel} of the complete W_f/W composite would change, but the discussed trends will still remain valid.

It should be noted that in reality the stiffness of the warp and weft fibers has an additional influence. After rolling the fabric, remaining tensions can straighten the fibers again. This increases the resulting $Y^{'}_{ff}$ and happens if X_{ff} is below a certain value which depends on the diameter and the elastic and plastic deformation properties of the fibers. For example, fabric 1 had the smallest X_{ff} (71 µm). Its $Y^{'}_{ff}$ resulted at the investigated cross section in 82 µm. At the cross section where the warp and weft fiber touch each other, $Y^{'}_{ff}$ has to be even higher. This is significantly larger than the maximum value of 50 µm discussed for a perfect flattened fabric.

The here presented parameter study results have been applied to improve W_f/W as it will be described in Chapter 7. However, to choose the best CVD process parameters, there is yet another factor which should be considered: The influence on the CVD-W grain morphology, which is presented in the following chapter.

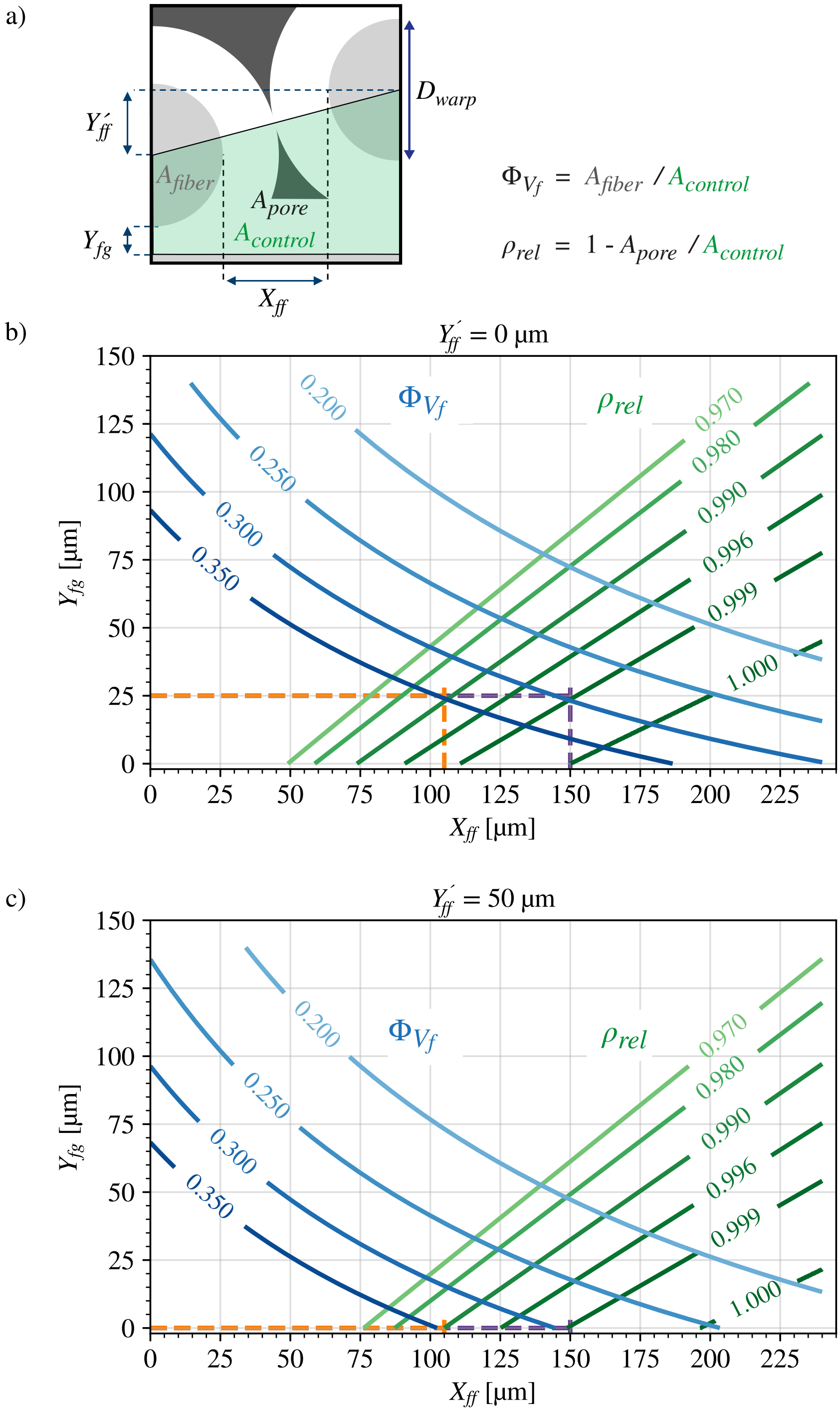

Figure 5.5: Contour plots for Φ_{V_f} and ρ_{rel} (b, c) as function of the warp fiber position parameters as shown in (a) with $D_{warp,fiber} = 150\,\mu\text{m}$.

6 Grain morphology of the CVD-W

6.1 Influence of the grain size on the mechanical properties

The microstructure of a material, especially the grain size, strongly influences its mechanical properties. The strength of a polycrystalline metal can be increased by grain size refinement since finer grains lead to more grain boundaries hindering dislocation sliding within the crystal lattice [110]. This effect can be quantized by the Hall-Petch relation [111,112]. Also for W [113–115] and CVD-W [116] it is reported that the strength increases for finer grains.

Bellow the DBTT (Section 2.2), normal W with randomly orientated coarse grains, breaks completely brittle under tension and mostly in an inter-granular fracture mode [14]. However, it is still possible to obtain large ductility under certain conditions. By severe mechanical deformation that lowered the average grain size from ∼40 µm to ∼0.5 µm, the maximum strain for uniaxial compression was improved to up to 60% [113, 114]. The high ductility is probably also enhanced by a large portion due to the deformation induced more favorable texture, activating slip systems and increasing the dislocation mobility [117].

For CVD-W with very fine randomly orientated grains of also ∼0.5 µm, the maximum compression strain was reported to be 4% [116], which is still high for an intrinsic brittle refractory and could be enabled by grain boundary sliding. For CVD-W with columnar grains (and thus strongly textured), maximum strains were reported to be even up to 85% for uniaxial compression in CVD grow direction [116], whereby it should be noted that many of the grains detached from each other. However, the latter testing conditions are not relevant for the fusion application, where thermal expansion does not lead to uniaxial stress states. Furthermore, using columnar CVD-W grown on a plane substrate as plasma facing component would bear the risk of cracks running intergranularly through the entire coating. This can be avoided by using a fabric as substrate so that the columnar grains originating from the fiber surfaces point radially in all directions, as it can be seen in Figure 6.1. For the resulting anisotropic grain structure, grain fining is probably only favorable for the ductility in the submicrometer range, where grain boundary sliding can take place. In the micrometer range there is probably only little influence on the ductility; but in W_f/W the (pseudo) ductility is achieved by the fiber reinforcement anyways.

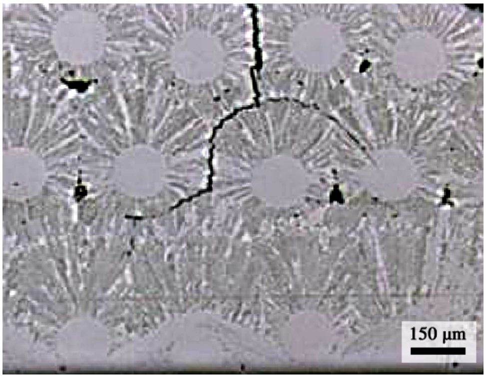

Figure 6.1: Additional motivation for finer CVD-W grains: To reduce probability for cracks at the CVD-W surface-to-surface contact areas.

There is theoretically another benefit for W_f/W if the CVD-W grains become finer. As the CVD-W matrix surfaces grow between adjacent fibers until contact, micropores can remain due to the pyramid grain facets. These micropores are aligned along the 2D contact interfaces being the weakest link in the composite, which can lead to crack formation due to thermal stress during cooling down after the CVD process, as it can be seen in Figure 6.1. This could therefore happen also during thermal cycling in the fusion reactor, bypassing the fiber reinforcing mechanisms. Thus, it is important to take countermeasures. Finer grains should lead to smaller micropores and to more contacts and thus to a stronger connection of the matrix-matrix interfaces.

To conclude, the aim is to get fine W grains in the CVD matrix of W_f/W, providing a higher matrix strength and most likely a stronger matrix surface-to-surface contact integrity. This motivation leads to the question: which CVD process parameters result in the finest W grain structure? The answer will be evaluated in the following sections.

6.2 Literature review: influence of the CVD parameters on the grain size

The information from literature regarding the grain size of W as function of the CVD process parameters is not yet very extensive. Most studies focused on the influence of the coating thickness and the deposition temperature.

With respect to the coating thickness, it can be summarized that the grain size increases with increasing coating thickness [118–121]. For a columnar grain structure, the grain lengths is proportional to the coating thickness and can reach a maximum of the coating thickness. Also the surface grain width increases with increasing coating thickness. The reason is that the initial grain nuclei have a random orientation, whereas the $\langle 100 \rangle$ oriented grains grow the fastest and block off the slower growing grains [121]. The $\langle 100 \rangle$ orientation is energetically most favorable, as supported by the research on the solidification process of body-centered cubic (BCC) crystals, such as W, with molecular dynamics and phase field modeling [122, 123]. The $\langle 100 \rangle$ orientated grains can still be rotated along the axis perpendicular to the surface and thus their grain boundaries remain intact while growing next to each other.

Regarding the deposition temperature (T), it is reported that it has below the recrystallization temperature no influence on the deposited grain width [118, 124, 125]. Melliar-Smith et al. reported this for T of 873, 973, and 1073 K with grain widths at the coating surface between 50 and 100 nm and a coating thickness of 240 ±10 nm [124]. Learn et al. reported this for T of 573 and 673 K, whereby for both the grain widths increased from 40 to 200 nm due to different coating thicknesses of 50 to 500 nm [118]. And finally Chang et al. reported this qualitatively for T of 645, 763, and 883 K and film thicknesses of ca. 24 µm [125].

Regarding the effect of changes in the gas composition, Chang et al. reported qualitatively, for a set of six different WF_6 to H_2 volume flow ratios at a constant total pressure, that finer grains were obtained for lower $\dot{V}_{\mathrm{WF}_6}^{inlet}$ and for higher $\dot{V}_{\mathrm{H}_2}^{inlet}$. However, it should be noted that with the procedure used, the complementary partial pressures p_i were not kept constant within one parameter series.

The results form literature will be compared with the results from the present study, which were acquired as described in the following section.

6.3 Experimental procedure

The same halved tube samples, which were used to measure the W coating thicknesses (Section 3.1.3), were also used to evaluate the influence of the CVD process parameters on the W grain width.

6.3.1 Sample evaluation

The embedded and polished samples were etched for 30 seconds with an active oxide polishing suspension "OP-S" with addition of an alkali with a OP-S to alkali ratio of 8:1. The alkali was a mixture of 5 g KOH and 5 g $K_3Fe(CN)_6$ in 50 ml H_2O.

After etching, three images per tube side, next to the position where R_W was maximal, were captured and merged. The images were post-processed in Photoshop CS6 [126]. After adjusting the brightness and the contrast, they were rotated so that the surface was parallel to the bottom. Lines were placed on top of the images with distances of 67, 133, 200, and 267 µm to the substrate. Along these lines the grain widths were measured. Writing a Python script for finding the intersections with the boundaries did not succeed in appropriate time. Therefore, it was faster to place the markers manually and to write a Python script only for the evaluation of the marker coordinates. The manual marking was done within the graph analyzing tool DigitizeIt [127]. Here, the x-axis was aligned parallel, and the y-axis perpendicular to the surface, respectively, with $y = 0$ being at the surface. In this way, a total of around 17 500 carefully considered markings were placed. As example, a section of a marked picture is shown in Figure 6.2.

Unfortunately the grain boundaries were not always obvious, thus a lot of intuition and revision was needed to obtain a comprehensive overall understanding for the parameter influence on the grain width. One reason was the following: In preparation of the measurement of the W coating thickness, four deposited half tubes were embedded at once, which allowed for four times faster grinding and polishing. However, after several months, this embedding material deformed slightly from drying. Therefore, in preparation of the grain width analysis, during etching, the distance between polishing disc and sample was less uniform. This caused the W depositions from the different IDs to get etched less uniformly. The etching results for #1090 and #1093 were too bad to be evaluated. However, since these IDs showed to be not critical for the overall understanding, they were left out. Still, spending more time for better pictures would have probably saved a lot of time in the evaluation.

The Python script for the grain widths evaluation had the following input and output.

Input: Dataset exported from DigitizeIt [127] as a single *.csv-file with unsorted x and y coordinates of the intersections between the grain boundaries and surface parallels.

Output: Minimal, mean, and maximal grain widths for each slice, tube side and ID.

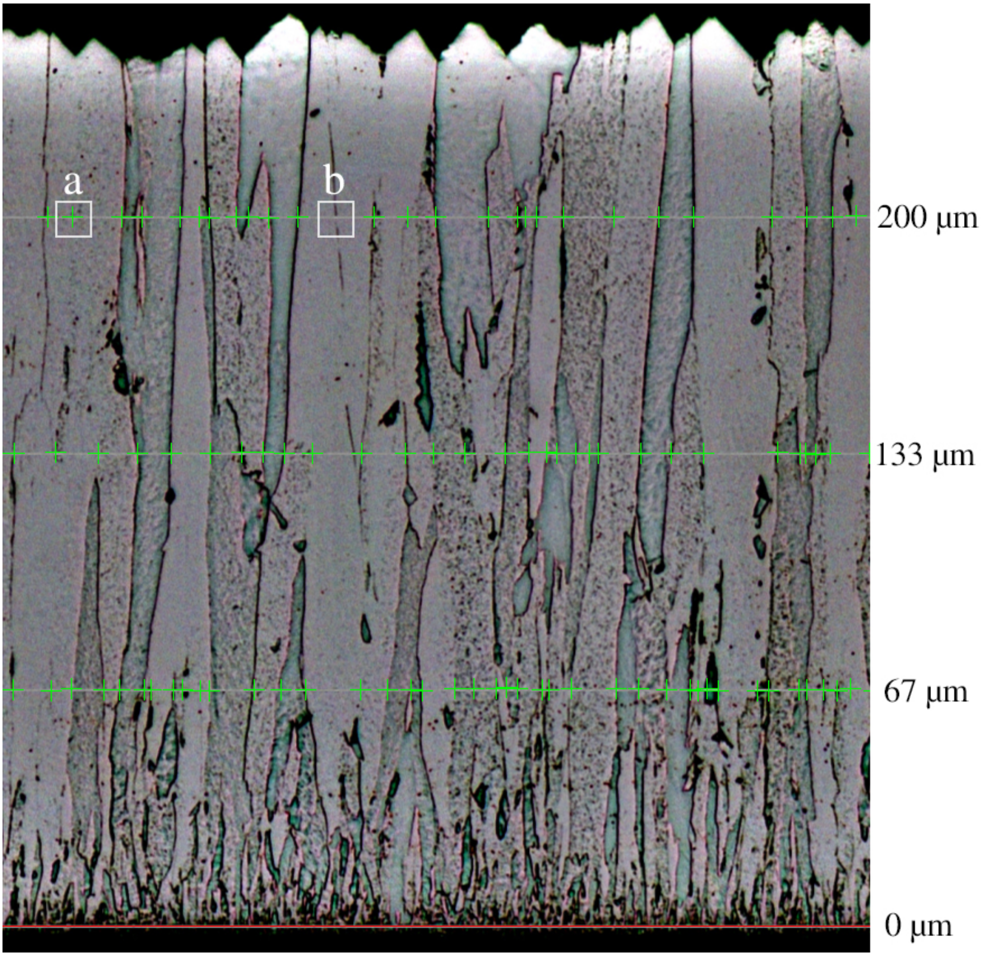

Figure 6.2: Grain structure of the W coating on the tube inner surface (sample ID 1100, near R_{max}). In addition, parallels are displayed with manually placed markers (+) for the grain width evaluation. Feature a: only very pale boundary, but in combination with clear undamaged grain on surface, a grain boundary is very likely at this position. Feature b: no grain boundary but just an artifact (a scratch) with a degenerated pyramid at the surface caused by the sample preparation.

6.4 Grain width results

6.4.1 H_2 partial pressure variation

In Figure 6.3 the grain widths are plotted versus the coating thickness, which equals the distance of the evaluated slice towards the substrate surface.

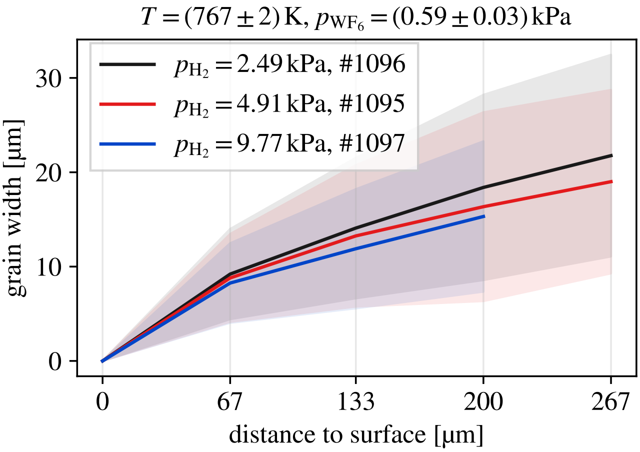

Figure 6.3: p_{H_2} variation: Mean (solid lines), minimum and maximum (filled areas) grain widths vs. distance to surface. The nearly constant parameters are provided in the heading, whereby the given uncertainties refer to the difference in the mean values for each ID.

First, it can be seen that the grain width increases significantly for higher thicknesses, as also observed and explained in the literature [118, 119, 121]. This trend can be seen in the following grain width vs. grain thickness plots as well. Therefore, the grain fineness in W_f/W can further be optimized by keeping the CVD growth thickness within the bulk CVD-W as low as possible. This can be achieved by placing the fabrics vertically as close as possible and the fibers horizontally only as far as necessary to avoid macropore formation.

Second, it can be seen that the grains become slightly finer with increasing p_{H_2}. This matches to the results of Chang et al. [125], whereas these new results, compared to the results of Chang et al., are quantitatively and p_{WF_6} was kept nearly constant within the series. The reason for the observed trend is most likely the higher nucleation rate for larger p_{H_2}. The higher nucleation rate leads to more grains and thus also to more of the fastest growing $\langle 100 \rangle$ orientated grains without having more space making them smaller. To conclude, a higher p_{H_2} results in finer grains.

6.4.2 WF_6 partial pressure variation

In Figure 6.4 the grain widths are shown for the p_{WF_6} variation.

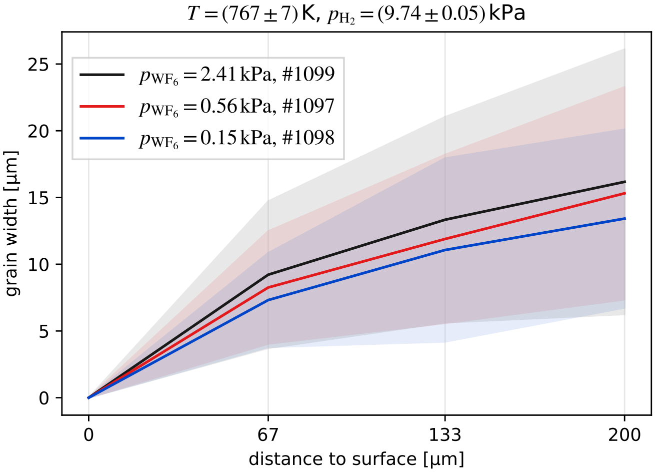

Figure 6.4: p_{WF_6} variation: Grain width vs. distance to surface.

In the investigated regime the grain width increases with increasing p_{WF_6}. This is again matching to the observations of Chang et al. [125]. Interestingly, this trend contrasts with the variation of p_{H_2}. The explanation could be that the more WF_6 atoms adsorb, the more the adsorption of H_2 atoms is hindered, which is also needed for the formation of a stable nucleus and its further growth. Kajikawa et al. reported that the W nuclei need a critical size to become stable, otherwise they dissociate again [128]. Further, as discussed in the previous chapters, the investigated process parameter range belongs to the regime where the deposition rate is independent of p_{WF_6}. Therefore, a larger p_{WF_6} does not increase the probability that a nucleus grows beyond the critical size. It is rather the opposite as H_2 is more likely to be blocked off from the surface by F. Therefore, a larger p_{WF_6} decreases the W nucleation rate within the regime with already sufficient amount of WF_6 (Zone III in Section 3.4). This leads to larger grain widths as explained in the p_{H_2} variation subsection. In the parameter regime where p_{WF_6} limits R_W (Zone I-II), the trend is probably opposite. To conclude, a lower p_{WF_6} results in finer grains (in Zone III).

6.4.3 Temperature variation

The difficulty with the T variation is that it also varies the p_i within the sample even for constant inlet conditions as shown in the previous chapters for the T_H variation (#1100, 1086, 1101). One either has to know in advance, how much the inlet conditions have to be adjusted, in order to get a constant p_i at the measuring point despite the different T, or, one has to be lucky. With the new model helping to calculate the needed inlet flows, the experiments could have been repeated to achieve constant p_i. However, fortunately, for the #1091, 1094, p_{H_2} and p_{WF_6} were already very similar at the reaction position. The corresponding plot is shown in Figure 6.5.

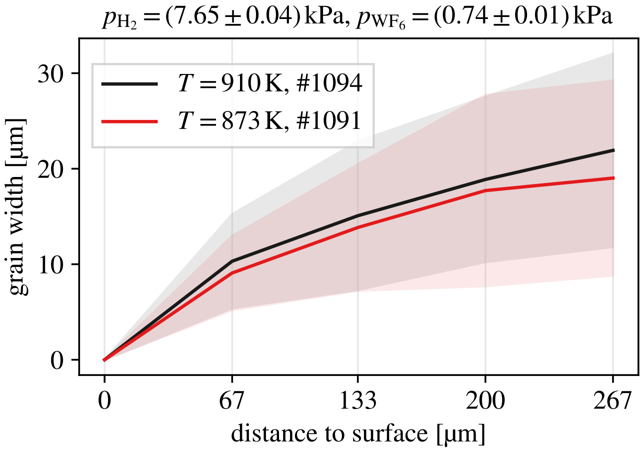

Figure 6.5: T variation: Grain width vs. distance to surface.

The result shows that the grain width slightly increases with increasing T. This is controversial to several results from the literature [118, 124, 125]. However, Shi et al. stated that a lower T leads to a higher nucleation rate [121]. This supports that a lower T should result in finer grains, especially since a lower T also reduces R_W, so that the substrate surface is more slowly completely covered by W, allowing more nuclei to form. The T trend will be confirmed in the next subsection. To conclude, a lower T results in finer grains (>550 K).

6.4.4 Overview plot: grain width vs. varied parameters

The grain width analysis is comprehended in Figure 6.6, in which the grain widths for all 13 investigated IDs are plotted together. In preparation, the grain widths of the 133 and 200 µm slices were averaged for each ID. The averaged grain widths are plotted versus the p_{H_2} and are separated in three T ranges (symbols). Furthermore, a color map is applied for the p_{WF_6}.

From Figure 6.6, the following conclusions can be drawn:

1. Via the inclusion of the p_{H_2} and p_{WF_6} dependencies, the data points can nicely be grouped by the three different T ranges.

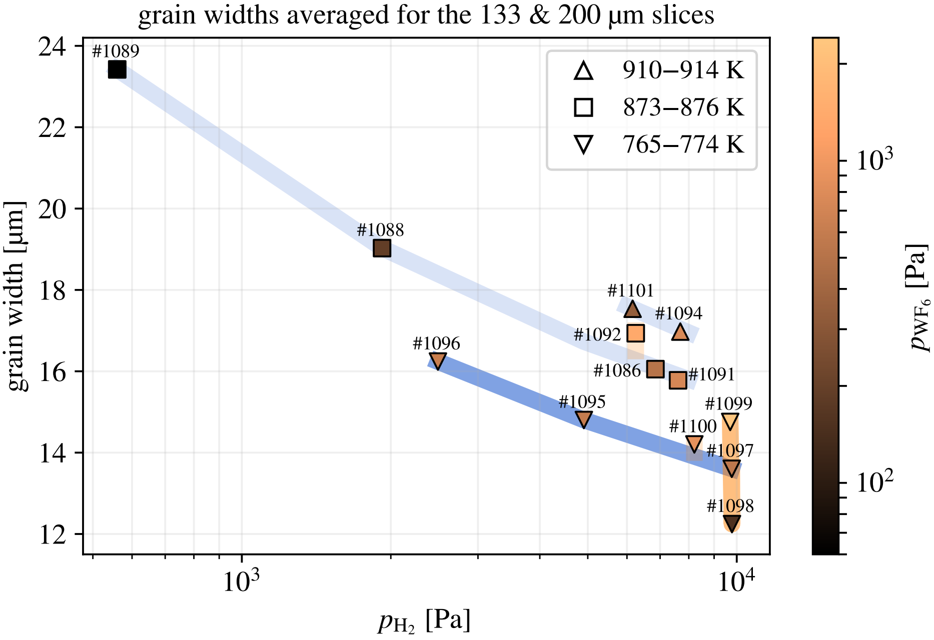

Figure 6.6: Grain width vs. p_{H_2} for different T (symbols) and p_{WF_6} (color map). The blue and copper lines mark the parameter sets for the p_{H_2} and p_{WF_6} variation, respectively. The pale blue and pale copper lines show the similar trends for higher T, shifted upwards.

2. The reciprocal trend of the p_{H_2} (blue) vs. the grain width is well visible and also holds well for all the other evaluated experimental results.

3. The trend of a finer grain for a lower p_{WF_6} (copper) matches for most of the results. Few samples did not follow this trend. The reason could be overlaying effects due to the change of all p_i and not only p_{WF_6} (#1101 and #1094). Further, the grain widths of #1088 could be a bit overestimated, since it was slightly overetched, so that some grain boundaries could have been hidden behind etching marks.

4. If the parameter regime changes from Zone III to II (Section 3.4), the nucleation rate is probably reduced with reducing p_{WF_6}. This would explain the large grains in sample #1089 produced within Zone II. Further, this leads to the assumption that there is a p_{WF_6} sweet spot for fine grains within Zone III right before the transition from Zone III to II, as it is the same for the pore infiltration. However, more data is needed to validate this.

5. Overall, only by changing the process parameters the average grain width were changed significantly by almost factor two at the same coating thickness.

6.5 Chapter conclusions

Finer grains improve the mechanical properties of the W matrix within a W_f/W composite. Furthermore, finer surface grains improve the surface-to-surface contact integrity of the CVD-W surfaces that started to grow from adjacent fibers.

The grain widths of the columnar CVD-W have been evaluated and correlated to the actual synthesis conditions at the evaluated position. The conditions were calculated via experimentally validated simulations under consideration of the gas consumption. The dependencies on coating thickness and partial pressures p_i already observed in the literature were confirmed. Furthermore, an overview plot with 13 process parameter sets revealed a newly discovered grain width-to-temperature dependence Figure 6.6.

To achieve finer CVD-W grain widths one should aim for:

- low coating thickness (also lowers grain lengths),
- high $p_{\mathrm{H_2}}$,
- low $p_{\mathrm{WF_6}}$ (while still staying in Zone III), and
- low T.

These trends can most likely be extrapolated to even finer grains than obtained within this study. How the newly gained knowledge can be applied will be described in the following chapters.

7 Using the gained knowledge to improve W$_f$/W

In overlap to the PhD work presented in this thesis, a fellow PhD student, Daniel Schwalenberg, produced a 15-layered W$_f$/W mock-up, whereby the results from the present thesis were already applied.

7.1 Deciding the fabric geometry parameters

Since the fabrics 1-5, shown in Figure 4.2, were still available, and designing and weaving new ones would have taken several months, it was decided to use fabric 4, which resulted from the earlier experiments for 48 pores from one slice in $X_{ff} = (210 \pm 31)$ µm, $Y'_{ff} = (27 \pm 12)$ µm, and $Y_{fg} = (64 \pm 28)$ µm (the parameter meaning is repeated in Figure 7.1). On the one hand, due to the fiber position deviations, a rather high X_{ff} had to be chosen for a good average ρ_{rel}, which lowered Φ_{V_f}. On the other hand, this large X_{ff} caused that the fiber stiffness did not negatively effect the flattening after weaving, so that Y'_{ff} of the chosen fabric 4 was much lower compared to that of e.g. fabric 1 (27 instead of 82 µm), which increased ρ_{rel} and Φ_{V_f} again.

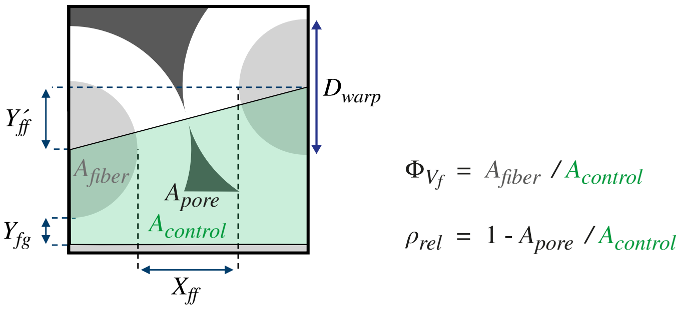

Figure 7.1: Repetition of the variables Y'_{ff}, Y_{fg}, X_{ff}, Φ_{V_f}, and ρ_{rel}.

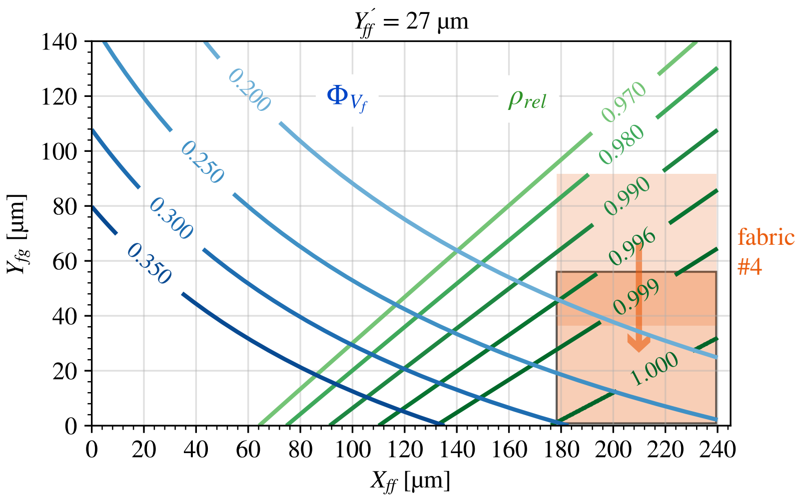

Figure 7.2: Contour plot for the quantities in Figure 7.1 with fabric 4 values marked.

In Figure 7.2 the positional parameters for fabric 4 are marked for the average of Y_{ff}' (upper orange rectangle). For the new experiments the advice was given to take extra care for an as low as possible Y_{fg} to improve Φ_{V_f} and ρ_{rel} as it is illustrated in form of the lower orange rectangle in Figure 7.2. For improvements beyond, new fabrics are needed. Concrete suggestions are given in Chapter 8.

7.2 Deciding the CVD process parameters

Table 7.1 summarizes the overall advantageous CVD process parameters for the W_f/W synthesis, which are based on the trends for the different criteria: fine W grains, uniform pore infiltration (microscale), uniform sample coating (macroscale), and lower process cost.

Table 7.1: Summary of advantageous CVD process parameter trends

	physical CVD parameters				
criteria	T	p_{WF_6} [1]	p_{H_2} [1]	p_{HF}	section
fine W grains	↓	↓	↑		6.4
uniform pore infiltration	↓	↓	(↓)	↓	5.1
uniform sample coating	↓	↓	↑	↓	4.2.2
lower process cost	∼	↓	∼	∼	7.2
overall	↓	↓	↑	↓	

[1] deposition rate is not limited by too low p_{WF_6}

The uniformity is influenced the most by T. Fortunately, also the grain fineness trend points into the same direction. Thus, the overall best for the material properties is to use a low T. Regarding the production cost, a lower T reduces the needed heating energy. However, at the same time, the process duration is increased. Therefore, as a compromise, it was decided to decrease T_H by 100 K from 873 to 773 K, whereas the surface T was estimated to (753±10) K. For each layer T_H was increased by 1.5 K to compensate for the increasing distance to the heater core.

The advantageous trends for p_{H_2} do not point into the same direction. However, the influence on the pore infiltration is minor, and the benefits on fine grains and macro-scaled uniformity by using a high p_{H_2} overweight. A higher $\dot{V}_{\mathrm{h}_2}^{inlet}$ increases the cost per time slightly as more H_2 is consumed and the convective cooling slightly increased. However, with 1 mole H_2 costing roughly only a factor of 0.0008 of that of WF_6, the impact is rather small and furthermore, the resulting increased p_{H_2} decreases the deposition duration and thus the cost again. Therefore, the cost influence of p_{H_2} is valued neutral. Overall, an increased p_{H_2} is beneficial. Thus, P_{tot} was increased from 9.5 to 12 kPa (current limit of the CVD machine) and $\dot{V}_{\mathrm{h}_2}^{inlet}$ from 1500 to 2500 sccm. The higher $\dot{V}_{\mathrm{h}_2}^{inlet}$ also decreases p_{HF} as the produced HF is rinsed away more effectively.

The advantageous trends for p_{WF_6} goes in the same direction (low) for all criteria. A lower p_{WF_6} can be achieved by lowering $\dot{V}_{\mathrm{WF}_6}^{inlet}$, and or increasing U_{WF_6}, which saves expensive WF_6 and improves the pore filling. However, as explained in the sections about the pore infiltration (Section 5.1) and the grain size (Section 6.4.4), WF_6 may not deplete and become the rate limiting factor (R_{W} should stay independent of p_{WF_6} as in Zone III (Figure 3.17)). The respective $\dot{V}_{\mathrm{WF}_6}^{inlet}$ was estimated via the Reactor Model developed within this work (Section 4.2) with additional geometry modifications. The heating plate diameter was increased to the diagonal lengths of the experimental square heating plate so that WF_6 will for sure not deplete in the edges. Further, since the reaction surface area increases during the deposition process, a grown-together lower fabric layer was modeled as ground, and an upper fabric layer was modeled with an increased r_{fiber}. The geometry for this stationary simulation is shown in Figure 7.3a,b. In Figure 7.3c R_{W} along the first layer surface versus the heating plate radius is shown.

As it can be seen, a $\dot{V}_{\mathrm{WF}_6}^{inlet}$ of 100 sccm is not sufficient. Towards the edge, R_{W} drops significantly within the pores as WF_6 depletes leading to a change in the reaction regime from Zone III to II. This would lead to larger pores and thus a reduced ρ_{rel}. A $\dot{V}_{\mathrm{WF}_6}^{inlet}$ of 150 sccm would probably be sufficient; however, as it is difficult to perfectly align the gas shower (central and perpendicular), 200 sccm was chosen.

In the former experiments, R_{W} could be estimated only very roughly. To ensure nevertheless that the previous fabric layer is infiltrated before it is covered by the next layer, Δt had to be chosen quite high. With the new model, R_{W} can be predicted with a

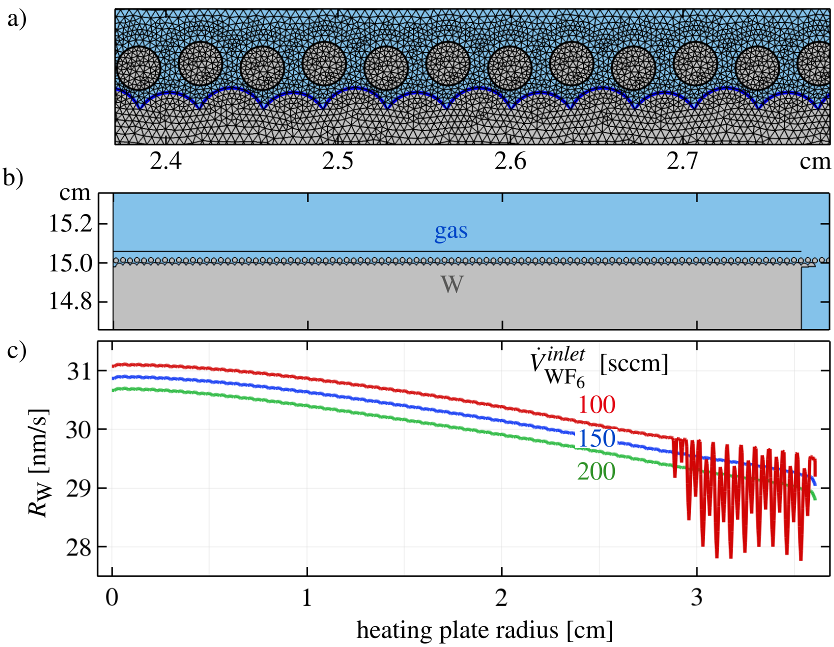

Figure 7.3: Model geometry and R_W results for the reactor model with a second fabric layer for determining a good value for $\dot{V}^{inlet}_{WF_6}$, with a) showing a zoomed section of b), and c) showing R_W along the first layer surface, which is marked in blue in a).

much smaller error so that Δt can be calculated more precisely, which leads to a higher vertical fabric packing density and thus to a larger Φ_{V_f} without reducing ρ_{rel}. Δt was changed from 45 min to 78 min, which is only larger because of the lower T, but still results in a smaller W coating thickness on top of the fabrics.

In Table 7.2 the former and the improved process parameters are summarized.

Table 7.2: Former and improved CVD process parameters.

T_{Heater}	[K]	873	→	773
P_{tot}	[kPa]	9.5	→	12
$\dot{V}^{inlet}_{H_2}$	[sccm]	1500	→	2500
$\dot{V}^{inlet}_{WF_6}$	[sccm]	400	→	200
Δt	[min]	45	→	78

7.3 Experimental W_f/W results applying the new parameters

In Figure 7.4, the effect of the different CVD process parameter sets on the W_f/W metallographic microstructure is shown. With respect to the pore structure, it looks better with the new parameters, however the difference is small. The reason is that also with the old setup the pores got filled already quite uniformly, because of the large X_{ff}, and because the process was run already in Zone III.

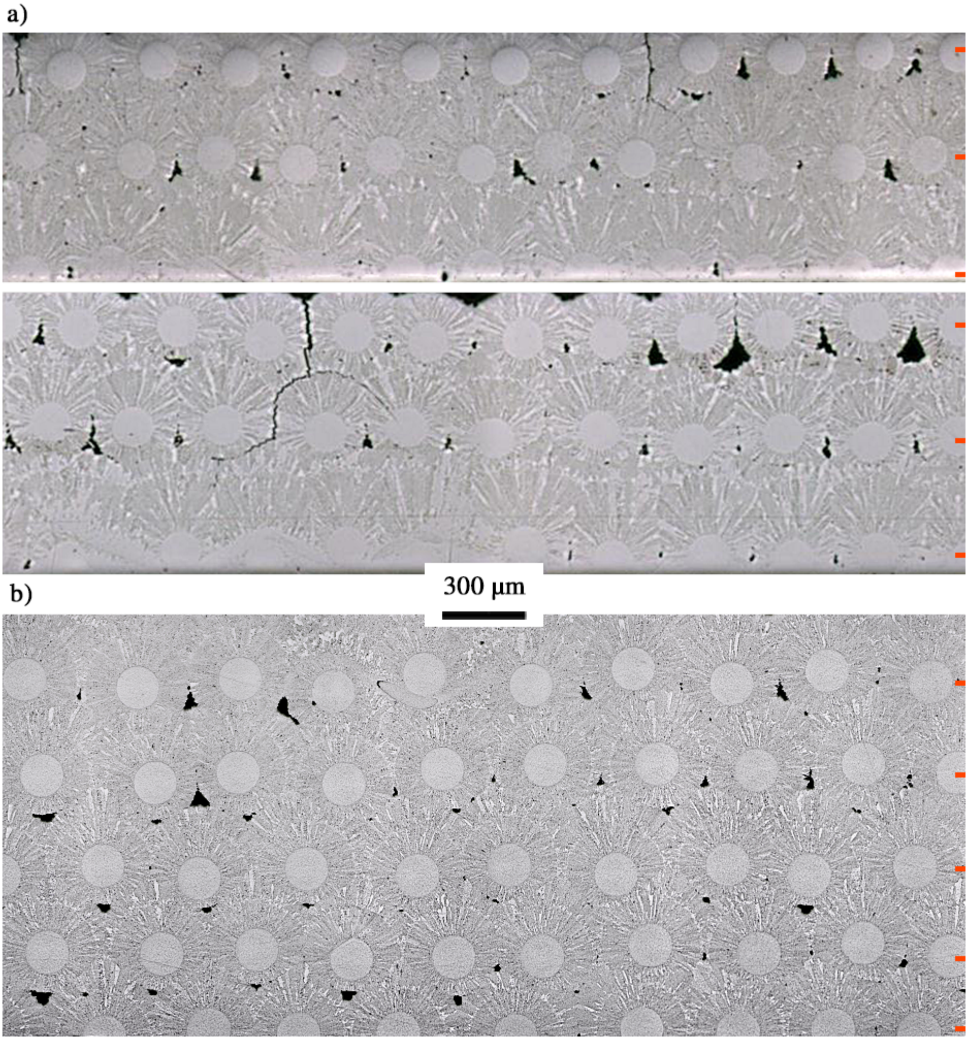

Figure 7.4: W_f/W samples produced with the former (a) and improved (b) CVD parameters from Table 7.2

Besides the small improvement of ρ_{rel}, the new parameters brought many additional benefits:

1. More compact vertical fabric placement (right red markers), thus a higher Φ_{V_f} and better fiber reinforcement.
2. More uniform macroscopic sample coating thickness (a reduced "bump" in the sample center).
3. Finer grain structure and thus improved mechanical properties.
4. Lower WF_6 demand (improved consumption rate).
5. Improved understanding of the process.

Furthermore, the new sample did not show cracks. This could be due to the stronger matrix-to-matrix contact integrity (micropores became smaller), which was also achieved by the new parameters. However, other facts reduced the risk for cracks as well. The additional fabric layers increased the sample thickness and fracture strengths. Further, the lower T led to less thermal mismatch stresses while cooling down (Cu heating plate: $\alpha_{\mathrm{Cu}} = 1.65 \times 10^{-5}\ \mathrm{K}^{-1}$, W_f/W: $\alpha_{\mathrm{W}} = 4.5 \times 10^{-6}\ \mathrm{K}^{-1}$ [129]).

It should be noted that in the new sample some areas resulted in larger pores than before. However, the reason for this was not the chosen process parameter set, but fabric deformations during suboptimal storage, or W pieces that fell off from inside the co-coated gas shower onto the fabric, immediately sealing the pores. Both can be avoided in future by a better fabric storage and by cleaning the gas shower more regularly.

8 Thesis conclusions and outlook

The goal of this dissertation was to provide a deep and quantitative process understanding to improve the material properties of W_f/W via the parameters of the CVD process (T, P_{tot}, $\dot{V}_i^{inlet}$) and the fabric geometry (fiber diameters and positioning). This goal was achieved with success. The developed models, scripts, and parameter studies allowed for optimizing the parameters with respect to the grain morphology, relative density, fiber volume fraction, and WF_6 consumption (production cost efficiency). Furthermore, first experimental results applying the theoretical optimization looked very promising. The process understanding gained and the models and methods developed will also allow in future to design new and advanced W-CVD setups with less trial-and-error, and can even be applied on 3D models.

One restriction should be pointed out though. The rate equations presented are based on the deposition on CVD-W or steel and should therefore not be relied upon blindly to predict the deposition rate within the first few minutes on any substrate where surface roughness, sticking coefficients and epitaxy are dominant. For example the selective character of W-CVD was not considered in the model. It is known that for certain process parameters (lower T and a much lower P_{tot}), W coats metals but not SiO_2 [69–71]. For the future it could prove valuable to test whether this can be useful for the W_f/W synthesis. If this phenomenon could be applied to the W_f/W production, where the fabric is coated by a non-metallic interface, and if an educt depletion would be avoided, this would lead to a relative density of 100%, as *only* the heating plate coating would grow upwards, so that pores between the fibers would remain accessible for being filled. A disadvantage would be the significantly increased deposition duration. However, advantages besides gaining 100% density would be that even lower fiber distances could be used (higher fiber volume fraction) and several fabrics could be stacked within one deposition process or more complex 3D substrate structures could be infiltrated. Lower fiber distances would have the additional benefit of a finer averaged grain width and especially grain length improving the mechanical properties.

Furthermore, an option for significantly finer W grains could be to introduce short flow pulses of a gas that forms additional nuclei of a new element with a different crystal structure and or orientation and thus forces the W to form new nuclei as well. Ideally the new elements result in an advantageous alloying such as e.g. Cr for self-passivating W [130]. Besides these suggestions two more are presented in the following final sections.

Suggestions to improve the W fabric (CVD substrate)

Positional deviations of the fibers cannot be controlled well with the current fabrics. These deviations can result in large pores if they lead to small X_{ff}, large Y'_{ff} or Y_{fg} (parameter explanation re-shown in Figure 8.1). Reducing these deviations would allow to reduce the safety margin regarding the average X_{ff} that results in a ρ_{rel} near one, which would improve Φ_{V_f} and reduce the average grain size as mentioned earlier.

Furthermore, the fiber and fabric stiffness should be reduced, so that Y_{fg} and Y'_{ff} can be close to their theoretical minimum, which will also improve Φ_{V_f} and ρ_{rel}. However, for ordinary fibers, those two goals behave contrary to each other, since less stiffness leads to a more loose fabric and thus to larger positional deviations. Here, the replacement of the warp fiber by a warp yarn of thin filaments could be the solution. The W-CVD infiltration and mechanical properties of four different yarn types were investigated [131]. The best performance was achieved with the yarn shown in Figure 8.2.

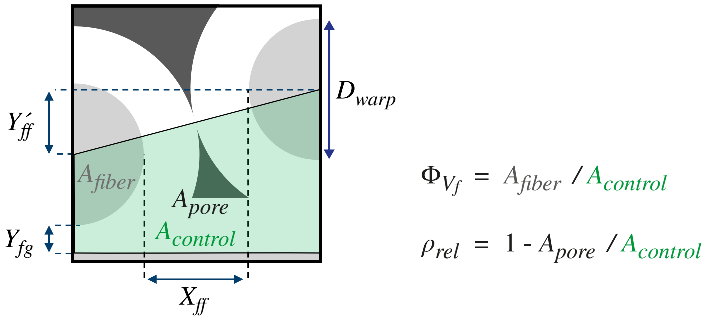

Figure 8.1: Repetition of the variables Y'_{ff}, Y_{fg}, X_{ff}, Φ_{V_f}, and ρ_{rel}.

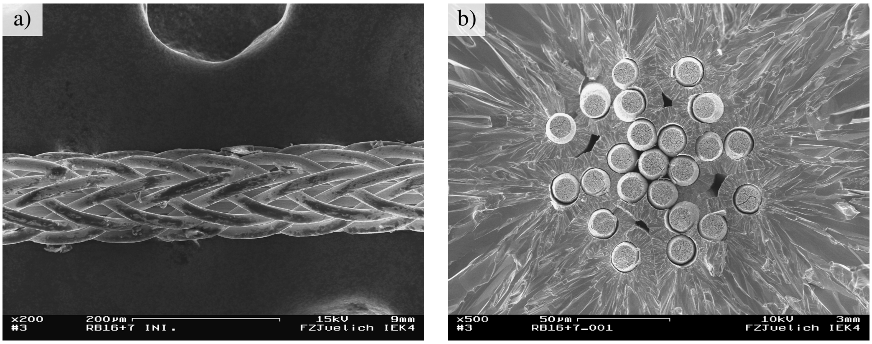

Figure 8.2: Yarn with 16 braided outer filaments and 7 densely packed and axially twisted core filaments (16_s7_c), with an outer diameter of 130 µm and a filament diameter of 19 µm [131]. a) uncoated and side view, b) after W coating, cross-sectional fracture surface.

This braided yarn has a much lower stiffness compared to a solid fiber, therefore the fabric should behave more like a sheet of textile, which can probably be flattened and pressed by an iron-equivalent down on the previous layer, reducing Y_{fg} and thus increasing Φ_{V_f} and ρ_{rel} of W_f/W further. In addition, the weft fiber cannot move as freely along the warp yarn surface compared to the a smoothly drawn warp fiber surface, since the braided filaments creates a rougher surface (Figure 8.2a), which could lead to less positional deviations due to an increased friction.

Another problem with weaving the 150 µm W warp fibers were curved deformations and thus residual stresses caused by coiling them for transportation and storage. This led by a large portion to the positional deviations or even to a fabric bending, due to stress relaxation. Here, the yarn will have an additional large benefit due to its high flexibility whereby additionally 16 µm filaments within the yarn have a higher fracture strength than the 150 µm fiber [132].

Furthermore, it would be beneficial to reduce the weft fiber diameter (D_{weft}) from 50 to 40 or even 30 µm. This would further reduce the average Y'_{ff} and Y_{fg} and thus increase Φ_{V_f} and ρ_{rel}. Whether $D_{weft} = 30$ µm is possible needs to be tested. A 20 µm weft fiber broke too often during weaving as tested by H. Gietl during his PhD. The smaller D_{weft} also allows for a reduced distance between each weft fiber, which results in an increased Φ_{V_f} and in a better fabric stability. Furthermore, a smaller weft fiber distance would reduce the isotropy of the mechanical properties, as with the current large distance the composite is only very strong parallel to the warp fibers but weak parallel to the weft fibers.

To summarize, D_{weft} should be reduced from 50 to 40–30 µm and the weft fiber distance from 2–3 mm down to what is technically feasible (but > warp fiber distance). Furthermore, the 150 µm warp fiber should be replaced by a yarn (16_s7_c). In a second iteration the warp fiber distance could be reduced based on the performance of a new fabric prototype. And finally, the fabrics have to be placed as flat as possible and stacked vertically as close as possible.

Suggestion to improve a continuous W_f/W production

The approach for a continuous W_f/W production via CVD is presented in [54, 133]. In this configuration, a long W fabric is slowly unwound from an unheated coil and wound onto a heated coil, where the CVD takes place. Advantages besides the continuity are that contaminations due to chamber openings are avoided and that the fabric is pressed under tension onto the prior layer (lowest possible Y_{fg}). A problem is that due to heat conductivity the fabric can be coated already while still being straight, resulting in damage to the coating when it is wound up.

A possible solution could be to apply the model to obtain the process parameters for which WF_6 depletes along the coil. The concept is sketched in Figure 8.3a.

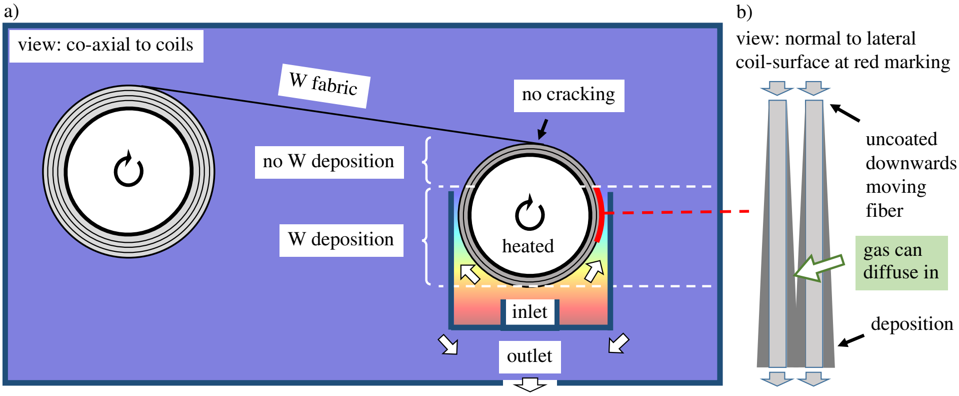

Figure 8.3: Schematic of how to improve the continuous W_f/W production (a simulated p_{WF_6} colormap would look slightly different). a) CVD setup, b) deposited fibers at the transition towards WF_6 depletion.

For high T and low $\dot{V}_{WF_6}^{inlet}$ the slowly rotating right coil will be, as a metaphor, only partially dipped into a WF_6 bath. Furthermore, this setup should result in the CVD-W matrix surfaces no longer coming into contact simultaneously along the almost parallel fibers, but rather like a "zipper", as illustrated in Figure 8.3b. This should lead to a much better pore infiltration, as an open entrance remains and also the problematic micropores along the matrix-to-matrix interface could be reduced strongly despite of the larger grains. Finally, the resulting coating thickness *between* the layers should remain uniform as each position should receive a similar total amount of W while being rotated uniformly through the stationary gas flow.

9 Appendix

The Python scripts shown in this Appendix and the Comsol model files (Single-fiber-tube Model, Reactor Model, and Single pore Model) can be downloaded from `https://github.com/Leo-Raumann/Dissertation-Files.git`.

9.1 Material and species properties

Table 9.1: Properties as used in the model, formatted for copy-paste

magnitude;[unit];	species;	value;	reference
density ρ;[kg/m^3];	W(s);	19 250;	[86, 87]
density ρ^0;[kg/m^3];	WF6(g);	12.4;	[92]
dipol moment μ_D;[D];	H2(g);	0;	not polar
dipol moment μ_D;[D];	HF(g);	1.826178;	[134]
dipol moment μ_D;[D];	WF6(g);	0;	not polar
emissivity ϵ_{rad};[-];	Steel 1.4571;	0.35;	intern
emissivity ϵ_{rad};[-];	W(s);	0.3±0.1;	intern
heat capacity c_p;[J/mol/K];	H2(g);	(3.300+2.231e-4*T+9.555e-8*T^2+3.143e1/T)*R;	fit to [94]
heat capacity c_p;[J/mol/K];	WF6(g);	(2.167e1-1.510e-3*T+3.079e-7*T^2-2.069e3/T)*R;	fit to [94]
heat capacity c_p;[J/mol/K];	HF(g);	(3.080+4.544e-4*T+1.990e-8*T^2+8.849e1/T)*R;	fit to [94]
heat capacity c_p;[J/mol/K];	W(s);	(2.882+4.094e-4*T+4.918e-8*T^2-2.514e1/T)*R;	fit to [94]
heat capacity c_p;[J/kg/K)];	Steel 1.4571;	500;	[135]
molar enthalpy h;[J/mol];	H2(g);	(3.450e-3+1.258e-8/2*T+5.657e-11/3*T^2-1.030/T)*RT;	fit to [94]
molar enthalpy h;[J/mol];	WF6(g);	(1.417e-2+3.152e-6/2*T-7.055e-10/3*T^2-2.116e2/T)*RT;	fit to [94]
molar enthalpy h;[J/mol];	HF(g);	(3.434e-3+2.377e-8/2*T+5.261e-11/3*T^2-3.381e1/T)*RT;	fit to [94]
molar enthalpy h;[J/mol];	W(s);	(2.793e-3+2.509e-7/2*T+6.878e-12/3*T^2-8.554e-1/T)*RT;	fit to [94]
molar entropie s;[J/mol/K];	H2(g);	(3.490*ln(T)-6.012e-5*T+1.043e-7/2*T^2-4.156)*R;	fit to [94]
molar entropie s;[J/mol/K];	WF6(g);	(1.312e1*ln(T)+8.529e-3*T-1.565e-6/2*T^2-3.618e1)*R;	fit to [94]
molar entropie s;[J/mol/K];	HF(g);	(3.498*ln(T)-8.707e-5*T+1.096e-7/2*T^2+9.911e-1)*R;	fit to [94]
molar entropie s;[J/mol/K];	W(s);	(2.788*ln(T)+5.122e-4*T+7.961e-9/2*T^2-1.211e1)*R;	fit to [94]
potential characteristic lengths σ;[Å];	H2(g);	2.827;	[95]
potential characteristic lengths σ;[Å];	HF(g);	3.148;	[136]
potential characteristic lengths σ;[Å];	WF6(g);	4.973+9.284e-4*T+6.582e-7*T^2-7.315e-10*T^3;	[137]
potential energy minimum ϵ/k_B;[K];	H2(g);	59.7;	[82]
potential energy minimum ϵ/k_B;[K];	HF(g);	330;	[136]
potential energy minimum ϵ/k_B;[K];	WF6(g);	819.9-1.06*T+6.19e-4*T^2-6.62e-8*T^3;	[137]
thermal conductivity k;[W/m/K];	Steel 1.4571;	11.3+0.0127*T;	intern
thermal conductivity k;[W/m/K];	W(s);	207.24-0.269*(T+273)+3e-4*(T+273)^2+1e-7*(T+273)^3;	[86]

9.2 Detailed results for the single fiber setup

Table 9.2: Inside the **steel tube**: $R_{exp,max}$, $R_{sim,max}$, and T and p_i at the surface position of $R_{sim,max}$.

ID	$R_{exp,max}$ [nm/s]	$R_{sim,max}$ [nm/s]	$T@R_{sim,max}$ [K]	$p_{H_2}@R_{sim,max}$ [kPa]	$p_{WF_6}@R_{sim,max}$ [kPa]
#1086	121.7 ± 8.4	125.1 ± 8.3	874.6 ± 6.6	6.85 ± 0.16	0.51 ± 0.06
#1088	62.5 ± 3.3	66.9 ± 5.8	875.4 ± 6.5	1.92 ± 0.03	0.19 ± 0.0
#1089	28.8 ± 2.3	32.3 ± 4.8	874.7 ± 6.6	0.56 ± 0.07	0.06 ± 0.01
#1090	139.4 ± 5.1	134.4 ± 11.1	871.4 ± 6.9	8.52 ± 0.01	0.35 ± 0.02
#1091	133.2 ± 7.0	129.8 ± 9.9	873.3 ± 6.8	7.61 ± 0.07	0.73 ± 0.04
#1092	120.7 ± 6.4	118.4 ± 8.2	873.9 ± 6.8	6.25 ± 0.14	1.36 ± 0.05
#1093	127.6 ± 9.8	121.1 ± 9.5	871.8 ± 6.9	6.86 ± 0.06	1.58 ± 0.03
#1094	189.5 ± 9.7	196.7 ± 15.0	910.1 ± 7.2	7.69 ± 0.05	0.75 ± 0.03
#1095	24.5 ± 1.5	25.6 ± 3.1	767.2 ± 7.3	4.91 ± 0.07	0.6 ± 0.01
#1096	18.1 ± 1.0	17.7 ± 2.4	765.3 ± 7.6	2.49 ± 0.07	0.62 ± 0.02
#1097	34.8 ± 2.1	36.8 ± 4.2	768.6 ± 7.1	9.77 ± 0.06	0.56 ± 0.0
#1098	33.4 ± 1.9	37.3 ± 4.2	769.5 ± 7.0	9.78 ± 0.06	0.15 ± 0.01
#1099	34.2 ± 2.9	34.9 ± 4.3	765.3 ± 7.6	9.7 ± 0.03	2.41 ± 0.0
#1100	33.9 ± 2.1	36.2 ± 3.6	773.3 ± 6.6	8.21 ± 0.02	0.9 ± 0.02
#1101	185.2 ± 10.3	182.3 ± 10.4	913.3 ± 7.0	6.16 ± 0.21	0.34 ± 0.08

Table 9.3: At the **W fiber**: $R_{exp,max}$, $R_{sim,max}$, and T and p_i at the surface position of $R_{sim,max}$.

ID	$R_{exp,max}$ [nm/s]	$R_{sim,max}$ [nm/s]	$T@R_{sim,max}$ [K]	$p_{H_2}@R_{sim,max}$ [kPa]	$p_{WF_6}@R_{sim,max}$ [kPa]
#1086	120.4 ± 3.4	120.9 ± 8.7	871.8 ± 7.2	6.79 ± 0.18	0.58 ± 0.05
#1088	60.9 ± 1.9	65.1 ± 6.1	872.9 ± 7.0	1.92 ± 0.03	0.2 ± 0.0
#1089	29.1 ± 1.0	31.5 ± 4.9	872.2 ± 7.1	0.56 ± 0.07	0.06 ± 0.01
#1090	133.1 ± 2.5	125.3 ± 11.4	865.3 ± 7.5	8.51 ± 0.02	0.4 ± 0.02
#1091	128.3 ± 3.1	123.4 ± 10.3	869.0 ± 7.4	7.57 ± 0.09	0.79 ± 0.03
#1092	115.3 ± 3.0	112.5 ± 8.6	870.0 ± 7.4	6.15 ± 0.16	1.42 ± 0.05
#1093	113.0 ± 3.0	109.5 ± 9.7	863.4 ± 7.7	6.79 ± 0.08	1.62 ± 0.03
#1094	169.1 ± 4.0	173.9 ± 15.2	898.7 ± 8.0	7.64 ± 0.07	0.82 ± 0.03
#1095	22.4 ± 0.6	21.2 ± 3.0	755.0 ± 7.9	4.92 ± 0.07	0.6 ± 0.01
#1096	13.6 ± 0.4	12.5 ± 2.0	743.0 ± 8.5	2.48 ± 0.07	0.62 ± 0.02
#1097	33.3 ± 0.7	32.9 ± 4.1	761.1 ± 7.6	9.78 ± 0.05	0.58 ± 0.0
#1098	34.4 ± 0.8	34.7 ± 4.2	764.6 ± 7.4	9.79 ± 0.06	0.17 ± 0.01
#1099	26.4 ± 0.8	24.5 ± 3.6	742.5 ± 8.5	9.72 ± 0.03	2.42 ± 0.01
#1100	35.2 ± 0.9	34.7 ± 3.7	770.4 ± 6.9	8.22 ± 0.02	0.92 ± 0.02
#1101	177.5 ± 4.3	176.2 ± 10.8	911.5 ± 7.4	5.96 ± 0.22	0.43 ± 0.07

9.3 Microscopic image analysis of W_f/W

This section documents the procedure to obtain the experimental fiber volume fraction (Φ_{V_f}), relative density (ρ_{rel}) and fiber positions.

9.3.1 Masking procedure

The applied image processing software was Adobe Photoshop CS6 [126].

Step 1: masking the pores and the ground's upper edge

1. The magic wand tool was used, with a tolerance of 80 and with "neighbored" activated, to roughly select the W CVD matrix.
2. The selection was enlarged so that the selection contour matched the white edge of the dark field capture, and inverted.
3. The filling tool was applied onto the selection of (2.), with "neighbored" deactivated, to mask all pores and the ground black (L = 0).
4. the filling tool was applied again on the ground with "neighbored" activated, to mask only the ground dark grey (L = 33). An example for the result can be seen in (Figure 9.1, b).

Step 2: masking the fibers

1. The dark field image was inverted and a levels filter for tonal adjustment applied to see the fibers better (Figure 9.1, c).
2. Light grey (L = 66) filled circles were placed manually at the fiber positions, while their alpha was set to 60 % (Figure 9.1, d).
3. The alpha was set back to 100 %.

Step 3: masking the CVD-W

- Since everything else was masked already, just a white layer had to be added as background (Figure 9.1, e).

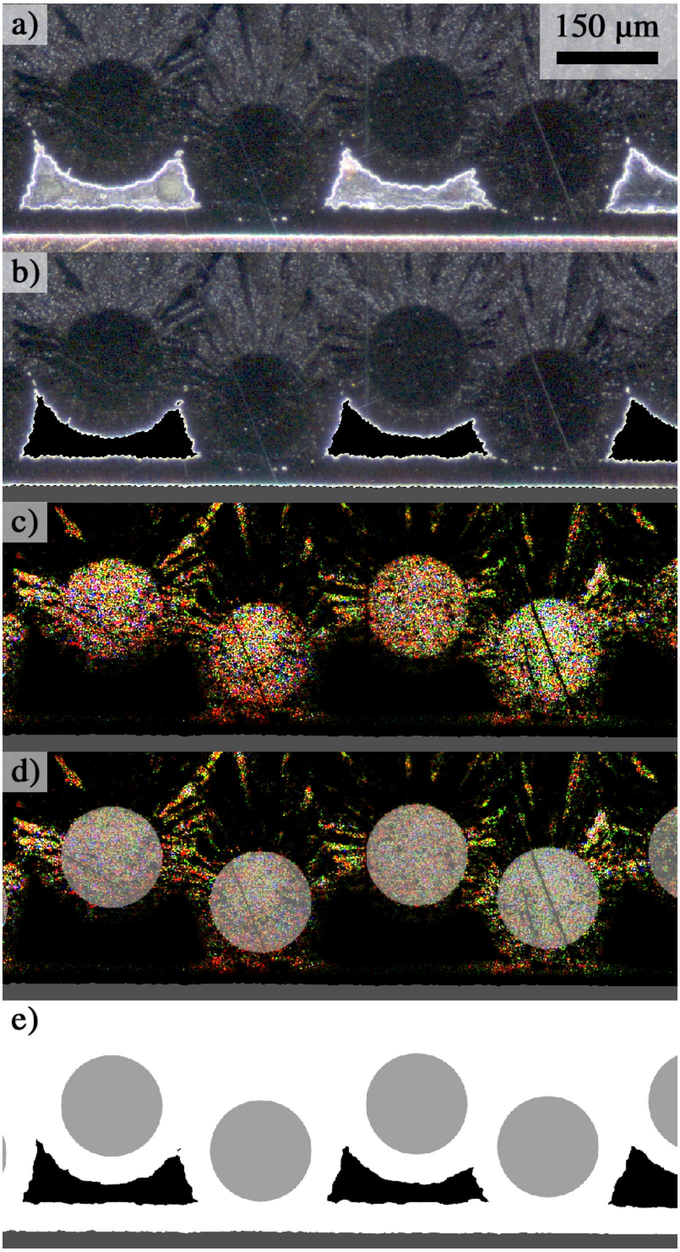

Figure 9.1: Part of the first layer of W_f/W produced by deposition of fabric 1. a) dark-field optical microscope image, b-d) masking steps for the pores, the ground, and the fibers, e) masking result used as input for the following Python script.

9.3.2 Python script and detailed results

In [1]:

```python
import numpy as np
import matplotlib.pyplot as plt
import pandas as pd
from scipy import ndimage

from skimage import io #to install skimage search for scikit-image
from skimage import data, color
from skimage.transform import hough_circle, hough_circle_peaks
from skimage.feature import canny
from skimage.draw import circle_perimeter
from skimage.util import img_as_ubyte

%config InlineBackend.figure_format = 'svg' # displaying as SVG (looks better)
```

Gather fiber middle point coordinates cx, cy

In [2]:

```python
#### CONFIG ###################
img_path = r"C:\Daten\Auswertung\wfw_layerwise\fabric 1 - 400\masked for python\400_a_rechts_masks.tif"
file_name = "400_a_rechts"

µm_to_pxl = 0.5052955

# Number of fibers
n = 91

# Radii that are searched
r_min = 149/2 #[µm]
r_max = 151/2 #[µm]
hough_radii = np.arange(int(round(r_min/µm_to_pxl,0)), int(round(r_max/µm_to_pxl,0))+1, 1)

# Masking legend
brightness_pore = 0
brightness_ground = 0.33
brightness_fiber = 0.66
brightness_W = 1
###############################

# Read image and convert to grayscale (2D array)
img_gray = io.imread(img_path, as_gray = True)

# Find edges (takes few minutes)
img_edges = canny(img_gray, sigma = 3)

# Detect circle
hough_res = hough_circle(img_edges, hough_radii)

# Select circles
accums, cx, cy, radii = hough_circle_peaks(hough_res, hough_radii, total_num_peaks = n)

# DataFrame for the center x- and y-coordinates
df_Posis = pd.DataFrame({'x':cx, 'y_f':cy, 'y_b':np.nan}).sort_values('x').reset_index(drop = True)

# Find y_bottom and fill into a data frame
for i, x_i in enumerate(df_Posis['x']):
    # start at y = image_height
    y = img_gray.shape[0] - 1
    #go up to W (white)
    while img_gray[y, x_i] < brightness_W:
        y -= 1
    df_Posis['y_b'].loc[i] = y + 1

# Plot fiber centers, y_bottom and pore numbers
fig = plt.figure(figsize=(100, 4))
ax = plt.subplot(111)
ax.plot(df_Posis['x'], df_Posis['y_f'], '+', c = 'r')
ax.plot(df_Posis['x'], df_Posis['y_b'], 'x', c = 'r')
for PoreID in np.arange(int((df_Posis.shape[0]-1)/2)):
    ax.text(df_Posis['x'][2*PoreID + 1] - 20, df_Posis['y_b'][2*PoreID] + 100, str(PoreID))

ax.imshow(img_gray[0:10000][:], cmap = plt.cm.gray)
```

```
Out[2]: <matplotlib.image.AxesImage at 0xbe1a208>
```

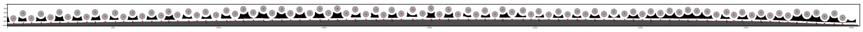

```
In [3]: df_Posis.head()
```

Out[3]:

	x	y_f	y_b
0	299	660	894.0
1	752	430	890.0
2	1148	653	879.0
3	1604	452	877.0
4	2062	611	864.0

Calculation of the rel. density and fiber vol. fraction

```
In [6]: def crop_halfPore(halfPoreID):
            '''
            crops the large image to the pore fraction below two neighbored fibers
            '''
            y_min = int((df_Posis['y_f'].loc[halfPoreID] + df_Posis['y_f'].loc[halfPoreID + 1])/2)
            y_max = int((df_Posis['y_b'].loc[halfPoreID] + df_Posis['y_b'].loc[halfPoreID + 1])/2)
            x_min = df_Posis['x'].loc[halfPoreID]
            x_max = df_Posis['x'].loc[halfPoreID + 1]

            img_halfPore = img_gray[y_min:y_max, x_min:x_max]
            return img_halfPore

        def calc_d_fh__V_shift(halfPoreID):
            # Vert dist between ground surface and lower fiber surface [µm]
            d_fh = µm_to_pxl*((df_Posis['y_b'].loc[halfPoreID] + df_Posis['y_b'].loc[halfPoreID + 1])/2
                              - max(df_Posis['y_f'].loc[halfPoreID],
                                df_Posis['y_f'].loc[halfPoreID + 1]) # lower fiber, max as origin is at top
                              - radii.mean())
            # Vertical dist between centers of two adjacent fibers [µm]
            v_shift = µm_to_pxl*abs(df_Posis['y_f'].loc[halfPoreID] - df_Posis['y_f'].loc[halfPoreID + 1])
            return d_fh,v_shift

        def calc_rel_density(PoreID,controll_area):
            halfPore_binary = (crop_halfPore(PoreID) > brightness_pore).astype(np.int)
            rel_dens = halfPore_binary.sum()/controll_area
            return rel_dens

        def calc_fiber_vol_frac(PoreID,controll_area):
            fiberParts_binary = (((brightness_ground + brightness_fiber)/2 < crop_halfPore(PoreID))
                                 & (crop_halfPore(PoreID) < (brightness_W + brightness_fiber)/2)).astype(np.int)
            fiber_vol_frac = fiberParts_binary.sum()/controll_area
            return fiber_vol_frac
```

Use the above methods in a for loop to fill a DataFrame

```
In [7]: df_halfPores = pd.DataFrame()

        for halfPoreID in np.arange(0, df_Posis.shape[0] - 1, 1):
            img_halfPore = crop_halfPore(halfPoreID)
            controll_area = (img_halfPore.shape[0]*img_halfPore.shape[1])

            single_df_row = {'halfPore#': halfPoreID,
                             'rel. Density': calc_rel_density(halfPoreID, controll_area),
                             'Fiber vol. frac.': calc_fiber_vol_frac(halfPoreID, controll_area),
                             'controll area [Pxl²]': controll_area,
                             # Horizontal dist between two adjacent fiber centers [µm]
                             'b_in_um': round(img_halfPore.shape[1]*µm_to_pxl, 1),
                             'd_fh_in_um': round(calc_d_fh__V_shift(halfPoreID)[0], 1),
                             'v_shift_in_um': round(calc_d_fh__V_shift(halfPoreID)[1], 1),
                            }
```

```
    df_halfPores = df_halfPores.append(pd.DataFrame.from_records([single_df_row],index = 'halfPore#'))
df_halfPores.head()
```

Out[7]:

halfPore#	rel. Density	Fiber vol. frac.	controll area [Pxl²]	b_in_um	d_fh_in_um	v_shift_in_um
0	0.785643	0.225007	157191	228.9	41.9	116.2
1	0.824131	0.259497	135828	200.1	41.7	112.7
2	0.801158	0.238685	148656	230.4	38.4	101.6
3	0.771915	0.227577	155262	231.4	55.8	80.3
4	0.726130	0.226502	156140	213.2	52.0	119.2

In [8]:

```
df_halfPores.std()
```

Out[8]:

```
rel. Density                0.080354
Fiber vol. frac.            0.033717
controll area [Pxl²]    24320.451160
b_in_um                    20.620216
d_fh_in_um                 24.538791
v_shift_in_um              25.031054
dtype: float64
```

Use above DataFrame to calculate values for "FullPores"

(between 3 neighbored fibers, fullpore/2 = halfpore for symmetric pores)

In [10]:

```
df_fullPores = pd.DataFrame()

def calc_for_fullPore(value_1,value_2,area_1,area_2):
    return  ((value_1 * area_1 + value_2 * area_2) / (area_1 + area_2))

fullPoreID = 0
for halfPoreID in np.arange(0, df_Posis.shape[0] - 2, 2):

    rel_density = calc_for_fullPore(df_halfPores['rel. Density'].loc[halfPoreID],
                                    df_halfPores['rel. Density'].loc[halfPoreID + 1],
                                    df_halfPores['controll area [Pxl²]'].loc[halfPoreID],
                                    df_halfPores['controll area [Pxl²]'].loc[halfPoreID + 1]
                                   )

    fiber_vol_frac = calc_for_fullPore(df_halfPores['Fiber vol. frac.'].loc[halfPoreID],
                                    df_halfPores['Fiber vol. frac.'].loc[halfPoreID + 1],
                                    df_halfPores['controll area [Pxl²]'].loc[halfPoreID],
                                    df_halfPores['controll area [Pxl²]'].loc[halfPoreID + 1]
                                   )

    # Add local position parameters to DataFrame, which can be also used as input for simulation
    x2 = df_Posis['x'].loc[halfPoreID + 1] - df_Posis['x'].loc[halfPoreID]
    x3 = df_Posis['x'].loc[halfPoreID + 2] - df_Posis['x'].loc[halfPoreID]

    y1 = df_Posis['y_b'].loc[halfPoreID] - df_Posis['y_f'].loc[halfPoreID]
    y2 = df_Posis['y_b'].loc[halfPoreID + 1] - df_Posis['y_f'].loc[halfPoreID + 1]
    y3 = df_Posis['y_b'].loc[halfPoreID + 2] - df_Posis['y_f'].loc[halfPoreID + 2]

    single_df_row = {'fullPore#': fullPoreID,
                     'rel. Density': rel_density,
                     'Fiber vol. frac.': fiber_vol_frac,
                     'halfPore_left#': halfPoreID,
                     'y1': y1*µm_to_pxl,
                     'x2': x2*µm_to_pxl,
                     'y2': y2*µm_to_pxl,
                     'x3': x3*µm_to_pxl,
                     'y3': y3*µm_to_pxl
                    }
```

```
    df_fullPores = df_fullPores.append(pd.DataFrame.from_records([single_df_row],index = 'fullPore#'))
    fullPoreID += 1

# Export for comsol
folder = r'P:\WILMA\Leonard Raumann\Comsol\2D growing interaction asym pore\Input'
df_fullPores.to_csv(folder + r'\posis_fullPores_' + file_name + '.txt', sep = '\t',
                    float_format = '%.1f', columns = ['x2','x3','y1','y2','y3'])

df_fullPores.head()
```

Out[10]:

	rel. Density	Fiber vol. frac.	halfPore_left#	y1	x2	y2	x3	y3
fullPore#								
0	0.803484	0.240995	0	118.239147	228.898862	232.435930	428.995880	114.196783
1	0.786219	0.233010	2	114.196783	230.414748	214.750587	461.840087	127.839762
2	0.734182	0.232645	4	127.839762	213.234701	246.078909	412.826424	129.860943
3	0.779179	0.227137	6	129.860943	227.888271	225.867088	449.712995	124.807989
4	0.798411	0.230827	8	124.807989	201.107609	231.930634	438.091199	125.818579

Implementation of Algorithm 4.1 (p. 80)

In [11]:

```
# Output: list pores that got experimentally filled sidewards further (but not yet in the simulation)
#         although top was sealed already

def calc_max_d_f(iPore):
    x2 = df_fullPores['x2'][iPore]
    x3 = df_fullPores['x3'][iPore]
    y1 = df_fullPores['y1'][iPore]
    y2 = df_fullPores['y2'][iPore]
    y3 = df_fullPores['y3'][iPore]

    d_f1f2 = (x2**2 + (y2 - y1)**2)**0.5
    d_f2f3 = ((x3 - x2)**2 + (y3 - y2)**2)**0.5

    return max(d_f1f2, d_f2f3) - 150

df_pore_analy = pd.DataFrame()

for iPore in range(43):
    max_d_g = max(df_fullPores['y1'][iPore], df_fullPores['y3'][iPore]) - 75
    filled_sidewards = 0
    if iPore != 0:
        if (calc_max_d_f(iPore) < calc_max_d_f(iPore - 1))\
        or (calc_max_d_f(iPore) < calc_max_d_f(iPore + 1)):
            if calc_max_d_f(iPore) < max_d_g:
                filled_sidewards = 1
                single_df_row = {'fullPore#': iPore,
                                 'max_d_f': calc_max_d_f(iPore),
                                 'max_d_g': max_d_g,
                                 'maybe_fed_from_side': filled_sidewards
                                 }
                df_pore_analy = df_pore_analy.append(pd.DataFrame.from_records([single_df_row],
                                                                                index = 'fullPore#'))
df_pore_analy.index
```

Out[11]:

```
Int64Index([12, 26, 35, 36, 37, 41], dtype='int64', name='fullPore#')
```

Table 9.4: For fabric #1 (cut "a"): Relative densities ρ_{rel} and fiber volume fractions Φ_{V_f} for single pores between three adjacent fibers and their center x, y coordinates.

Pore ID	Φ_{V_f}	ρ_{rel}	x_2 [µm]	x_3 [µm]	y_1 [µm]	y_2 [µm]	y_3 [µm]
0	0.24	0.80	228.90	429.00	118.24	232.44	114.20
1	0.23	0.79	230.41	461.84	114.20	214.75	127.84
2	0.23	0.73	213.23	412.83	127.84	246.08	129.86
3	0.23	0.78	227.89	449.71	129.86	225.87	124.81
4	0.23	0.80	201.11	438.09	124.81	231.93	125.82
5	0.25	0.86	244.06	441.63	125.82	211.72	115.21
6	0.24	0.80	216.27	451.23	115.21	207.68	125.31
7	0.24	0.79	222.33	451.23	125.31	208.18	133.90
8	0.25	0.75	178.87	391.10	133.90	228.39	148.56
9	0.21	0.86	264.27	465.38	148.56	224.86	137.44
10	0.23	0.84	209.70	459.82	137.44	212.22	135.92
11	0.20	0.81	249.11	454.77	135.92	240.52	160.68
12	0.19	0.69	198.08	434.05	160.68	266.29	188.48
13	0.17	0.71	244.06	451.23	188.48	277.91	170.79
14	0.19	0.68	228.90	438.09	170.79	261.24	162.71
15	0.19	0.74	219.30	467.40	162.71	251.13	162.20
16	0.19	0.73	238.50	441.12	162.20	260.73	163.72
17	0.20	0.68	214.75	429.00	163.72	266.80	151.08
18	0.20	0.83	215.26	469.92	151.08	243.55	130.37
19	0.24	0.82	242.54	424.45	130.37	236.98	111.17
20	0.24	0.78	194.03	421.92	111.17	224.86	135.92
21	0.19	0.87	275.89	509.84	135.92	235.47	140.47
22	0.23	0.74	201.11	404.24	140.47	264.27	119.25
23	0.23	0.78	216.27	442.64	119.25	231.93	118.24
24	0.25	0.88	246.58	436.07	118.24	220.31	115.21
25	0.24	0.84	208.69	449.71	115.21	209.19	120.77
26	0.23	0.76	181.91	408.28	120.77	233.95	175.34
27	0.22	0.84	262.25	454.77	175.34	211.72	119.25
28	0.28	0.89	183.93	424.45	119.25	192.01	114.70
29	0.26	0.83	230.92	452.74	114.70	187.46	120.26
30	0.27	0.86	230.92	426.47	120.26	191.51	128.85
31	0.25	0.79	224.35	444.15	128.85	199.09	132.89
32	0.23	0.88	235.47	489.63	132.89	187.46	144.01
33	0.25	0.75	209.70	426.97	144.01	192.52	138.96
34	0.23	0.74	201.61	434.55	138.96	202.62	166.24
35	0.20	0.66	219.30	449.71	166.24	216.77	187.46
36	0.19	0.63	206.16	419.90	187.46	240.02	220.31
37	0.19	0.70	251.13	469.42	220.31	210.71	139.97
38	0.25	0.84	243.55	419.40	139.97	206.67	139.46
39	0.24	0.80	198.08	430.01	139.46	203.63	138.96
40	0.25	0.76	218.29	437.08	138.96	198.08	137.95
41	0.24	0.74	217.28	425.96	137.95	200.10	156.64
42	0.18	0.63	215.26	455.78	156.64	250.63	204.64
43	0.19	0.61	225.87	421.42	204.64	252.14	166.75
44	0.20	0.68	233.95	429.00	166.75	250.63	151.08

9.4 Python script for the thermal diffusion coefficient

In [1]:

```
#Version 1.4
import numpy as np
import pandas as pd
import time
```

In [2]:

```
###=== INPUT DATA =======###
dfAllPolys = pd.read_excel('C:/Daten/Modeling/Stoffdaten/Polynomals_for_T_star_related_quantities.xlsx')

R_const = 8.31446 #[J mol^-1 K^-1]
speciesData={0:{'species':'H_2',
                'molar mass [kg/mol]':0.00201588,
                '(epsilon/k_B)[K]':lambda T:59.7,
                'sigma[m]':lambda T:2.827E-10,
               },
             1:{'species':'WF_6',
                'molar mass [kg/mol]':0.297830419,
                '(epsilon/k_B)[K]': lambda T:(819.92 -1.0619*T + 0.000619*T**2 - (6.62E-8)*T**3),
                'sigma[m]': lambda T:(4.9734 + 0.0009284*T + 6.5815E-7*T**2 - (7.315E-10)*T**3)*10**-10,
               },
             2:{'species':'HF',
                'molar mass [kg/mol]':0.020006,
                '(epsilon/k_B)[K]':lambda T:330,
                'sigma[m]':lambda T:3.148E-10,
               },}
'''
2:{'species':'SiH_4',
   'molar mass [kg/mol]':0.03212,
   '(epsilon/k_B)[K]':lambda T:207.6,
   'sigma[m]':lambda T:4.084E-10,
  },
'''
#references: polynomals Kleijn1991, p. 37; other data as in Table 8.1 in present dissertation
###======================###

#number of species:
N = len(speciesData)
#zip molar masses:
m_={}
for key in speciesData: m_[key] = speciesData[key]['molar mass [kg/mol]']

def create_T_dep_Dicts(T):
    '''returns T dependent literature data as compact indexed dictionaries for use in formulas;
    this has to be executed in the beginning of the T loop, which will fill the look up table,
    to provide the function calc_Md_and_detMd with needed T dependent local variables'''
    sigma_, epsilonDivKb_ = {}, {}
    for k in range(N): sigma_[k]=speciesData[k]['sigma[m]'](T)
    for k in range(N): epsilonDivKb_[k]=speciesData[k]['(epsilon/k_B)[K]'](T)
    return sigma_, epsilonDivKb_

def getQuantityValue(Quantity,T_star):
    '''
    returns value for requested Quantity (Omega_i or A*-C*)
    looks up the polynomals in table 2.5 in [Kleijn1993] depending on T_star.
    '''
    dfPolys = dfAllPolys.query('Quantity == @Quantity and T_star_low <= @T_star < T_star_high')
    return float(dfPolys['a0']+dfPolys['a1']*T_star+dfPolys['a2']*T_star**2+dfPolys['a3']*T_star**3)

def calc_Md_and_detMd(T,f_):
    '''
    returns the matrix in the denominator in the equation for D_T [Kleijn1993, Eq. 2.89] and its determinant
    needs the for loop variables T, f_ as input
    needs m_, sigma_, epsilonDivKb_, c_p_ as lokal variables
    '''
    #following lambda is an unnamed python function not to be confused with thermal conductivity
    sigma = lambda i,j: 0.5*(sigma_[i]+sigma_[j]) #[m] [Eq. 2.69]
    epsilonDivKb = lambda i,j: (epsilonDivKb_[i]*epsilonDivKb_[j])**0.5 #[K] [Eq. 2.70]
    T_star = lambda i,j: T/epsilonDivKb(i,j) #[-] [Eq. 2.71]
```

```
    Omega_mu = lambda i,j: getQuantityValue('Omega_mu',T_star(i,j))
    Omega_D  = lambda i,j: getQuantityValue('Omega_D',T_star(i,j))
    A_star   = lambda i,j: getQuantityValue('A_star',T_star(i,j))
    B_star   = lambda i,j: getQuantityValue('B_star',T_star(i,j))
    C_star   = lambda i,j: getQuantityValue('C_star',T_star(i,j))

    #to obtain lamb (thermal heat conductivity in W/(m*K) [p.43, Eq. 2.80 = 2.81 for i = j)]:
    lamb = lambda i,j: (0.00263*(T*(m_[i]+m_[j])/(2*m_[i]*m_[j]))**0.5
                        /((sigma(i,j)*1E10)**2*Omega_mu(i,j))) #(K/kg*mol)**0.5/m²...units does not fit,
                                                               #but final result fit to Fig 2.5 with this

    def L_00(i,j): #[Eq. 2.90 and 2.91]
        result=0.
        if i!=j:
            result=2.*f_[i]*f_[j]/(A_star(i,j)*lamb(i,j))
            for n in range(N):
                if n!=i:
                    result+=2.*f_[j]*f_[n]*m_[j]/(m_[i]*A_star(i,n)*lamb(i,n))
                    # the f_[j] is correct compared to Hirschfelder1967
                    # with f_[i] as in the book of Kleijn, its not possible to reproduce Fig 2.5
        return result


    def L_01(i,j):
        result=0.
        if i==j:
            for n in range(N):
                if n!=i:
                    result+=(5.*f_[i]*f_[n]*m_[n]*(6./5.*C_star(i,n)-1)
                             /((m_[i]+m_[n])*A_star(i,n)*lamb(i,n)))
        if i!=j:
            result=(-5.*f_[i]*f_[j]*m_[i]*(6./5.*C_star(i,j)-1.)
                    /((m_[i]+m_[j])*A_star(i,j)*lamb(i,j)))
        return result

    def L_10(i,j): return m_[j]/m_[i]*L_01(i,j)

    def L_11(i,j):
        result=0.
        if i==j:
            result=-4.*f_[i]**2/lamb(i,j)
            for n in range(N):
                if n!=i:
                    result-=(2.*f_[i]*f_[n]*(15./2.*m_[i]**2+25./4.*m_[n]**2
                                             -3.*m_[n]**2*B_star(i,n)
                                             +4.*m_[i]*m_[n]*A_star(i,n))
                             /((m_[i]+m_[n])**2*A_star(i,n)*lamb(i,n)))
        if i!=j:
            result=(2*f_[i]*f_[j]*m_[i]*m_[j]/((m_[i]+m_[j])**2*A_star(i,j)*lamb(i,j))
                    *(55./4.-3.*B_star(i,j)-4.*A_star(i,j)))
        return result

    #filling of the matrix according to gas species i,j,
    #which start here at zero and not with one as in the book,
    #as matrix indizes and range(...) also starts at zero

    Md = np.zeros((2*N,2*N)) # matrix in denominator in Eq. 2.89
    for i in range(N): #i,j=0,1,2,... #i=row, j=column
        for j in range(N):
            Md[i,j]     = L_00(i,j)
            Md[i,j+N]   = L_01(i,j)
            Md[i+N,j]   = L_10(i,j)
            Md[i+N,j+N] = L_11(i,j)
    return Md, np.linalg.det(Md) #so that det(Md) needs to be calculated only once for all k

def kroneckerDelta(i,j):  #carefull: np.kron(i,j) is something else
    if i == j: return 1.
    else: return 0.
```

```
def calc_D_T(Md, detMd, k, f_):
    '''
    Returns thermal diffusion coefficients for different species k, which do share the same Md and detMd.
    '''
    Mc = np.zeros((2*N+1, 2*N+1))# matrix in counter
    Mc[:-1,:-1] = Md
    for j in range(N):
        Mc[N+j, 2*N] = f_[j] #last column (index start at 0, thus column 2*N e.g.=6 is the 7. column)
        Mc[2*N, j]   = f_[j]*kroneckerDelta(j,k) #last row
    return -8*m_[k]/5/R_const*np.linalg.det(Mc)/detMd

######## build look-up-dataframe for D_T(k): #######
df_D = pd.DataFrame()

###=== T & molefractions loop CONFIG =======###
T_loop   = np.linspace(300,1100,18)
f_0_loop = np.linspace(1e-6,1-1e-6,11)
f_0 = f_0_loop[0] #will be replaced by other is elements of f_0_loop during following nested for-loops
f_1_loop = [1e-6,1e-2]+np.logspace(-1.6,-0.07,12).tolist()+[1-f_0]

t0 = time.clock()
for T in T_loop:
    sigma_,epsilonDivKb_= create_T_dep_Dicts(T)
    for f_0 in f_0_loop:
        for f_1 in f_1_loop:
            if f_0 > 0 and f_1 > 0 and f_0+f_1 < 1:
                f_=[f_0, f_1, 1-f_0-f_1]
                Md,detMd = calc_Md_and_detMd(T,f_)
                single_row = {'$T$ [K]':T}
                for k in range(N):
                    single_row['$x('+speciesData[k]['species']+')$'] = f_[k]
                    single_row['$D_T('+speciesData[k]['species']+')$ [kg/(m*s)]'] = calc_D_T(Md,detMd,k,f_)
                df_D = df_D.append(pd.DataFrame.from_records([single_row]),sort = False)

neededTime = time.clock() - t 0
df_D.head()
```

Out[2]:

	T [K]	$x(H_2)$	$D_T(H_2)$ [kg/(m*s)]	$x(WF_6)$	$D_T(WF_6)$ [kg/(m*s)]	$x(HF)$	$D_T(HF)$ [kg/(m*s)]
0	300.0	0.000001	-8.608532e-13	0.000001	-7.895946e-12	0.999998	8.756800e-12
0	300.0	0.000001	-8.396021e-13	0.010000	-6.721363e-08	0.989999	6.721447e-08
0	300.0	0.000001	-8.114028e-13	0.025119	-1.361034e-07	0.974880	1.361042e-07
0	300.0	0.000001	-7.954698e-13	0.034601	-1.659782e-07	0.965398	1.659790e-07
0	300.0	0.000001	-7.751778e-13	0.047663	-1.958734e-07	0.952336	1.958741e-07

In [3]:

```
print('needed time: ' + '%.1f'%(neededTime/60) + ' min')
```

```
needed time: 26.9 min
```

In [4]:

```
# ==== EXPORT for Comsol ==============

fillingUpSpecies = 2 #the species that fills up the mole fraction to 1
                     #and is thus not needed as argument

myColumnOrder = ['$T$ [K]']
for k in range (N):
    if k != fillingUpSpecies:
        myColumnOrder += df_D.filter(like='x')\
                        .filter(like=speciesData[k]['species']).columns.tolist()
for k in range (N):
    myColumnOrder += df_D.filter(like='D_T')\
                    .filter(like=speciesData[k]['species']).columns.tolist()

destiFile = r'P:\WILMA\Leonard Raumann\Comsol\single fiber tube\input data\D_T.txt'
df_D[myColumnOrder].to_csv(destiFile,index=False, sep='\t', float_format='%1.2e',)
df_D[myColumnOrder].head()
```

Out[4]:

	T [K]	$x(H_2)$	$x(WF_6)$	$D_T(H_2)$ [kg/(m*s)]	$D_T(WF_6)$ [kg/(m*s)]	$D_T(HF)$ [kg/(m*s)]
0	300.0	0.000001	0.000001	-8.608532e-13	-7.895946e-12	8.756800e-12
0	300.0	0.000001	0.010000	-8.396021e-13	-6.721363e-08	6.721447e-08
0	300.0	0.000001	0.025119	-8.114028e-13	-1.361034e-07	1.361042e-07

9.5 Python script for theoretical Φ_{V_f} and ρ_{rel} as function of fiber positions (uniform growth)

In [1]:

```
import numpy as np
import pandas as pd
```

Calculation: Fiber volume fraction & Relative Density

In [2]:

```
### Parameters ##########################

# warp fiber radius:
r_wa = 75 #[µm],
# horizontal distance between surfaces of fiber 1 (left) and fiber 2 (right):
dh_f1s_f2s = np.linspace(0,240,500) #[µm],
# vertical distance between the ground surface and the surfaces of the lower fiber (here fiber 1):
d_gs_f1s = np.linspace(0,140,int(500*140/200)) #[µm],
# vertical distance between the lower and higher fiber:
vertical_displ = np.linspace(0,140,3) #[µm]

def calc_fiber_vol_frac(r_wa, dh_f1s_f2s, d_gs_f1s, vertical_displ):
    # fiber
    fiber_area = 0.5*np.pi * r_wa**2 #[µm²]
    # horizontal distance between the fiber centers:
    b = dh_f1s_f2s + 2 * r_wa #[µm]
    # area, in which the fiber volume fraction is calculated
    controll_area = b * (r_wa + d_gs_f1s + vertical_displ/2) #[µm²]
    # fiber volume fraction:
    fiber_vol_frac = fiber_area / controll_area #[-]
    return fiber_vol_frac

def calc_rel_density(r_wa, dh_f1s_f2s, d_gs_f1s, vertical_displ):
    # distance between surfaces of ground and higher fiber
    d_gs_f2s = d_gs_f1s + vertical_displ #[µm],
    # horizontal distance between the the fiber centers
    b = dh_f1s_f2s + 2 * r_wa #[µm],
    # distance between surfaces of fiber 1 (left) and fiber 2 (right):
    d_f1s_f2s = (b**2 + vertical_displ**2)**0.5 - 2 * r_wa
    # radius until "CVD surface-to-surface contact" for uniform growth
    r_grown = r_wa + d_f1s_f2s/2
    # area, in which the relative density is calculated
    controll_area = b * (r_wa + d_gs_f1s + vertical_displ/2) #[µm²]

    # part of the radius "h", for which the circle (fiber) overlaps with the ground,
    h1 = d_f1s_f2s - d_gs_f1s
    h2 = d_f1s_f2s - d_gs_f2s

    def calc_A(h):
        '''
        to calculate the part of the left or right fiber area (A/2) that needs to be removed
        see https://de.wikipedia.org/wiki/Kreissegment
        '''
        if isinstance(h, int) or isinstance(h, float):
            if h < 0: h = 0
        else: #numpy array:
            h[h < 0] = 0

        A = r_grown**2 * np.arccos(1 - h/r_grown) - (r_grown - h) * (2*r_grown*h - h**2)**0.5
        return A

    # solid area = grown fiber area - overlap + grown ground area
    solid_area = np.pi/2 * r_grown**2 - (calc_A(h1) + calc_A(h2))/2 + b*d_f1s_f2s/2

    rel_density = solid_area / controll_area

    return rel_density
```

Contour plots

In [3]:

```
import matplotlib.pyplot as plt
from   matplotlib.ticker import (MultipleLocator, FormatStrFormatter, AutoMinorLocator)
from   matplotlib.colors import ListedColormap
```

In [4]:

```
def contourPlot(vertical_displ = 0, markers_x = [], markers_y = []):

    fig, ax = plt.subplots(1,1)

    ### Plot labeling and settings #########################
    ax.set_title('$Y^{´}_{\!\!ff}$ = ' + str(vertical_displ) + ' µm', fontsize = 12)
    ax.set_xlabel('$X_{ff}$ [µm]')
    ax.set_ylabel('$Y_{fg}$ [µm]')

    # grid and ticks
    ax.grid(alpha = 0.4)
    ax.set_xlim(0, 245)
    ax.set_xticks(np.arange(0, 260, 20).tolist())

    ax.xaxis.set_minor_locator(MultipleLocator(4))
    ax.yaxis.set_minor_locator(MultipleLocator(4))

    # rel. density and fiber vol. fraction labels
    ax.text(160, 130 - vertical_displ/2, r'$\rho_{rel}$', color = 'g',
            backgroundcolor = 'w', fontsize = 14)
    ax.text(90, 130 - vertical_displ/2, r'$\Phi_{V_f}$', color = 'b',
        backgroundcolor = 'w', fontsize = 14)
    ########################################################

    # for manual contour label positions:
    def getLabelPosis(x1, x2, y1, y2, n = 6):
        y1b = y1 + 8 - 0.42*vertical_displ
        y2b = y2 + 8 - 0.42*vertical_displ
        m = (y2b - y1b) / (x2 - x1)
        b = y2b - x2*(y2b - y1b) / (x2 - x1)
        f = lambda x: m*x + b

        x = np.linspace(x1, x2, n)
        result = []
        for i in range(n):
            result += [(x[i], f(x[i]))]
        return result
    # slice contour plot color map
    def sliceCmap(cmap_name, lo = 0.5, hi = 0.9):
        cmap = plt.cm.get_cmap(cmap_name, 512)
        return ListedColormap(cmap(np.linspace(lo, hi, 256)))

    x = dh_f1s_f2s
    y = d_gs_f1s
    X, Y = np.meshgrid(x, y)

    # cotour plot for rel. density
    Z = calc_rel_density(r_wa, X, Y, vertical_displ)
    rel_dens_levels=[0.97,0.98,0.99,0.996,0.999,1]
    CS = plt.contour(X, Y, Z, levels=rel_dens_levels, linewidths = 2, cmap = sliceCmap('Greens'))
    label_x_pos = 200
    ax.clabel(CS, inline=1, fontsize=11,
              manual = getLabelPosis(x1 = 205, x2 = 215, y1 = 120, y2 = 25, n = len(rel_dens_levels)))

    # cotour plot for fiber vol. fraction
    Z = calc_fiber_vol_frac(r_wa, X, Y, vertical_displ)
    f_frac_levels = [0.2,0.25,0.30,0.35]
    CS = plt.contour(X, Y, Z, levels= f_frac_levels, linewidths = 2, cmap = sliceCmap('Blues'))
    label_x_pos = 30
    ax.clabel(CS, inline=1, fontsize=11,
              manual = getLabelPosis(x1 = 20, x2 = 60, y1 = 60, y2 = 125, n = len(f_frac_levels)))
```

```
    # xy marker lines
    marker_colors = ['r', 'orange']
    for i in range(len(markers_x)):
        ax.plot((0, markers_x[i]),(markers_y[i], markers_y[i]), color = marker_colors[i], zorder = -1)
        ax.plot((markers_x[i], markers_x[i]),(0, markers_y[i]), color = marker_colors[i], zorder = -1)
```

```
In [5]: contourPlot(vertical_displ = 27, markers_x = [], markers_y = [])
```

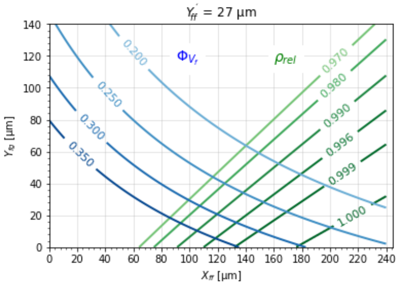

```
In [6]: contourPlot(vertical_displ = 25, markers_x = [125,210], markers_y = [40,64])
```

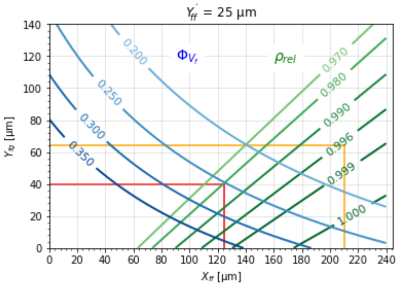

List of Figures

List of Tables

Bibliography

[1] L. Raumann, J. Coenen, J. Riesch, Y. Mao, H. Gietl, T. Höschen, Ch. Linsmeier, O. Guillon, Modeling and validation of chemical vapor deposition of tungsten for tungsten fiber reinforced tungsten composites, Surface and Coatings Technology 381 (2020) 124745.

[2] C. Buchal, Course 5 of the Joint EPS-SIF International School on Energy "Energy: Where we stand and where we go" 22 - 27 July 2019 - VILLA MONASTERO - VARENNA, LAKE COMO, EPJ Web of Conferences, 2020, Chapt. The Challenge of Discussing Energy Facts and Climate Change.

[3] Y. Kim, M. Kim, W. Kim, Effect of the Fukushima nuclear disaster on global public acceptance of nuclear energy, Energy Policy 61 (2013) 822–828.

[4] A. Brunnengräber, Das wicked problem der Endlagerung Zehn Charakteristika des komplexen Umgangs mit hochradioaktiven Reststoffen, Nomos Verlagsgesellschaft mbH & Co. KG, Baden-Baden, 2016.

[5] K. Stierstadt, G. Fischer, Radioactive waste-wherever to remove?, 2nd Edition, Wissenschaftlicher Verlag Harri Deutsch GmbH, Frankfurt am Main, 2011.

[6] N. Ruiz, I. Cobelo, J. Oyarzabal, A direct load control model for virtual power plant management, IEEE Transactions on Power Systems 24 (2) (2009) 959–966.

[7] T. S. Reshid, Study of some structural fusion materials for (n, 2n) reactions, Journal of Fusion Energy 34 (4) (2015) 746–750.

[8] F. Romanelli, Fusion Electricity a roadmap to the realisation of fusion energy, European Fusion Development Agreement, EFDA, 2012, ISBN 978-3-00-040720-8.

[9] G. Federici, G. Giruzzi, C. Lowry, R. Kemp, D. Ward, R. Wenninger, H. Zohm, EU DEMO design and R&D studies, in: Fusion Engineering (SOFT), 2013 IEEE 25th Symposium on Fusion Technology, 2013, pp. 1–8.

[10] H. Zohm, Assessment of DEMO challenges in technology and physics, Fusion Engineering and Design 88 (6-8) (2013) 428–433.

[11] R. Wenninger, M. Bernert, T. Eich, E. Fable, G. Federici, A. Kallenbach, A. Loarte, C. Lowry, D. McDonald, R. Neu, T. Pütterich, P. Schneider, B. Sieglin, G. Strohmayer, F. Reimold, M. Wischmeier, DEMO divertor limitations during and in between ELMs, Nuclear Fusion 54 (11) (2014) 114003.

[12] N. Baluc, Materials for fusion power reactors, Plasma Physics and Controlled Fusion 48 (12B) (2006) B165–B177.

[13] Ch. Linsmeier, M. Rieth, J. Aktaa, T. Chikada, A. Hoffmann, J. Hoffmann, A. Houben, H. Kurishita, X. Jin, M. Li, A. Litnovsky, S. Matsuo, A. von Müller, V. Nikolic, T. Palacios, R. Pippan, D. Qu, J. Reiser, J. Riesch, T. Shikama, R. Stieglitz, T. Weber, S. Wurster, J.-H. You, Z. Zhou, Development of advanced high heat flux and plasma-facing materials, Nuclear Fusion 57 (9) (2017) 092007.

[14] E. Lassner, W.-D. Schubert, Tungsten - Properties, Chemistry, Technology of the Element, Alloys, and Chemical Compound, Springer, 1999.

[15] J. Reiser, M. Rieth, B. Dafferner, A. Hoffmann, Charpy impact properties of pure tungsten plate material in as-received and recrystallized condition, Journal of Nuclear Materials 442 (2013) 204–207.

[16] J. W. Coenen, S. Antusch, M. Aumann, W. Biel, J. Du, J. Engels, S. Heuer, A. Houben, T. Hoeschen, B. Jasper, et al., Materials for DEMO and reactor applications – boundary conditions and new concepts, Physica Scripta 2016 (T167).

[17] J. Riesch, M. Aumann, J. W. Coenen, H. Gietl, G. Holzner, T. Höschen, P. Huber, M. Li, Ch. Linsmeier, R. Neu, Chemically deposited tungsten fibre-reinforced tungsten - The way to a mock-up for divertor applications, Nuclear Materials and Energy (2016) –ICFRM Conference 2015.

[18] History of fusion, official EUROfusion web-page. URL: https://www.euro-fusion.org/fusion/history-of-fusion/.

[19] U. Schumacher, Status and problems of fusion reactor development, Naturwissenschaften 88 (3) (2001) 102–112.

[20] W. M. Stacey, Fusion, WILEY-VCH Verlag GmbH & Co. KGaA, Weinheim, 2010.

[21] T. Klinger, T. Andreeva, S. Bozhenkov et al., Overview of first Wendelstein 7-X high-performance operation, Nuclear Fusion 59 (11).

[22] D. Stork, P. Agostini, J. Boutard, D. Buckthorpe, E. Diegele, S. Dudarev, C. English, G. Federici, M. Gilbert, S. Gonzalez, A. Ibarra, Ch. Linsmeier, A. Puma, G. Marbach, P. Morris, L. Packer, B. Raj, M. Rieth, M. Tran, D. Ward, S. Zinkle,

Developing structural, high-heat flux and plasma facing materials for a near-term DEMO fusion power plant: The EU assessment, Journal of Nuclear Materials 455 (2014) 277 – 291.

[23] D. Stork, P. Agostini, J. Boutard, D. Buckthorpe, E. Diegele, S. Dudarev, C. English, G. Federici, M. Gilbert, S. Gonzalez, A. Ibarra, Ch. Linsmeier, A. Puma, G. Marbach, P. Morris, L. Packer, B. Raj, M. Rieth, M. Tran, D. Ward, S. Zinkle, Materials R&D for a timely DEMO: Key findings and recommendationsof the EU Roadmap Materials Assessment Group, Fusion Engineering and Design 89 (2014) 1586 – 1594.

[24] J.-H. You, E. Visca, C. Bachmann, T. Barrett, F. Crescenzi, M. Fursdon, H. Greuner, D. Guilhem, P. Languille, M. Li, S. McIntosh, A. Müller, J. Reiser, M. Richou, M. Rieth, European DEMO divertor target: Operational requirements and material-design interface, Nuclear Materials and Energy 9 (2016) 171 – 176.

[25] J.-H. You, G. Mazzone, E. Visca, C. Bachmann, E. Autissier, T. Barrett, V. Cocilovo, F. Crescenzi, P. Domalapally, D. Dongiovanni, S. Entler, G. Federici, P. Frosi, M. Fursdon, H. Greuner, D. Hancock, D. Marzullo, S. McIntosh, A. Müller, M. Porfiri, G. Ramogida, J. Reiser, M. Richou, M. Rieth, A. Rydzy, R. Villari, V. Widak, Conceptual design studies for the European DEMO divertor: Rationale and first results, Fusion Engineering and Design 109 (2016) 1598 – 1603.

[26] H. Bolt, V. Barabash, G. Federici, J. Linke, A. Loarte, J. Roth, K. Sato, Plasma facing and high heat flux materials – needs for ITER and beyond, Journal of Nuclear Materials 307-311 (1) (2002) 43–52.

[27] Collage from images of the official ITER web-page, URL: https://www.iter.org/album/Media/7

[28] W. Yih, C. Wang, Tungsten: Sources, Metallurgy, Properties, and Applications, Springer US, 1979.

[29] T. Hirai, F. Escourbiac, S. Carpentier-Chouchana, A. Fedosov, L. Ferrand, T. Jokinen, V. Komarov, A. Kukushkin, M. Merola, R. Mitteau, R. Pitts, W. Shu, M. Sugihara, B. Riccard, S. Suzuki, R. Villarid, ITER tungsten divertor design development and qualification program, Fusion Engineering and Design (88) (2013) 1798–1801.

[30] G. Pintsuk, I. Bobin-Vastra, S. Constans, P. Gavila, M. Rödig, B. Riccardi, Qualification and post-mortem characterization of tungsten mock-ups exposed to cyclic high heat flux loading, Fusion Engineering and Design 88 (9–10) (2013) 1858 –

1861, proceedings of the 27th Symposium On Fusion Technology (SOFT-27); Liège, Belgium, September 24-28, 2012.

[31] S. Zinkle, N. Ghoniem, Operating temperature windows for fusion reactor structural materials, Fusion Engineering and Design 51-52 (0) (2000) 55–71.

[32] W. Timmis, Material assessment report on the use of copper alloys in DEMO, Technical Report, Culham Centre for Fusion Energy.

[33] C. Bonnekoh, U. Jäntsch, J. Hoffmann, H. Leiste, A. Hartmaier, D. Weygand, A. Hoffmann, J. Reiser, The brittle-to-ductile transition in cold rolled tungsten plates: Impact of crystallographic texture, grain size and dislocation density on the transition temperature, International Journal of Refractory Metals and Hard Materials 78 (2019) 146–163.

[34] A. Giannattasio, Z. Yao, E. Tarleton, S. Roberts, Brittle–ductile transitions in polycrystalline tungsten, Philosophical Magazine 90 (30) (2010) 3947–3959.

[35] M. Fukuda, K. Yabuuchi, S. Nogami, A. Hasegawa, T. Tanaka, Microstructural development of tungsten and tungsten–rhenium alloys due to neutron irradiation in HFIR, Journal of Nuclear Materials 455 (1-3) (2014) 460–463.

[36] A. Hasegawa, M. Fukuda, S. Nogami, K. Yabuuchi, Neutron irradiation effects on tungsten materials, Fusion Engineering and Design 89 (7-8) (2014) 1568–1572.

[37] X. Hu, T. Koyanagi, M. Fukuda, N. K. Kumar, L. L. Snead, B. D. Wirth, Y. Katoh, Irradiation hardening of pure tungsten exposed to neutron irradiation, Journal of Nuclear Materials 480 (2016) 235–243.

[38] M. Gilbert, J.-C. Sublet, Neutron-induced transmutation effects in W and W-alloys in a fusion environment, Nuclear Fusion 51 (4) (2011) 043005.

[39] M. Gilbert, S. Dudarev, D. Nguyen-Manh, S. Zheng, L. Packer, J.-C. Sublet, Neutron-induced dpa, transmutations, gas production, and helium embrittlement of fusion materials, Journal of Nuclear Materials 442 (1-3) (2013) 755–760.

[40] T. Hwang, M. Fukuda, S. Nogami, A. Hasegawa, H. Usami, K. Yabuuchi, K. Ozawa, H. Tanigawa, Effect of self-ion irradiation on hardening and microstructure of tungsten, Nuclear Materials and Energy 9 (2016) 430–435.

[41] T. Loewenhoff, J. Linke, G. Pintsuk, C. Thomser, Tungsten and CFC degradation under combined high cycle transient and steady state heat loads, Fusion Engineering and Design 87 (7-8) (2012) 1201–1205.

[42] B. Jasper, Einzelfaserkomposite aus Pulvermetallurgischem Wolframfaserverstärktem Wolfram, Ph.D. thesis, Ruhr-Universität Bochum (2017).

[43] K. K. Chawla, Ceramic Matrix Composites, 2nd Edition, Springer US, New York, 2003.

[44] J. Du, A Feasibility Study of Tungsten-Fiber-Reinforced Tungsten Composites with Engineered interfaces, PhD thesis, Technische Universität München (2010).

[45] W. Curtin, Multiple matrix cracking in brittle matrix composites, Acta Metallurgica et Materialia 41 (5) (1993) 1369–1377.

[46] A. Evans, M.-Y. He, J. Hutchinson, Interface debonding and fiber cracking in brittle matrix composites, Journal of the American Ceramic Society 72 (12) (1989) 2300–2303.

[47] A. Evans, F. Zok, J. Davis, The role of interfaces in fiber-reinforced brittle matrix composites, Composites Science and Technology 42 (1991) 3–24.

[48] J. Riesch, Entwicklung und Charakterisierung eines wolframfaserverstärkten Wolfram-Verbundwerkstoffs, PhD thesis, Technische Universität München (2012).

[49] J. Riesch, J.-Y. Buffiere, T. Höschen, M. di Michiel, M. Scheel, Ch. Linsmeier, J.-H. You, In situ synchrotron tomography estimation of toughening effect by semi-ductile fibre reinforcement in a tungsten-fibre-reinforced tungsten composite system, Acta Materialia 61 (19) (2013) 7060–7071.

[50] J. Riesch, T. Hoeschen, Ch. Linsmeier, S. Wurster, J.-H. You, Enhanced toughness and stable crack propagation in a novel tungsten fibre-reinforced tungsten composite produced by chemical vapour infiltration, Physica Scripta 2014 (T159) (2014) 014031.

[51] R. Neu, J. Riesch, J. Coenen, J. Brinkmann, A. Calvo, S. Elgeti, C. Garcia-Rosales, H. Greuner, T. Höschen, G. Holzner, F. Klein, F. Koch, Ch. Linsmeier, A. Litnovsky, T. Wegener, S. Wurster, J.-H. You, Advanced tungsten materials for plasma-facing components of DEMO and fusion power plants, Fusion Engineering and Design 109-111: Part A (2016) 1046–1052.

[52] R. Neu, J. Riesch, A. Müller, M. Balden, J. Coenen, H. Gietl, T. Höschen, M. Li, S. Wurster, J.-H. You, Tungsten fibre-reinforced composites for advanced plasma facing components, Nuclear Materials and Energy 12 (2016) 1308–1313.

[53] J. Riesch, Y. Han, J. Almanstötter, J. W. Coenen, T. Höschen, B. Jasper, P. Zhao, Ch. Linsmeier, R. Neu, Development of tungsten fibre-reinforced tungsten composites towards their use in DEMO - potassium doped tungsten wire, Physica Scripta 2016 (T167) (2016) 014006.

[54] H. Gietl, Weiterentwicklung von wolframfaserverstfärktem Wolframverbundwerkstoff für den Einsatz in der Fusion, PhD thesis, Technische Universität München (2018).

[55] B. Jasper, J. W. Coenen, J. Riesch, T. Höschen, M. Bram, Ch. Linsmeier, Powder Metallurgical Tungsten Fiber-Reinforced Tungsten, Material Science Forum, Trans Tech Publications 825-826 (2015) 125–133.

[56] B. Jasper, S. Schönen, J. Du, T. Höschen, F. Koch, Ch. Linsmeier, R. Neu, J. Riesch, A. Terra, J. Coenen, Behavior of tungsten fiber-reinforced tungsten based on single fiber push-out study, Nuclear Materials and Energy 9 (2016) 416–421.

[57] Y. Mao, J. W. Coenen, J. Riesch, S. Sistla, J. Almanstötter, B. Jasper, A. Terra, T. Höschen, H. Gietl, M. Bram, et al., Development and characterization of powder metallurgically produced discontinuous tungsten fiber reinforced tungsten composites, Physica Scripta 2017 (T170) (2017) 014005.

[58] Y. Mao, J. W. Coenen, J. Riesch, S. Sistla, J. Almanstötter, B. Jasper, A. Terra, T. Höschen, H. Gietl, Ch. Linsmeier, C. Broeckmann, Influence of the interface strength on the mechanical properties of discontinuous tungsten fiber-reinforced tungsten composites produced by field assisted sintering technology, Composites Part A: Applied Science and Manufacturing 107 (2018) 342–353.

[59] Y. Mao, Development and Characterization of Powder Metallurgically Produced Multi- Tungsten Fiber Reinforced Tungsten Composites, PhD thesis, Rheinisch-Westfälische Technische Hochschule Aachen (2019).

[60] J. Coenen, Y. Mao, S. Sistla, A. Müller, G. Pintsuk, M. Wirtz, J. Riesch, T. Hoeschen, A. Terra, J.-H. You, H. Greuner, A. Kreter, C. Broeckmann, R. Neu, Ch. Linsmeier, Materials development for new high heat-flux component mock-ups for DEMO, Fusion Engineering and Design 146 (2019) 1431–1436.

[61] J. W. Coenen, Y. Mao, S. Sistla, J. Riesch, T. Hoeschen, C. Broeckmann, R. Neu, Ch. Linsmeier, Improved pseudo-ductile behavior of powder metallurgical tungsten short fiber-reinforced tungsten (W_f/W), Nuclear Materials and Energy 15 (2018) 214–219.

[62] K. Choy, Chemical vapour deposition of coatings, Progress in materials science 48 (2) (2003) 57–170.

[63] X.-T. Yan, Y. Xu, Chemical Vapour Deposition, 1st Edition, Springer-Verlag London, 2010.

[64] H. Pierson, Handbook of Chemical Vapor Deposition, Vol. 2., Noyes Publications / William Andrew Publishing, LLC, 1999.

[65] A. de Lodyguine, Illuminant for incandescent lamps, US Patent 575: (Jan. 1897).

[66] H. C. Aspinall, et al., Chemical Vapour Deposition, The Royal Society of Chemistry, 2009.

[67] N. E. Miller, I. Beinglass, CVD tungsten interconnect and contact barrier technology for VLSI, Solid State Technology 25 (12) (1982) 85–90.

[68] E. Granneman, Thin films in the integrated circuit industry: requirements and deposition methods, Thin Solid Films 228 (1-2) (1993) 1–11.

[69] K. Kuijlaars, C. Kleijn, H. van Den Akker, A detailed model for low-pressure CVD of tungsten, Thin Solid Films 270 (1-2) (1995) 456–461.

[70] K. Kuijlaars, C. Kleijn, H. Van den Akker, Simulation of selective tungsten chemical vapour deposition, Materials Science in Semiconductor Processing 1 (1) (1998) 43–54.

[71] C. Kleijn, R. Dorsman, K. Kuijlaars, M. Okkerse, H. Van Santen, Multi-scale modeling of chemical vapor deposition processes for thin film technology, Journal of Crystal Growth 303 (1) (2007) 362–380.

[72] M. D. Allendorf, On-line deposition of oxides on flat glass, Interface-Electrochemical Society 10 (2) (2001) 34–39.

[73] K.-L. Choy, Chemical Vapour Deposition (CVD), 1st Edition, Taylor & Francis Inc, University College London, UK, 2019.

[74] T. Kodas, M. Hampden-Smith, The Chemistry of Metal CVD, VCH Weinheim, 1994.

[75] A. F. Zinn, The Chemistry of Metal CVD, VCH Verlagsgesellschaft, Weinheim, 2007, Chapt. Chemical vapor deposition of tungsten, pp. 105–174.

[76] T. Oosterlaken, G. Leusink, G. Janssen, S. Radelaar, The hydrogen reduction of WF_6: A kinetic study based on in situ partial pressure measurements, Journal of the Electrochemical Society 143 (5) (1996) 1668–1675.

[77] E. K. Broadbent, Selective Low Pressure Chemical Vapor Deposition of Tungsten, Journal of The Electrochemical Society 131 (6) (1984) 1427.

[78] Y. Pauleau, Kinetics and Mechanism of Selective Tungsten Deposition by LPCVD, Journal of the Electrochemical Society 132 (11) (1985) 2779.

[79] C. M. McConica, K. Krishnamani, The Kinetics of LPCVD Tungsten Deposition in a Single Wafer Reactor, J. Electrochem. Soc. 133 (1986) 2542–2548.

[80] H. Körner, Selective low pressure chemical vapour deposition of tungsten: Deposition kinetics, selectivity and film properties, Thin Solid Films 175 (1989) 55–60.

[81] W. Bryant, Kinetics of Tungsten Deposition by the Reaction of WF_6 and Hydrogen, Journal of The Electrochemical Society 125 (9) (1978) 1534.

[82] C. R. Kleijn, C. Werner, Modeling of chemical vapor deposition of tungsten films, Birkhäuser, Basel, 1993.

[83] W. Bryant, G. Meier, Kinetics of the Chemical Vapor Deposition of Tungsten, J. Electrochem. Soc. 120.

[84] E. J. McInerney, E. Srinivasan, D. C. Smith, G. Ramanath, Kinetic rate expression for tungsten chemical vapor deposition in different WF_6 flow regimes from step coverage measurements, Zeitschrift für Metallkunde 91 (2000) 573–580.

[85] P. Van der Putte, The reaction kinetics of the H_2 reduction of WF_6 in the chemical vapor deposition of tungsten films, Philips Journal of Research 42 (5/6) (1987) 608–626.

[86] Y. Lian, X. Liu, Z. Xu, J. Song, Y. Yu, Preparation and properties of CVD-W coated W/Cu FGM mock-ups, Fusion Engineering and Design 88 (9/10) (2013) 1694–1698.

[87] F. Hamelmann, G. Haindl, A. Aschentrup, A. Klipp, U. Kleineberg, P. Jutzi, U. Heinzmann, Plasma enhanced MOCVD of smooth nanometer-sized Metal/Silicon Single- and multilayer films, in: T. Allendorf, M.D.; Besman (Ed.), CVD XV: Proceedings of the Fifteenth International Symposium on Chemical Vapor Deposition, Vol. 2000, The Electrochemical Society, 2000, p. 131.

[88] T. G. M. Oosterlaken, G. J. Leusink, G. C. A. M. Janssen, S. Radelaar, K. J. Kuijlaars, C. R. Kleijn, H. E. A. van den Akker, Influence of temperature gradients on partial pressures in a low-pressure chemical-vapor-deposition reactor, Journal of Applied Physics 76 (5) (1994) 3130–3139.

[89] R. Arora, R. Pollard, A Mathematical Model for Chemical Vapor Deposition Processes Influenced by Surface Reaction Kinetics: Application to Low-Pressure Deposition of Tungsten, Journal of The Electrochemical Society 138 (5) (1991) 1523–1537.

[90] J. A. M. Ammerlaan, Kinetics and Characterization of Tungsten CVD Processes, Delft Univ Pr, 1994.

[91] J. Creighton, The surface chemistry and kinetics of tungsten chemical vapor deposition and selectivity loss, Thin Solid Films 241 (1-2) (1994) 310–317.

[92] Institut für Arbeitsschutz der Deutschen Gesetzlichen Unfallversicherung, GESTIS-Stoffdatenbank WF_6 (2019).

[93] COMSOL INC. URL: https://www.comsol.com/.

[94] I. Barin (Ed.), Thermochemical Data of Pure Substances, VCH Verlagsgesellschaft, Weinheim, 1995.

[95] J. O. Hirschfelder, C. F. Curtiss, R. B. Bird, The Molecular Theory of Gases and Liquids, John Wiley & Sons Inc, New York, 1964.

[96] P. A. Tipler, Physik, Spektrum Akademischer Verlag GmbH, Heidelberg, 2000.

[97] D. F. Fairbanks, C. R. Wilke, Diffusion Coefficients in Multicomponent Gas Mixtures, Industrial & Engineering Chemistry 42 (3) (1950) 471–475.

[98] C. R. Wilke, C. Y. Lee, Estimation of Diffusion Coefficients for Gases and Vapors, Industrial & Engineering Chemistry 47 (6) (1955) 1253–1257.

[99] K. Kuijlaars, C. Kleijn, H. Van Den Akker, Multi-component diffusion phenomena in multiple-wafer chemical vapour deposition reactors, The Chemical Engineering Journal and The Biochemical Engineering Journal 57 (2) (1995) 127–136.

[100] C. R. Kleijn, A. Hasper, J. Holleman, C. J. Hoogendoorn, J. Middelhoek, An Experimental and Modeling Study of the Tungsten LPCVD Growth Kinetics from H_2-WF_6 at Low WF_6 Partial Pressures, in: S. S. Wong, S. Furukawa (Eds.), Tungsten and Other Advanced Metals for VLSI/ULSI Applications V, MRS Pub., 1990, pp. 109–116.

[101] A. Hasper, Modeling and Optimization of the Step Coverage of Tungsten LPCVD in Trenches and Contact Holes, Journal of The Electrochemical Society 138 (6) (1991) 1728.

[102] M. Li, S. Dew, M. Brett, T. Smy, Kinetic simulation of metal chemical-vapor deposition on high aspect ratio features in modern very-large-scale-integrated processing, Journal of Vacuum Science & Technology B: Microelectronics and Nanometer Structures Processing, Measurement, and Phenomena 18 (3) (2000) 1343–1347.

[103] Python library SciPy. URL: https://docs.scipy.org/doc/scipy/reference/generated/scipy.optimize.curve_fit.html.

[104] ITA - Insitute für Textiltechnik und Lehrstuhl für Textilmaschinenbau, RWTH Aachen. URL: https://www.ita.rwth-aachen.de/cms/ jezh/ITA/.

[105] H. Gietl, A. v Müller, J. Coenen, M. Decius, D. Ewert, T. Höschen, P. Huber, M. Milwich, J. Riesch, R. Neu, Textile preforms for tungsten fibre-reinforced composites, Journal of Composite Materials 52 (28) (2018) 3875–3884.

[106] Research Centre Jülich, Institute of Energy and Climate Research, Plasma Physics (IEK-4). URL: https://www.fz-juelich.de/iek/iek-4.

[107] Python library Skimage. URL: https://scikit-image.org/docs/dev/api/skimage.html.

[108] Raumann, GitHub repository for the model and script files of the present work, URL: https://github.com/Leo-Raumann/Dissertation-Files.git (2020).

[109] M. Knudsen, The Kinetic Theory of Gases, John Wiley & Sons, Inc., New York, 1950.

[110] G. Gottstein, Materialwissenschaft und Werkstofftechnik, Springer-Verlag GmbH, Heidelberg, 2013.

[111] E. O. Hall, The Deformation and Ageing of Mild Steel: III Discussion of Results, Proceedings of the Physical Society. Section B 64 (9) (1951) 747–753.

[112] N. Hansen, Hall–Petch relation and boundary strengthening, Scripta Materialia 51 (8) (2004) 801–806.

[113] Q. Wei, T. Jiao, K. T. Ramesh, E. Ma, L. J. Kecskes, L. Magness, R. Dowding, V. U. Kazykhanov, R. Z. Valiev, Mechanical behavior and dynamic failure of high-strength ultrafine grained tungsten under uniaxial compression, Acta Materialia 54 (2005) 7.

[114] Q. Wei, K. Ramesh, L. J. Kecskes, S. N. Mathaudhu, K. Hartwig, Ultrafine and Nanostructured Refractory Metals Processed by SPD: Microstructure and Mechanical Properties, Materials Science Forum 579 (2008) 75–90.

[115] D. J. Dunstan, A. J. Bushby, Grain size dependence of the strength of metals: The Hall–Petch effect does not scale as the inverse square root of grain size, International Journal of Plasticity 53 (2014) 56–65.

[116] G. Subhash, Y. Lee, G. Ravichandran, Plastic deformation of CVD textured tungsten—I. Constitutive response, Acta Metallurgica et Materialia 42 (1) (1994) 319–330.

[117] Z. Levin, K. Hartwig, Strong ductile bulk tungsten, Materials Science and Engineering: A 707 (2017) 602–611.

[118] A. J. Learn, D. W. Foster, Resistivity, grain size, and impurity effects in chemically vapor-deposited tungsten films, Journal of Applied Physics 58 (5) (1985) 2001–2007.

[119] M. Haque, U. Patel, H. Naseem, W. Brown, Atmospheric pressure chemical vapor deposition of blanket tungsten films on silicon substrates for integrated circuit applications, Journal of electronic materials 24 (6) (1995) 761–766.

[120] Y. Lian, X. Liu, J. Wang, F. Feng, Y. Lv, J. Song, J. Chen, Influence of surface morphology and microstructure on performance of CVD tungsten coating under fusion transient thermal loads, Applied Surface Science 390 (2016) 167–174.

[121] J. Q. Shi, S. Y. Yao, F. Wang, X. D. Yu, H. T. Huang, C. W. Tan, Z. H. Nie, H. L. Ma, H. N. Cai, Microstructures of chemical vapor deposited high-purity tungsten achieved by two different precursors, Materials Characterization 134 (2017) 1–8.

[122] C. Guo, J.-C. Wang, Z.-J. Wang, J.-J. Li, Y.-L. Guo, S. Tang, Investigation of atom-attaching process of three-dimensional body-center-cubic dendritic growth by phase-field crystal model, Acta Physica Sinica 64 (2) (2015) 028102.

[123] D. Y. Sun, M. Asta, J. J. Hoyt, Crystal-melt interfacial free energies and mobilities in fcc and bcc Fe, Physical Review B 69 (17).

[124] C. M. Melliar-Smith, A. C. Adams, R. H. Kaiser, R. A. Kushner, Chemically vapor deposited tungsten for semiconductor metallizations, Journal of The Electrochemical Society 121 (2) (1974) 298–303.

[125] I.-S. Chang, M.-H. Hon, Growth characteristics and electrical resistivity of chemical vapor-deposited tungsten film, Thin Solid Films 333 (1-2) (1998) 108–113.

[126] Adobe Photoshop, image processing software. URL: http://www.adobephotoshop.com.

[127] Digitizer software: Digitize it. URL: https://www.digitizeit.de/.

[128] Y. Kajikawa, T. Tsumura, S. Noda, H. Komiyama, Y. Shimogaki, Nucleation of W during Chemical Vapor Deposition from WF_6 and SiH_4, Japanese Journal of Applied Physics 43 (6B) (2004) 3945–3950.

[129] R. E. Bolz, CRC handbook of tables for applied engineering science, CRC press, 2019.

[130] F. Klein, T. Wegener, A. Litnovsky, M. Rasinski, X. Tan, J. Schmitz, Ch. Linsmeier, J. Coenen, H. Du, J. Mayer, U. Breuer, On Oxidation Resistance Mechanisms at 1273 K of Tungsten-Based Alloys Containing Chromium and Yttria, Metals 8 (7) (2018) 488.

[131] M. Treitz, Development of production routines for fibre reinforced metal matrix composites, Master's thesis, University of Applied Sciences Munich (2019).

[132] J. Riesch, A. Feichtmayer, M. Fuhr, J. Almannstötter, J. Coenen, H. Gietl, T. Höschen, A. Manhard, Ch. Linsmeier, R. Neu, Tensile behaviour of drawn tungsten wire used in tungsten fibre-reinforced tungsten composites, Physica Scripta (T170) (2017) 014032.

[133] H. Gietl, J. Riesch, J. Coenen, T. Höschen, R. Neu, Production of tungsten-fibre reinforced tungsten composites by a novel continuous chemical vapour deposition process, Fusion Engineering and Design 146 (2019) 1426–1430.

[134] J. Rumble (Ed.), CRC Handbook of Chemistry and Physics, 99th Edition, CRC Press, Boca Raton, 2018.

[135] Deutsche Edelstahlwerke, Werkstoffdatenblatt X6CrNiMoTi17-12-2, 1.4571 (2015).

[136] F. M. Mourits, F. H. Rummens, A critical evaluation of Lennard–Jones and Stockmayer potential parameters and of some correlation methods, Canadian Journal of Chemistry 55 (16) (1977) 3007–3020.

[137] L. Zarkova, U. Hohm, pVT–Second Virial Coefficients B(T), Viscosity η(T), and Self-Diffusion ρD(T) of the Gases: BF_3, CF_4, SiF_4, CCl_4, $SiCl_4$, SF_6, MoF_6, WF_6, UF_6, $C(CH_3)_4$, and $Si(CH_3)_4$ Determined by Means of an Isotropic Temperature-Dependent Potential, Journal of Physical and Chemical Reference Data 31 (1) (2002) 183–216.

Acknowledgments

By no doubt, the biggest thanks goes to my supervisor Jan W. Coenen. He gave me the PhD position, a great start, weekly support in all aspects, cheers, corrections, point outs, and praise. He understood my problems before the sentence was finished and gave me quickly very good, clear and helpful suggestions. I could not think of a better supervisor.

Special thanks goes to Prof. Oliver Guillon (head of the IEK-1 and professor at the RWTH Aachen, at which I studied *Material Engineering*), for being my doctoral supervisor. Although being very busy, he was always very supportive by regular meetings, visiting my presentations, and correcting my interim reports – which is remarkable.
Also a great thanks to Prof. Christian Linsmeier (head of the IEK-4, where I was employed and located during my PhD and beyond) for being my second examiner, for the yearly exchange, and for the detailed revision and support regarding the manuscript of my first publication. Also a big thanks to Johann Riesch from the IPP Garching for being my second supervisor regarding CVD and modeling, and also for the detailed revisions and structural improvements with respect to my writings.

Many thanks also to my IEK-4 colleges, Yiran Mao, Daniel Schwalenberg, and Alexis Terra for scientific discussions and assistance.
Also a great thanks to our staff members Rudi Caspers, Beatrix Göths, Dirk Nicolai, Tim Rüttgers, Robert Habrichs, and Albert Hiller. Without them I could not have done all the experiments.
Another big thanks goes to Tobias Wegener for scripting assistance, especially regarding the complicated calculation of the thermal diffusion coefficients and to the entire Python community for creating such a great open source programming language.
And to my IPP Garching colleges, Hans Gietl, and Till Höschen for scientific discussions, whereby the second part of this dissertation would not have reached the presented scope without the work of Hans Gietl.

I would also like to thank Prof. Chris Kleijn, an expert on W-CVD modeling, for allowing me to visit him in the Technical University Delft, for listening to my research status, and for the scientific discussion.
Additionally, I have to thank Annette Pahl and Clemens Ruhl from the COMSOL Support

for their patience and assistance in in solving many Comsol error issues.

And last but not least, I owe most deeply gratitude to my family and friends for their encouragements and support, in particular to my wife, Anh Thu, for covering my back countless of time, especially in the PhD final phase, in which our first child, Levia, was born.

Band / Volume 501
Retrieval of atmospheric quantities from remote sensing measurements of nightglow emissions in the MLT region
Q. Chen (2020), 208 pp
ISBN: 978-3-95806-485-0

Band / Volume 502
Auswirkungen der Energiewende auf das deutsche Gastransportsystem
B. Gillessen (2020), XVII, 186
ISBN: 978-3-95806-487-4

Band / Volume 503
Lagrangian Simulation of Stratospheric Water Vapour: Impact of Large-Scale Circulation and Small-Scale Transport Processes
L. Poshyvailo (2020), 124 pp
ISBN: 978-3-95806-488-1

Band / Volume 504
Water Management in Automotive Polymer-Electrolyte-Membrane Fuel Cell Stacks
S. Asanin (2020), XVIII, 172 pp
ISBN: 978-3-95806-491-1

Band / Volume 505
Towards a new real-time irrigation scheduling method: observation, modelling and their integration by data assimilation
D. Li (2020), viii, 94 pp
ISBN: 978-3-95806-492-8

Band / Volume 506
Modellgestützte Analyse kosteneffizienter CO_2-Reduktionsstrategien
P. M. Lopion (2020), XIV, 269 pp
ISBN: 978-3-95806-493-5

Band / Volume 507
Integration of Renewable Energy Sources into the Future European Power System Using a Verified Dispatch Model with High Spatiotemporal Resolution
C. Syranidou (2020), VIII, 242 pp
ISBN: 978-3-95806-494-2

Band / Volume 508
Solar driven water electrolysis based on silicon solar cells and earth-abundant catalysts
K. Welter (2020), iv, 165 pp
ISBN: 978-3-95806-495-9

Schriften des Forschungszentrums Jülich
Reihe Energie & Umwelt / Energy & Environment

Band / Volume 509
Electric Field Assisted Sintering of Gadolinium-doped Ceria
T. P. Mishra (2020), x, 195 pp
ISBN: 978-3-95806-496-6

Band / Volume 510
Effect of electric field on the sintering of ceria
C. Cao (2020), xix, 143 pp
ISBN: 978-3-95806-497-3

Band / Volume 511
Techno-ökonomische Bewertung von Verfahren zur Herstellung von Kraftstoffen aus H_2 und CO_2
S. Schemme (2020), 360 pp
ISBN: 978-3-95806-499-7

Band / Volume 512
Enhanced crosshole GPR full-waveform inversion to improve aquifer characterization
Z. Zhou (2020), VIII, 136 pp
ISBN: 978-3-95806-500-0

Band / Volume 513
Time-Resolved Photoluminescence on Perovskite Absorber Materials for Photovoltaic Applications
F. Staub (2020), viii, 198 pp
ISBN: 978-3-95806-503-1

Band / Volume 514
Crystallisation of Oxidic Gasifier Slags
J. P. Schupsky (2020), III, 127, XXII pp
ISBN: 978-3-95806-506-2

Band / Volume 515
Modeling and validation of chemical vapor deposition for tungsten fiber reinforced tungsten
L. Raumann (2020), X, 98, XXXVIII pp
ISBN: 978-3-95806-507-9

Weitere ***Schriften des Verlags im Forschungszentrum Jülich*** unter
http://wwwzb1.fz-juelich.de/verlagextern1/index.asp

Energie & Umwelt / Energy & Environment
Band / Volume 515
ISBN978-3-95806-507-9

Mitglied der Helmholtz-Gemeinschaft

JÜLICH
Forschungszentrum